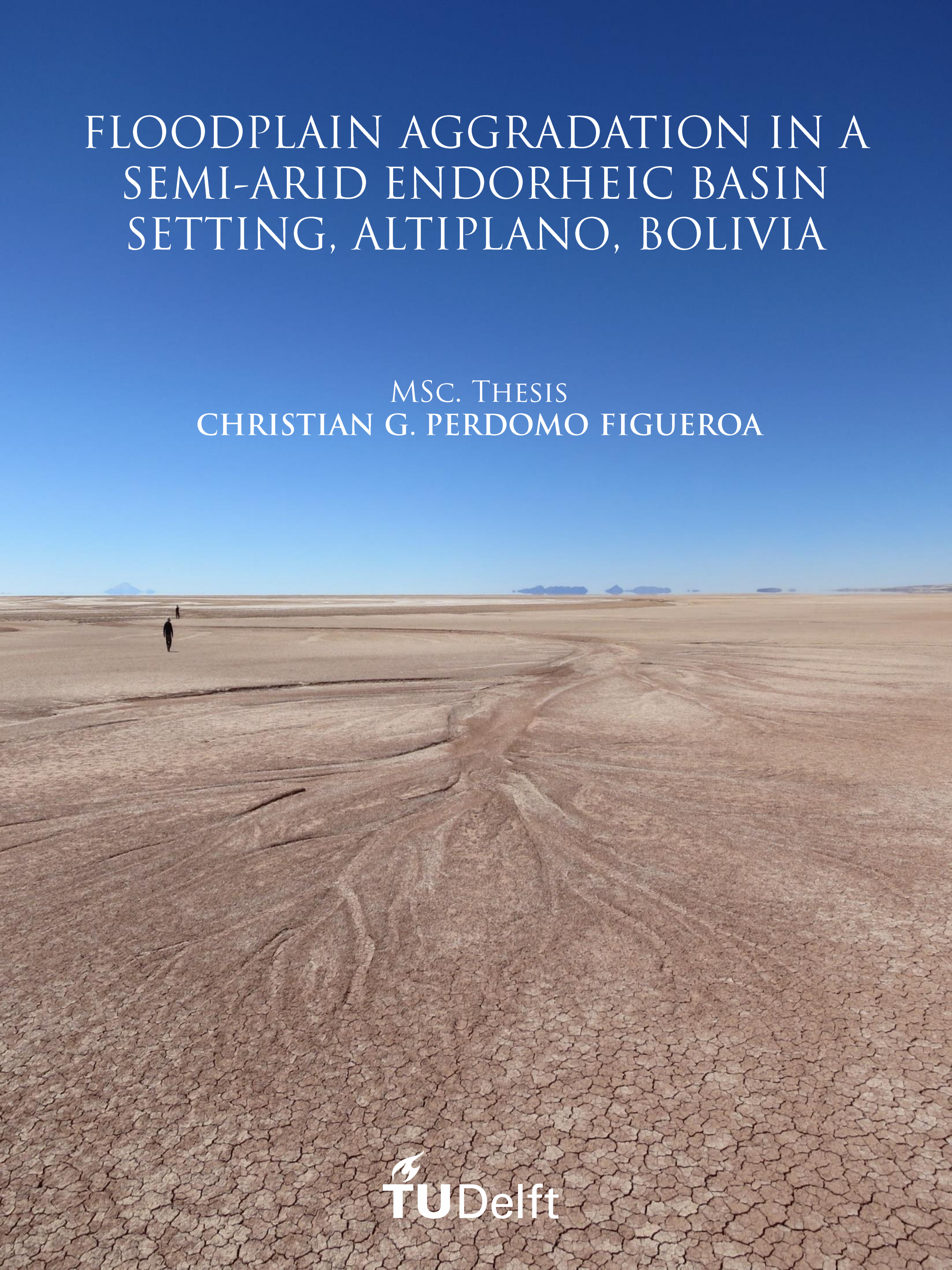

FLOODPLAIN AGGRADATION IN A SEMI-ARID ENDORHEIC BASIN SETTING, ALTIPLANO, BOLIVIA

MSc. Thesis

CHRISTIAN G. PERDOMO FIGUEROA

This thesis is dedicated to my beloved parents and sister

FLOODPLAIN AGGRADATION IN A SEMI-ARID ENDORHEIC BASIN SETTING, ALTIPLANO, BOLIVIA

By

CHRISTIAN GUILLERMO PERDOMO FIGUEROA

TO OBTAIN THE DEGREE OF MASTER OF SCIENCE
AT DELFT UNIVERSITY OF TECHNOLOGY,
FACULTY OF CIVIL ENGINEERING AND GEOSCIENCES,
SECTION OF APPLIED GEOLOGY,
TO BE DEFENDED PUBLICLY ON WEDNESDAY NOVEMBER 15th, 2017 AT 02:00 PM

Student number:	4500180	
Project duration:	November 2016 – November 2017	
Thesis committee:	Dr. M.E. Donselaar (Chair)	TU Delft Supervisor
	K.A. van Toorenenburg, MSc.	TU Delft, daily supervisor
	Dr. J.E.A (Joep) Storms	TU Delft
	Adriana Guatame-García, MSc.	TU Delft
	Dr. M.G.G. de Jong	ENGIE

Abstract

The importance of gas as a driver of security of energy supply and the influence of the role it currently has and will continue having in the energy transition has stimulated the development of further research studies in unconventional sources of natural gas. Mature gas fields of coarse-grained fluvial reservoirs have already reached their production plateau and are in a production decline with high-water cuts.

The northwest gas province of the Netherlands contains low-permeable fine-grained fluvial deposits of which the reservoir architecture and connectivity have not yet been widely studied using the standard industry techniques. For this reason, the geomorphological and sedimentological characteristics of the Río Colorado fluvial system were used as a modern analogue to determine how the river avulsion process has generated the current fluvial topography and why its repetition has developed a vertical stacking pattern of thin but laterally extensive layers.

Differential Global Positioning System data, Google Earth Pro Imagery, and previous studies focused on the evolution analysis of river positions in this region, allowed the observation of multiple repetitions of avulsion river in an area of approximately 400 km^2, describing the fluvial sediments on top of the lacustrine deposits and representing alluvial ridges with an average width of 1500 m. Moreover, a thickness variation between the fluvial and lacustrine deposits up to 2 meters was recognised over 25 km, and a very gentle gradient slope, from 0.02° at the apex of the fluvial fan to 0.0022° in the flattened section towards the Salar de Uyuni.

Borehole data from the West Netherlands Basin and surface data from the Río Colorado were integrated to construct a three-dimensional model that represents the characteristics of the fluvial deposits regarding geobody size, geometry, and potential connectivity. With this, and the distribution of porosity and permeability as a function of channel belt and alluvial ridge width resulted in reservoir volumes up to $2 \times 10^9 \mathrm{sm}^3$.

Six wells were simulated to understand the production behaviour in channel belts, alluvial ridges, and floodplain sediments. Water saturation, pressure and streamline maps differ from well to well, and the model contributed to quantify the most efficient production rates per well location in the fluvial fan system. The results allowed to predict the communication between facies and how that connectivity reflected the resultant flow rates and recovery factors, showing the tough gas as potential secondary targets and prolonging the production stages of mature oil fields.

Acknowledgements

ENGIE E&P NL B.V., Energiebeheer Nederland B.V. (EBN), and Delft University Foundation Fund (UfD) have financially supported this work, to whom I am sincerely grateful. The thesis is part of the Tough Gas research project at the Delft University of Technology.

The warmest gratitude goes to Professor Rick Donselaar and K.A van Toorenenburg, for their supervision and constant wise guidance throughout the entire development of this thesis. Since the beginning of the project in Bolivia, they have had a friendly attitude; always opened for explanations, suggestions, and proper feedback.

Many thanks to my parents Martha Figueroa and Guillermo Perdomo and my sister Thatiana Perdomo; I am grateful for our love and constant motivation to explore the beautiful meaning of life. Special thanks to Manuela Posada Henao, for her invaluable support in tough and joyful moments, continuously sharing her positivism.

I would like to express my gratitude towards Roberto Trujillo Cuellar. We have had many great times during the studies and will hopefully have many more.

Abbreviations

2D	Two-dimensional space
3D	Three-dimensional space
A_i	Area percentage per facies
ASCII	American Standard Code for Information Interchange
Bg	Gas Formation Volume Factor
BP	Before Present
BRV	Bulk Rock Volume
C	Carbon
cal	Calendar
$CaSO_4$	Calcium Sulphate
CSRS	Canadian Spatial Reference System
dGPS	Differential Global Positioning System
Eg	Gas Expansion Factor
$E[x]$	Expected Value
FDP	Field Development Project
GIIP	Gas Initially In Place
GNSS	Global Navigation Satellite Systems
GR	Gamma-ray
$HCPV$	Hydrocarbon Pore Volume
m	Meters
mD	Millidarcy
mm	Millimetres
k	Permeability
ka	Kiloannus
km	Kilometres
kW	Kilowatts

LST	Lowstand System Tract
NaCl	Sodium Chloride
NTG	Net to Gross
OSL	Optically Stimulated Luminescence
PPP	Precise Point Positioning
PRW-01	Pernis West – 01
q_i	Production rate
RINEX	Receiver Independent Exchange Format
S_g	Gas Saturation
sm^3	Standard Cubic Meters
S_{wirr}	Irreducible Water Saturation
S_w	Water Saturation
Th	Thorium
U	Uranium
yr	Year
°C	Celsius Degrees
φ	Porosity
γ	Gamma

Contents

List of Figures

List of Tables

1. Introduction

Floodplain deposition is an important process for the development of river channels regarding sediment accumulation. Most of these sediments among and beyond channel belts are deposited when a discharge of fluid flow occurs. The confined water reaches the maximum capacity of the channel, exceeding the levees of the river and spreading out very-fine sand and silt onto the floodplain, fining away from the channel (Nichols, 2009). Amalgamated floodplain deposits elevate the floodplain around the active channel before an upstream avulsion occurs (Van Toorenenburg, et al., 2016). These shifting in river flows out of a fixed pathway into a new region in the floodplain is called river avulsion (Mohrig, et al., 2000). The topography of the floodplain deposits plays an important role in the location of avulsed channels. It repels new channels due to the alluvial ridges along the floodplains created by previous channels (Mackey & Bridge, 1995) or influences between incisional and aggradational avulsion modes depending on the characteristics of the floodplain drainage (Mohrig, et al., 2000).

In the past, these thin sand sheets were bypassed as potential gas reservoirs, due to their poor detectability with conventional wireline logs, low recognition with 2D and 3D seismic data, and relatively lower petrophysical properties compared to coarse-grained fluvial sandstones. However, the interest of the oil and gas companies in this type of thin-bedded reservoir bodies is increasing due to the increment in water cut and pressure depletion in mature oilfields, and the high costs required for the drilling of new wells in reservoirs with high-quality reservoir properties. The already existing wells and facilities are an advantage for the production and economic evaluation of secondary targets like the one involved in this study, as part of the Tough Gas project at the Delft University of Technology.

The semi-arid Río Colorado, located in the southeast part of the Altiplano Basin, Bolivia, provides a modern-day analogue to characterise the evolution of ancient river systems regarding gradient profile, stacked channel fills, floodplain aggradation and lateral extension of sand layers. Several authors have studied the processes of avulsion in these low-gradient fluvial setting for different purposes. First, to determine the avulsion frequency during the last 4000 years using absolute age dating and to understand how the river flow-paths evolve in time and space (Donselaar, et al., 2017). Secondly, to analyse the influence of floodplain aggradation controlling switching of rivers (Van Toorenenburg, et al., 2016b).

The aim of this study is to integrate the evolution of the current fluvial topography of the Río Colorado (regarding geomorphological and sedimentary characteristics of this fluvial fan system) with the subsurface data from the West Netherlands Basin (wireline log from the Pernis West-01 and core plugs) in a three-dimensional model.

A fieldwork collecting-data campaign was planned to obtain information of the fluvial fan at the southeast of the Salar de Uyuni, Bolivia. Differential GPS data provides the topography data, the sedimentary logs allows to quantify a net to gross and to describe sedimentary structures, and previous studies using Optical Stimulated Luminescence age dating (OSL) provides the river avulsion frequency (Donselaar, et al., 2017). The borehole data provides gamma-ray for lithology identification (normally, sandstones and claystones have different reading signatures), and the porosity and permeability from plug samples are used to distribute the rock properties as a funtion of channel belt and alluvial ridge width. The resultant dynamic model is expected to simulate the conditions for a dry gas reservoir and to improve the prediction of fluid flow paths, estimating the uncertainty in volume calculations and enhance the reservoir management providing effective production rates.

2. Geological Setting

The Altiplano Basin, formed in the central Andean Chain in South America, is one of the largest continental plateaus on Earth. The basin is limited by the Eastern and Western Cordilleras, in an extension of around 200 km, with a low topographic relief and an average elevation of 3800 m above sea level (Murray, et al., 2010). Both cordilleras supplied the succession of Upper Cretaceous and Cenozoic sedimentary and volcanic rocks, summarized as: sequence of carbonate rock in the lower succession (El Molino Formation) from the Maastrichtian and mid-Palaeocene, fluvial siltstone and sandstone (Santa Lucia Formation), Eocene to Oligocene fluvial sandstone (Potoco Formation), fluvial fan conglomerates (Coniri Formation) and several upper Oligocene to Quaternary volcanoclastic series (DeCelles & Horton, 2003).

2.1 Tectonic Evolution

Throughout the formation of the Andean Orogenic System, several structural elongated depressions were developed, including the Altiplano Basin (Figure 1); a large endorheic basin that extends from Peru to the north of Argentina. These basins constitute physiographic depressions inside the mountain relief and have been widespread areas of synorogenic erosion and transport of clastic sediments, producing a substantial record of Cenozoic nonmarine sedimentation, including young deposits filling the modern foreland region and ancient deposits exposed within the central Andes (Horton, et al., 2001).

The Altiplano Basin was formed in the Late Cretaceous-Paleogene (Hammerschmidt, et al., 1992) as a result of the oblique subduction of the oceanic Nazca Plate beneath the western margin of the South American Plate (Isacks, 1988). The basin is flanked to the west by Neogene arc-related volcanic rocks of the Western Cordillera and the east by deformed Palaeozoic rocks of the Eastern Cordillera (Hampton & Horton, 2007).

This endorheic basin is located in the widest part of the Andean Chain. It covers 200,000 km^2, extending from 14° to 22°S latitude and 66° to 71°W longitude (Rigsby, et al., 2005) and an altitude varying from 3700 to 4100 m, with small relieves that can reach 4600 m (Lavenu, 1991).

Regional seismic data, GPS surveys and the flat-lying nature of the Quaternary strata all suggest that tectonic activity did not have a major influence on the Holocene and late Pleistocene lake terrace sediments (Bills, et al., 1994). Therefore, the sediment supply - by the fluvial activity over the lacustrine deposits - in combination with the climate variation has played a vital role in the development of the basin in the last thousands of years.

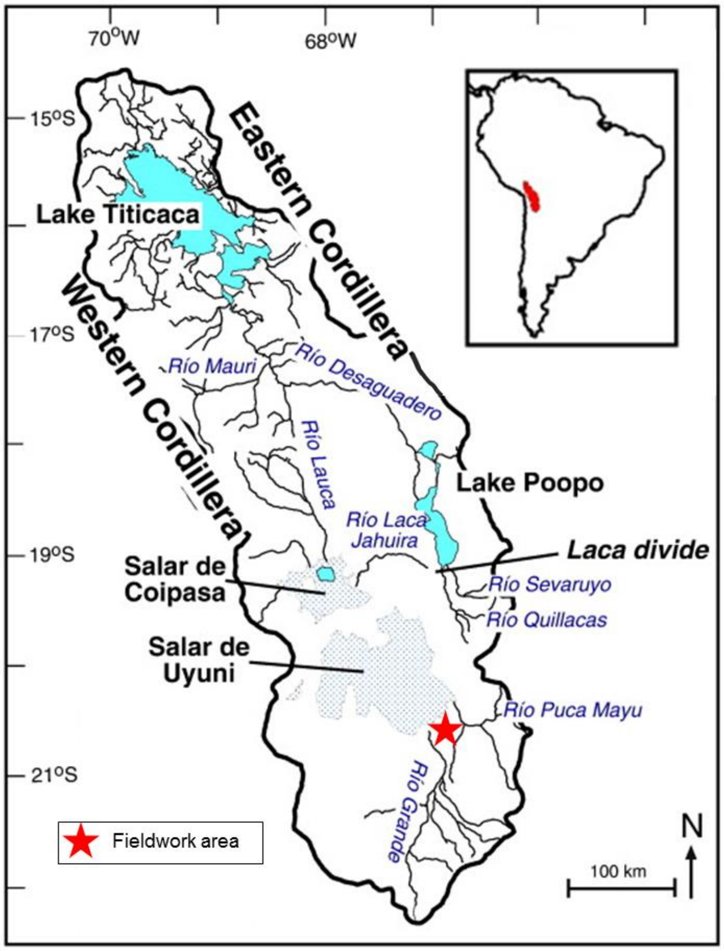

Figure 1. Major hydrographic features in the Altiplano Basin. Modified from (Placzek, et al., 2011).

2.2 Climatic Setting

The climatic conditions of the basin are one of the variables that influence the evolution of the basin. Since the Pleistocene, this region has been affected by wetter and drier periods, causing expansion and contraction of the lakes present in the area. Nowadays, the basin experiences dry climate conditions, resulting in the progradation of fluvial systems like the Río Colorado (Donselaar, et al., 2013), which is the main hydrological feature of study in this work.

The Altiplano Basin is occupied by four main hydrographic basins: Lake Titicaca at the north, Lake Poopo in the centre, and Salar de Coipasa and Salar de Uyuni at the south (Figure 1 and Figure 2). These hydrographic basins have changed since the late Pleistocene as a combination of two modes of variation in the rainfall precipitations over the central Andes (Placzek, et al., 2011). 1) Rainfalls in the northern part of the Altiplano that were developed during the austral summer period (from December until March); when the Intertropical Convergence Zone (Figure 3) is displaced towards the south and convection is stronger in the Amazon Basin (Lenters & Cook, 1997). 2) Summer rainfalls on the south part of the Altiplano with an interannual variability mostly related to precipitation anomalies and humidity levels in the Chaco region of Argentina (Vuille & Keimig, 2004).

These variations from wetter to drier conditions are different between the north and south of the Altiplano.The Lake Titicaca to the north with a permanent deep freshwater (>285 m water depth), a very shallow Lake Poopo with which periodically dries out, and Salar de Coipasa and Salar de Uyuni as seasonal hypersaline lakes (Argollo & Mourguiart, 2000).

Besides, sedimentological and palynological studies of paleoshorelines, cores with muds containing abundant diatoms, and U-Th and ^{14}C showed that the Altiplano experienced wetter and drier climate periods, due to changes in atmospheric circulation and evapotranspiration (Placzek & Patchett, 2006). Dry events are marked by salt deposits that consist mainly of halite (NaCl) and gypsum (CaSO4) and, using the natural γ-radiation (much higher values for lacustrine muds than the salt deposits), it is possible to measure the changes in moisture through time (Baker, et al., 2001). In wetter periods, the Salar was occupied by a series of three lacustrine phases (Argollo & Mourguiart, 2000): The oldest paleolake is the Minchin, with an age of about 42,000 calendar year BP and yielding an interpolated age for the top of the interval of 38,100 cal.yr BP. For the Tauca period (26, 100 – 14,900 cal.yr BP) the dates were attributed from lacustrine muds (Figure 3C). Low values of γ-radiation of the paleolake Coipasa indicate an age of about 14,900 to 12,500 cal.yr BP (Baker, et al., 2001).

Above the current level of the present-day Salar de Uyuni, several highstand lake levels are determined: +140 m for the Minchin, +127 m for the Tauca paleolake and ≤+55 m for the Coipasa period (Bills, et al., 1994) and (Placzek & Patchett, 2006). Each wet period has its subsequent dry cycle when the lakes contracted and converted to hypersaline lakes. At present, the basin is in a dry climate period with low lake levels and formation of Lowstand Systems Tract (LST) deposits (Donselaar, et al., 2013).

Current precipitations in the area of study allow understanding the processes of runoff that determine the present-day morphology. Because of that, it is shown the measurements of weather stations in the Uyuni hydrographic basin from 1990 to 2007, describing a periodic variation of annual and monthly precipitation (Figure 4), with an average of 196 mm/yr and concentrated from December to March (Donselaar, et al., 2013).

2.3 Río Colorado fluvial system

Previous authors (Donselaar, et al., 2017) have reconstructed the abandoned channel pathways in the area of study using the Optically Stimulated Luminescence (OSL). This technique allows obtaining a better understanding of the overlapping of channels and their avulsions. These sedimentation processes have formed a fluvial fan morphology (Figure 5), constituted by a network of stacked river channels in combination with the associated point bars, crevasse channels and splays, and floodplain deposits. The abandoned channels and present-day river have a flow direction from southeast to northwest, terminating on a coastal plain with an extremely low dip (0.0022°) towards the border of the Salar de Uyuni. The lithology of the coastal plain consists of mud, silt and very fine sand with salt cement (Donselaar, et al., 2013). The nature of the sedimentary processes in the area of study analysed, combined with the climate fluctuations, is responsible for the current morphology of the Río Colorado system.

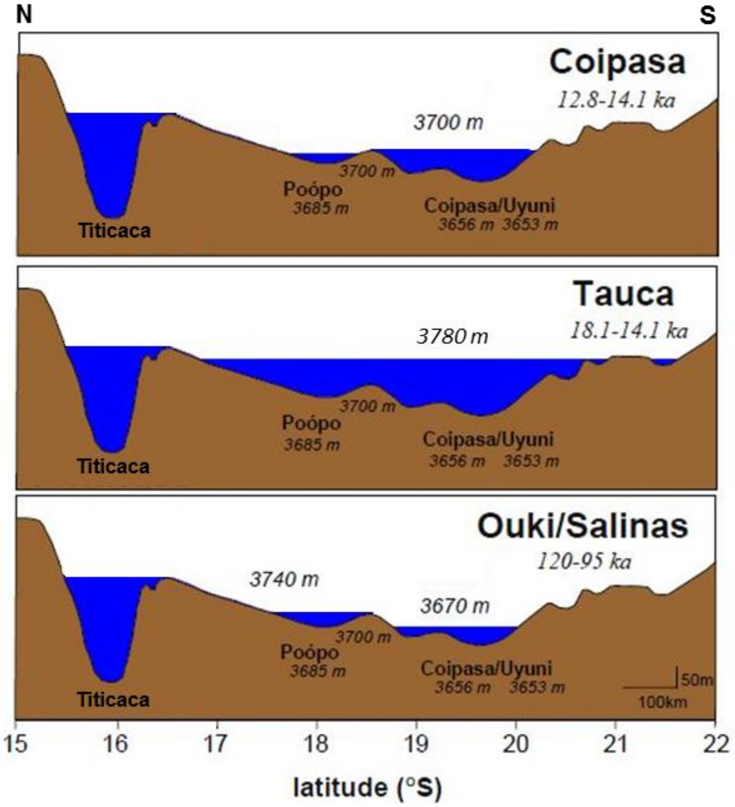

Figure 2. Schematic cross-sections of the main hydrographic basins for the three paleo-lake cycles. Modified from (Placzek, et al., 2011).

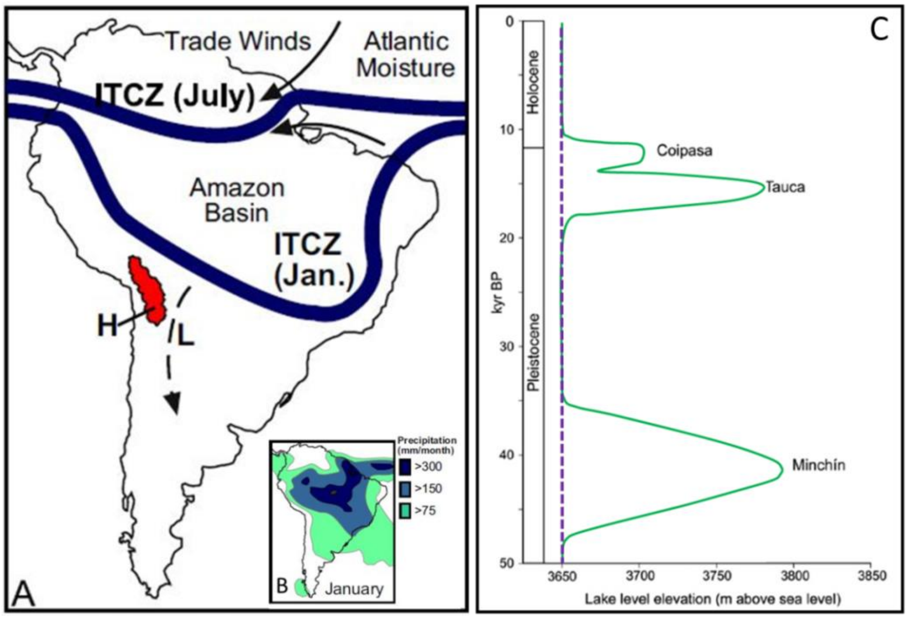

Figure 3. (A) Main climate features in South America: the Altiplano Basin (Red), the (Intertropical Convergence Zone) and the trade winds (Placzek, et al., 2013). (B) Monthly precipitations for January (Placzek, et al., 2013) and (C) Highstand lake levels variations since the Pleistocene–Holocene. Present-day Salar de Uyuni level in purple. Modified from (Donselaar, et al., 2013).

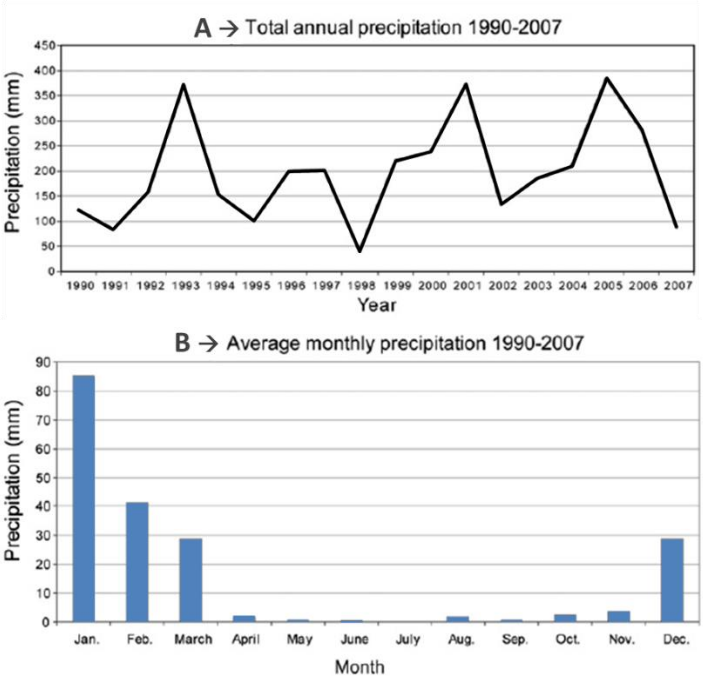

Figure 4. Precipitation data from Uyuni hydrographic basin. (A) Total annual precipitation from 1990 to 2007. (B) Average monthly precipitation from 1990 to 2007. Modified from (Donselaar, et al., 2013)

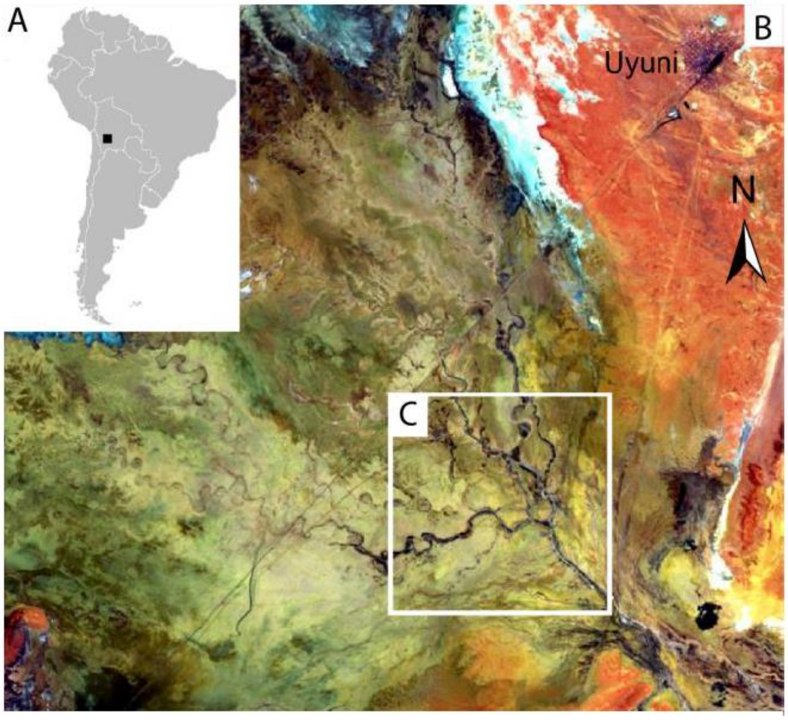

Figure 5. A) Map of South America with location. B) Landsat image of the regional area of study. Scale view: 25x25 km. C) Detailed area with avulsion network. (Donselaar, et al., 2017)

2.4 Rot Fringe and Solling formations

This study integrates the geomorphology and sedimentology characteristics of the Río Colorado in the Altiplano Basin and the subsurface data of the West Netherlands Basin with the Solling and Rot Fringe formations. These formations are part of the Upper Germanic Trias Group and were deposited during the Late Scythian and Early Anisian respectively (Van Adrichem Boogaert & Kouwe, 1993); around 240 Ma ago. The Rot Fringe Formation is composed of claystones, sandstones and some thin anhydrite layers occurred under fluvial conditions (Van Adrichem Boogaert & Kouwe, 1993). The Solling Formation is underlying the Rot Fringe Formation, and consists of claystones intercalated with sandstones. This claystones were deposited in a lacustrine setting (Van Adrichem Boogaert & Kouwe, 1993). Appendix A describes the overall stratigraphic framework of West Netherlands Basin.

3. Methods and Data Acquisition

3.1 Fieldwork Data Acquisition

Prior to the data acquisition campaign, Google Earth Pro Imagery was used to determine the morphological characteristics of the area, to load useful station points used in previous fieldworks by (Torres Carranza, 2013) and K.A. van Toorenenburg in 2014, to select the location of the lithology logs and to design the transect routes for the dGPS measurements to be collected (fully described in the next section of this chapter).

The fieldwork was carried out from the 27th of October until the 9th of November of 2016, to collect data for the geomorphological and sedimentological analysis of the Río Colorado, and then build the 3D static and dynamic model.

3.1.1 Differential GPS data

Figure 6 describes the essential elements that compound the setup of the dGPS; a fixed base station and a remote station at the top of the Rover that can be separated approximately 2 km far from the base station to record reliable information.

Several transects were drawn perpendicular to the orientation of the present-day river and river avulsion paths (red line and branching grey brownish lines respectively, Figure 7C). These transects are concentrated in an area limited at the southeast by a national road and at the northwest by the railway (dashed lines, Figure 7C and Figure 7D). Once the main region was covered (where the river starts avulsing randomly), the data acquisition was extended with three more sections of the fluvial fan system, from proximal to distal, to analyse the gradient and slope changes in the area (Figure 7B).

Appendix B describes the schedule during the first stage of the fieldwork. It shows the timing on/off of the base station and rover during the recording of GPS signals for the detailed transects (from A-A’ to P-P’) and the regional sections (proximal, medial and distal) of the fluvial fan system.

3.1.1.1 dGPS data processing

Before starting with the analysis of the dGPS data obtained in the fieldwork, the recording signal and timing on/off of the base and remote stations were processed using the Precise Point Positioning (PPP) from The Canadian Spatial Reference System (CSRS). The access to this service is free, and data were submitted to perform the computation of the Global Navigation Satellite Systems (GNSS) information acquired in the fieldwork to obtain higher accuracy positions from the raw observation data.

A brief description of the procedure implemented by this system is summarised. First, data is transferred to a computing device as an ASCII or binary format. Secondly, the raw data extracted from the dGPS devices are transformed into the Receiver Independent Exchange Format (RINEX). It is recommended to compress the file to minimise the upload time. The PPP uses the GNSS satellite orbit ephemerides to produce corrected coordinates of a constant "absolute" accuracy, regardless of proximity to known base stations.

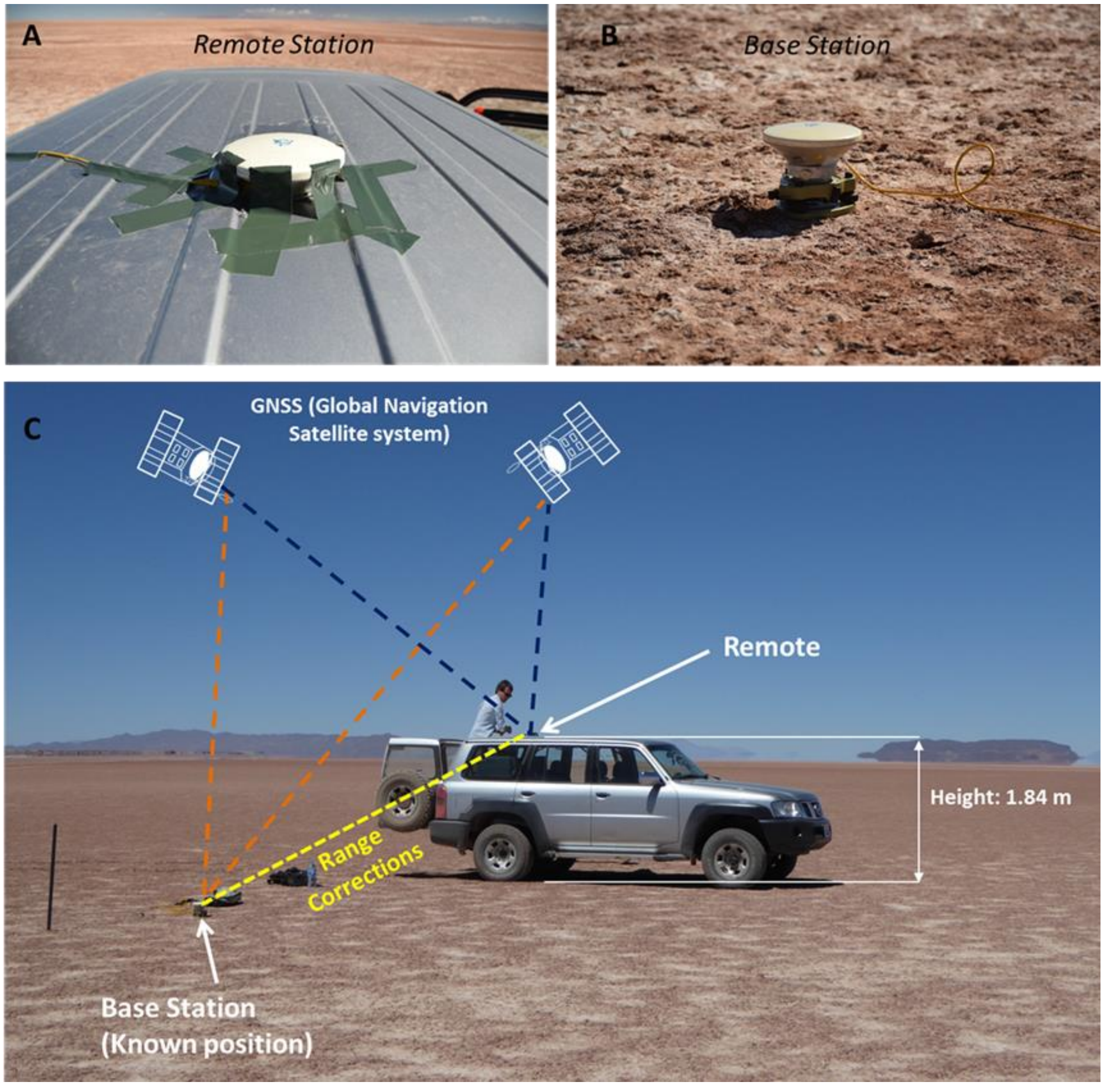

Figure 6(A). Remote station at the top of the car, 1.84 meters above the flat surface. (B) Ground-based reference station. (C) Non-real time *dGPS set up.*

3.1.1.2 dGPS profiles

QGIS software was used to analyse the dGPS data. The plugin *Profile to points* allowed the creation of several profiles from the dGPS data recorded in the field. These patterns provided valuable information about the evolution of the avulsion of the Río Colorado and, combined with the absolute dating with the OSL method; it was possible to understand the process of avulsion controlling the spatial and temporal distribution of pre-existing river channels. Chapter 4 of this report contains nine of the main profiles used for the analysis.

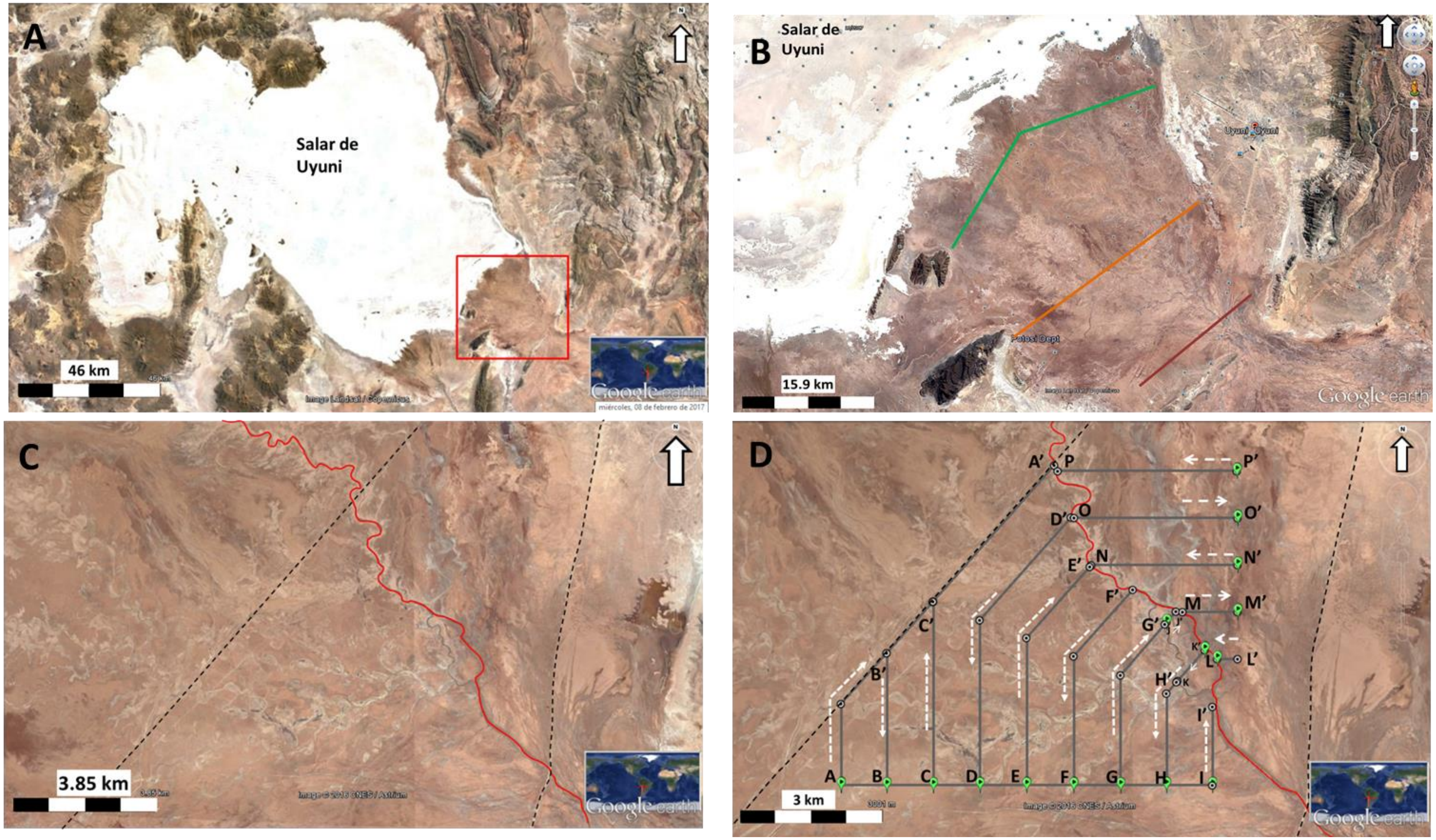

Figure 7. (A) Location of the area of study (red square), at the southeast of the Salar de Uyuni. (B) Proximal (brown) middle (orange) and distal (green) sections of the fluvial fan, ending in the Salar de Uyuni. (C) Present-day river (red line) with floodplain in light brown and the last – abandoned channels in light grey branching shape. (D) Transects traced from S-N, SW-NE and W-E covering an area limited by the national road (dashed line - east) and the railway (dashed line - west). Google Earth Pro Imagery.

3.1.2 Lithological logs

Once the ground relief measurements were obtained, four holes were made in the ground to obtain samples for the lithological description and to find the contact between the lacustrine and the floodplain deposits (*Table 1*). Pick, shovel, scraper and knife were some of the main tools to scope the target. Besides, manual percussion drilling with plastic and steel tubes was necessary to reach the top of the expected contact and to reduce time and energy.

Table 1. Coordinates of the lithology logs taken in the fieldwork

Name	**Coordinates (WGS 84 / UTM zone 19S)**			
	Latitude	**Longitude**	**X**	**Y**
2011-S10	20°34'57.48"S	66°54'25.74"W	718143.08	7722641.28
20161102-FS	20°35'13.85"S	66°51'55.88"W	722476.96	7722081.47
20161102-LC1	20°35'14.00"S	66°51'57.52"W	722429.4	7722077.48
20161104-LAS2	20°31'56.69"S	66°55'13.22"W	716838.81	7728219.31

The next step was to describe the sedimentary features of the fluvial system in a lithology logs, including thickness, grain size, composition, texture and structures (Appendix D) using grain size rulers, hand lens, and measuring tape. Figure 8 illustrates the location of the lithology logs taken in the field, each of them localised in distinctive river shape geometry. For instance, the location of the lithology columns 2011-S10 and 20161102-LC1 described lateral accretion surfaces in point bars (Figure 8C and Figure 8D respectively) and floodplain deposits in 20161102-FS (Figure 8C).

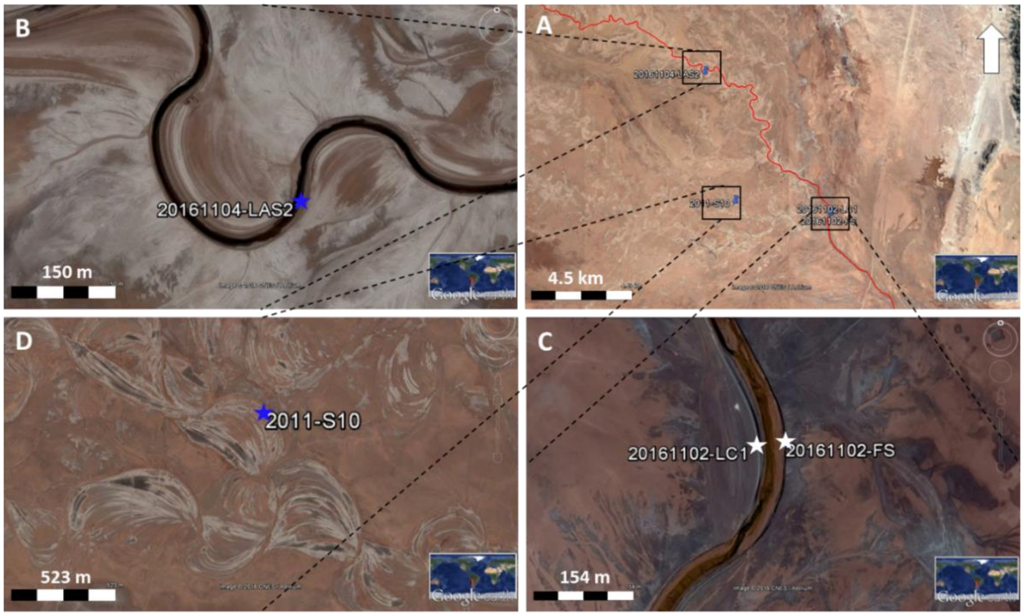

Figure 8. (A) Overview of the recent Río Colorado (red line) and the location of the lithology logs. (B) Lithology log located at the left border of the point bar in the present-day river (C) Location of lateral accretion surface and floodplain (D) Point bar of one of the abandoned channel pathways. .

3.2 Optically Stimulated Luminescence dating

The absolute dating interpretation of several samples along the area, performed by (Donselaar, et al., 2013) and (Donselaar, et al., 2017), is also considered for the analysis of the dGPS data profiles. These authors have used the Optically-Stimulated Luminescence (OSL), a late Quaternary dating technique that can be used to estimate the time since grains of certain minerals (most commonly quartz and feldspar) were exposed to daylight by detecting their subsequent response to environmental ionising radiation exposure (Rhodes, 2011). Throughout geologic time, these mineral grains have been exposed to a luminescence signal (as ionising radiation), stimulating the electrons within the crystal structure. Part of the freed electrons become trapped in this crystal network and accumulate over time (Aitken, 1998).

3.3 Modelling methodology

3.3.1 Regional top and bottom layers of the model

The static model of the modern analogue was built in Petrel. The top layer of the model was entirely constructed with dGPS data from the fieldwork performed in 2016 in the *make surface* tab and using the *convergent interpolation* algorithm. This algorithm is control point oriented (rather than grid point oriented). This means it converges on the solution iteratively, adding more and more resolution with each iteration. This process ensures that general trends are retained in areas with little data while detail is honoured in the area where the data exists (SCM, 2014). *Krigging* and *Minimum Curvature* algorithms were also tried, but the interpolated points followed the direction of the recorded paths or bull-eye shape densities were higher, giving a false representation of the topography in the area.

The distal section of the Río Colorado ceases in the coastal plain of the Salar de Uyuni desert and serves as a reference of the bottom layer that will be considered as the base of the geological model. The bottom of the structure was built using basic geometry to extend the three lowest heights in the regional profiles (Figure 17).

First, the height values were projected to the centre of the fan-shape. Second, the space between the main points was divided into several points separated equally from each other. Third, the components (Ax and Ay) of the vector representing the centre line of the fluvial fan system were calculated as follows:

$$A_{x=}A \times \cos\theta$$

$$A_{y=}A \times \cos\alpha$$

Finally, the points were connected using *convergent extrapolation*. The graphical description of the process is illustrated in Appendix E.

3.3.2 Channel belt polygons in the detailed area

In order to build the static and dynamic model of the fluvial fan, it was considered the highest 57 km^2 of the system, where the rivers were easily demarked, all the OSL samples are concentrated, and the majority of the transects were recorded. This size of the area was also enough to be considered as a modern analogue for the sandstones of the South-Permian

Basin with the Rotliegend feather edge (Donselaar, et al., 2017).

The distribution of the lithology content in the fluvial and floodplain deposits was intended to be represented as realistic as possible. Each of the channel belts of the rivers identified in the Google Earth Pro Imagery was measured and demarked. After that, a line in the centre of each channel belt was drawn to simulate how the reservoir properties decreased from the main channel to the alluvial ridges and terminating with the floodplain deposits (Figure 9).

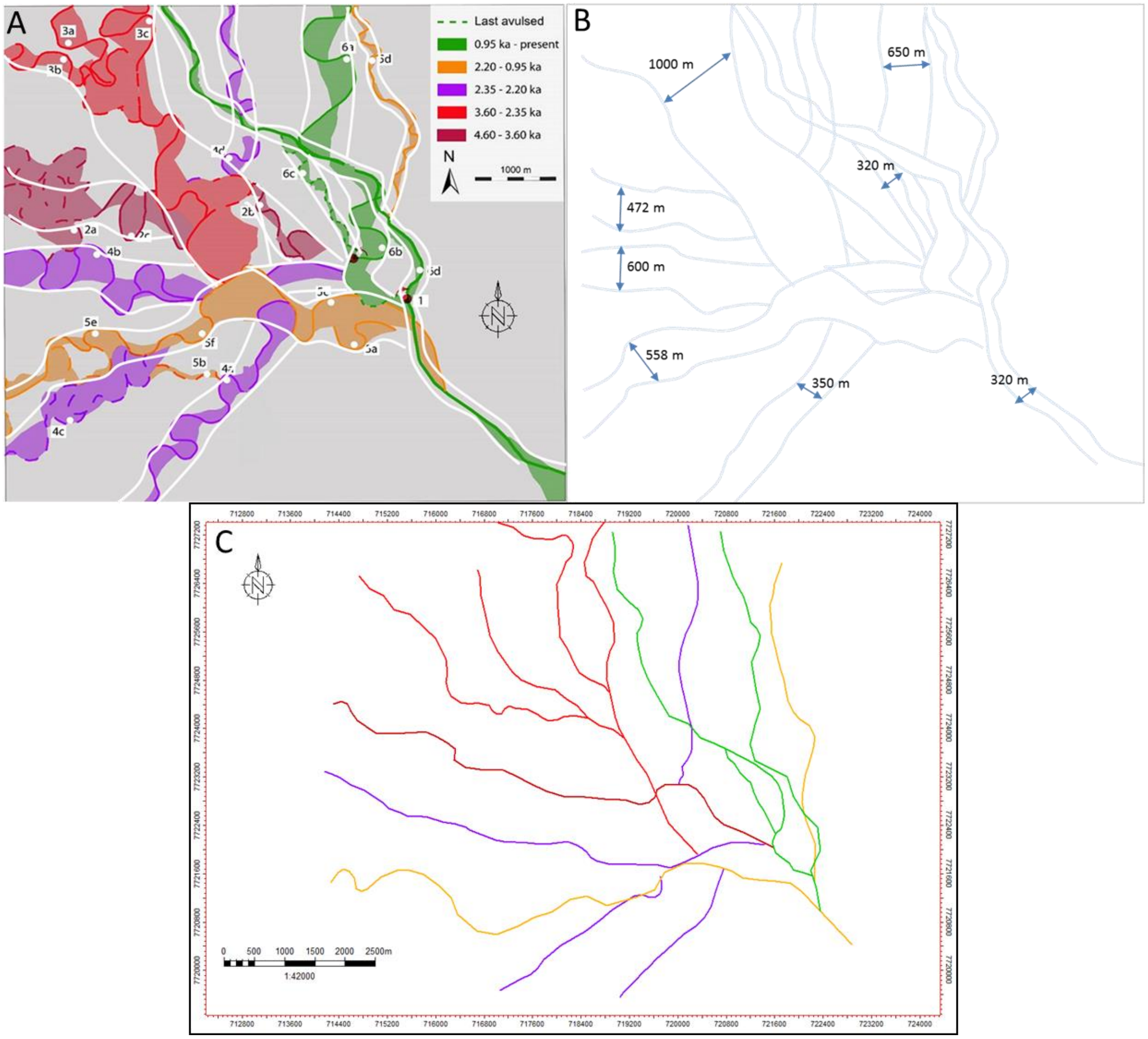

Figure 9 A) OSL samples map modified from (Donselaar, et al., 2017) and the width of each of the channel belts. B) Width for each channel belt. C) Polygons representing the centre of each channel belt

3.3.3 Facies modelling

The wireline log data and core samples from the Pernis West 01 well correlate the Rot Fringe and Solling formations in the subsurface of the West Netherlands Basin onshore with the modern analogue data of the fluvial fan system in the Altiplano Basin, Bolivia. As mentioned before in the geological setting, these formations describe the depositional setting of the fluvial sediments, laying down in a lacustrine and evaporitic framework (Geluk, 1996), which are similar to the conditions in the Río Colorado.

Gamma-ray is extremely helpful because claystones and sandstones usually have different gamma-ray signatures. Appendix F contains 63 gamma-ray readings from the open hole log tools and their associated porosity and horizontal permeability values from the plug samples of the Lower Rot Fringe Sandstone, Lower Rot Fringe Claystone and the Solling Claystone Members. This information is provided by the Geological Survey of the Netherlands at www.nlog.nl.

The crevasse channels and splay deposits were interpreted using core data from the Lower Rot Fringe Claystone and Solling Claystone Members (Boerboom, 2016). However, in order to describe the petrophysical properties in the channel belts, plug samples from the Rot Fringe sandstone member were also considered; where the porosity and permeability are higher than the underlying members (Figure 10). Based on that, porosity and permeability ranges were defined for each of the facies (Table 2).

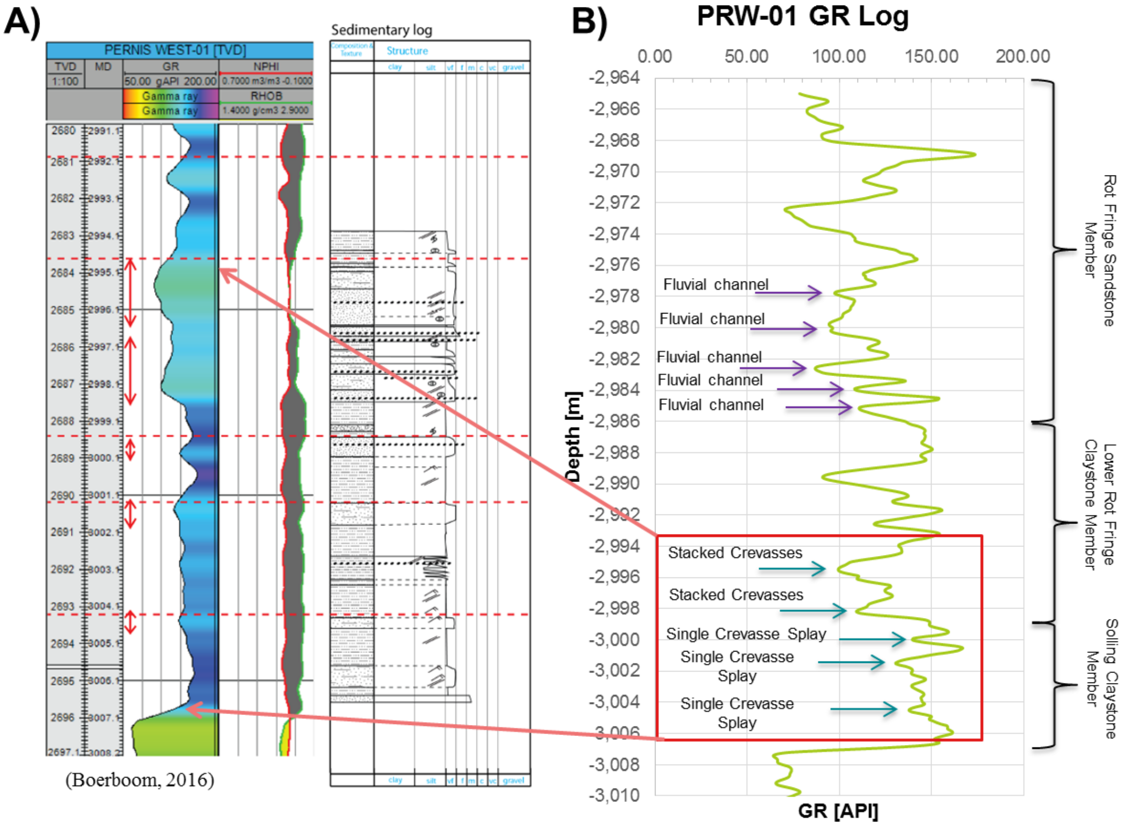

(Boerboom, 2016)

Figure 10. A) Open-hole logs and the sedimentary description of the PRW-01 (Boerboom, 2016) from the Lower Rot Fringe Claystone Member and Solling Claystone Member, compared with B) the fluvial channels from the Rot Fringe Sandstone Member.

Table 2. Porosity and permeability ranges for each facies

Facies	Porosity Ranges [Fraction]	Permeability Ranges [mD]
Channel belt	0.14 - 0.19	35 - 154
Crevasse splay deposits	0.09-0.14	0.6 - 35
Floodplain (Fines)	0.04-0.09	0.06 - 0.6
Floodplain (Clay)	0 - 0.04	0 - 0.019

Comparing GR with porosity and permeability, it was found that the lowest GR does not necessarily has the highest porosity and permeability values. However, this model has the purpose to populate higher porosity and permeability values in the centre of the channel belts (Figure 9), and decrease these petrophysical properties to the edges of the fluvial deposits. Based on that, the porosity was the property used to correlate with distance.

For the property modelling, *distance to object* was the method used to distribute the petrophysical parameters. A width of 1500 meters was considered for the alluvial ridges (on average, according to what was observed from the dGPS profiles). Therefore, 750 m to one side of the channel is the edge of the wing, before reaching the floodplain. Based on that,

$$\frac{750\ (meters)}{63\ (data\ points)} = \sim 12$$

This means that the property was decreased every 12 meters as the sediments moves away from the polygon. Once the GR values reach the end of the alluvial ridge, the property became zero (representing the clay in the floodplain).

3.3.4 Production behaviour

More than 20 wells were distributed around the model to simulate a real gas field, starting its production in 2017 and evaluating the performance during the next six years; analysing gas and water production in pure pressure depletion or with the influence of a bottom aquifer. However, only 6 of these wells were included in the results and subsequent analysis; taking two from each facies. Different production cases designed in Petrel were simulated in Eclipse.

4. Results

Multiple repetitions of avulsion pattern were observed in an area of approximately 400 km^2. Regional and local transects were used to measure top-level topography, describing the fluvial sediments on top of the lacustrine deposits (yellow and brown lines respectively, Figure 11B). This morphology was the skeleton used to construct the geological model.

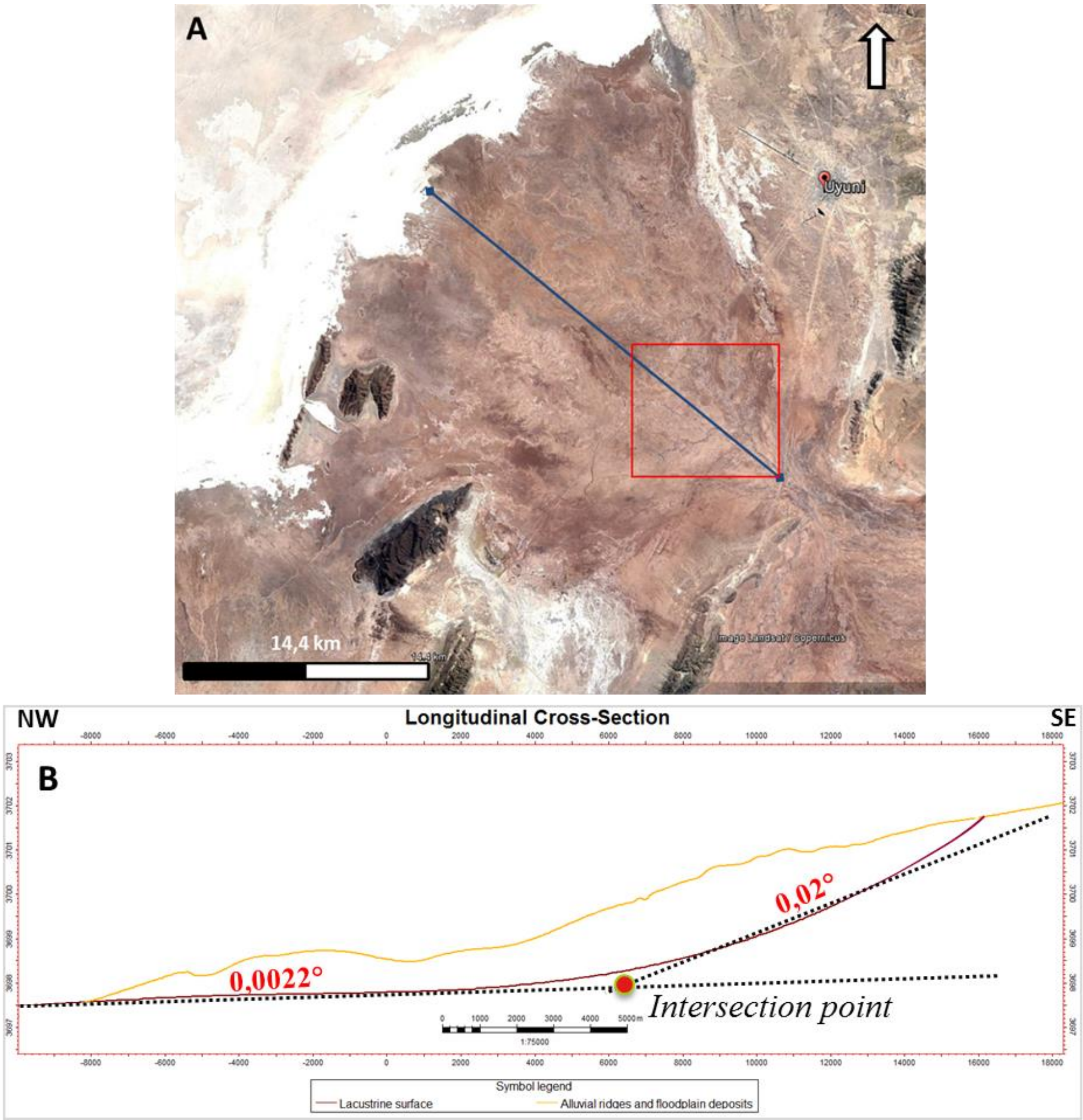

Figure 11. A) The regional cross section from NW to SE and the detailed area (red square). B) Gradient profile from the apex of the fluvial fan towards the Salar de Uyuni.

4.1 Lacustrine-fluvial interface

The lacustrine-fluvial interface has an average gradient profile of 0.00012 over approximately 25 km. In the longitudinal cross-section, it was observed a very gentle gradient slope, changing from 0.02° at the inclined section (from the southeast at the apex of the fan) to 0.0022° in the flattened section towards the Salar de Uyuni (Figure 11B).

4.2 Detailed area

In total, 19 profiles were measured in the fieldwork. 16 of them were recorded in an area where the Río Colorado started avulsing, concentrated in a detailed region of around 57 km^2 (Figure 7D, Figure 12 and Appendix C). Figure 12 is labelling the river evolution according to the absolute age dating OSL samples (Donselaar, et al., 2017). Each age was recognised by an assigned colour, starting from the oldest in the sequence with dark red and ending with the present river in green.

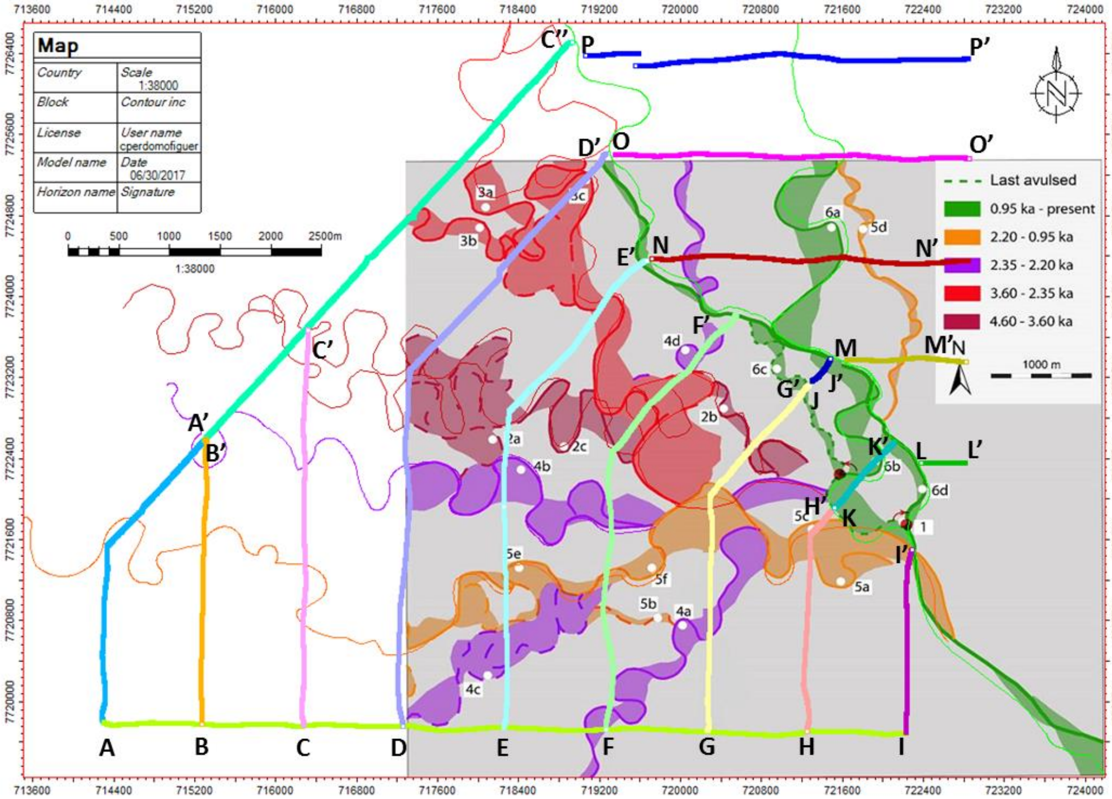

Figure 12. Río Colorado flow paths and OSL samples location, overlapped by transects and polygons of the interpreted rivers in the detailed study area. Modified from (Donselaar, et al., 2017)

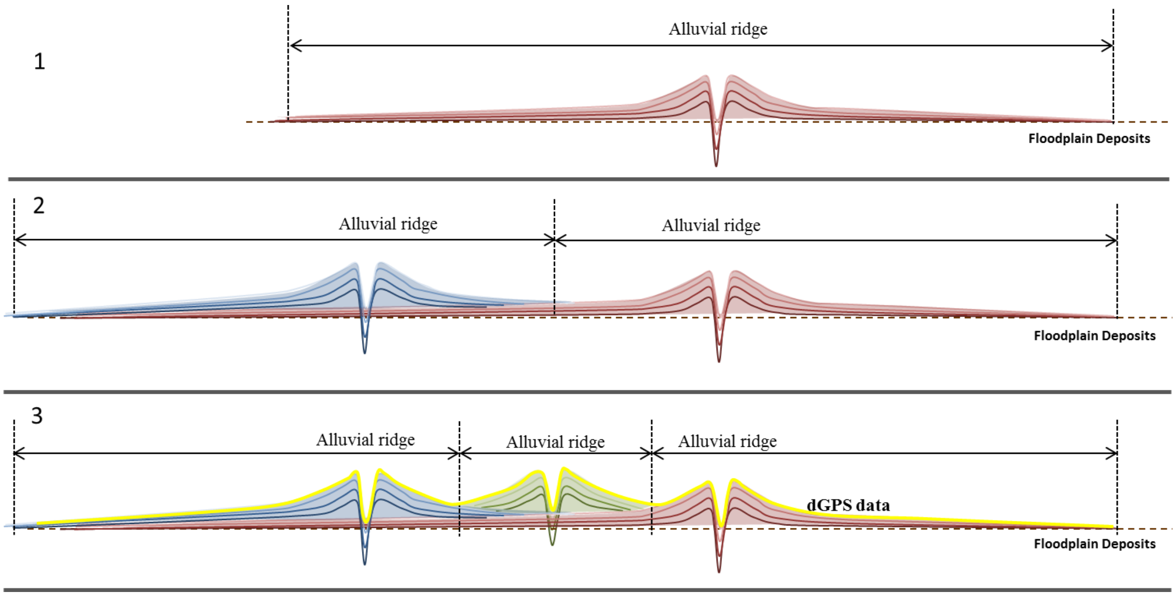

Figure 13. Schematic representation of the laterally-amalgamated alluvial ridges (not to scale). The yellow line is representing the dGPS data, showing the reason why it is difficult to delimit each side of the alluvial ridges.

The sketch in Figure 13 is a schematic representation of the laterally-amalgamated alluvial ridges, describing an alluvial ridge on top of older fluvial sediments. It explains the reason why the complete extension of the channel wings (a term associated alluvial ridges by (Mohrig, et al., 2000)) and the compensational stacking are not always observable in the dGPS data. The merged profiles in Figure 15 and Figure 16 described channels confined by their respective levees and elevated above the surrounding floodplain during the last 4000 years.

Starting at the apex of the fluvial system in the southeast of the fan with merged profile H-H’, K-K’ and L-L’, the OSL samples and the dGPS data allowed to observe only two alluvial ridges of the most recently avulsed rivers: the 2.29 to 0.95 ka and the present-day river. The southern picks in profile H-H’ belong to the crevasse splay deposits coming from the present-day river (Figure 14).

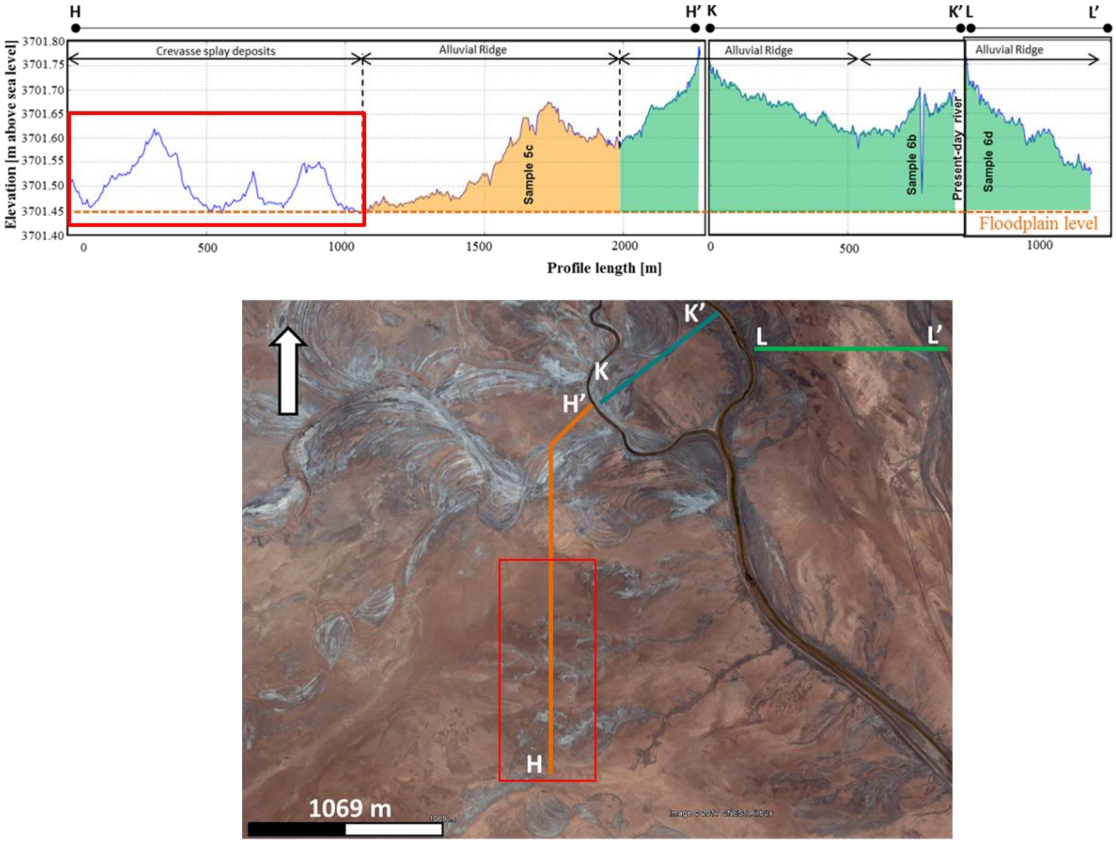

Figure 14. Crevasse splay deposits (red square) derived from the present-day river.

The next merged profile is separated 1 km to the west from the previous profile is G-G', J-J' and M-M' (Figure 15). It allowed to observe: 1) older river activity (sample 5d) to the east side of the present-day river, 2) the oldest river with sample 2b (4.60 – 3.60 ka) below the sample 5c and 6c and 3) the branch of sample 4a (2.35 to 2.30 ka). Evidence of ancient river activity was possible due to the divergent pattern of the Río Colorado with sample 6c and 6c (the youngest in the record), avoiding positive relief from the river with sample 2b.

Continue moving to the west (Figure 16), the development of the Río Colorado with sample 3c (3.60 – 2.35 ka) to the east side of the river with sample 2c (4.60 – 3.60 ka) in profile E-E' was observed. The expression of its evolution was detected moving farther to the west, with profiles D-D' and A'-C'' (shifting to sample 3b and 3a). The same tendency was recognised in the river with sample 4b and 4c (2.35 – 2.30 ka) in profiles E-E', D-D' and A-C''. The development of this river (purple colour) to the west-southwest of the fluvial fan left enough space for the deposition and aggradation of the river with sample 5e.

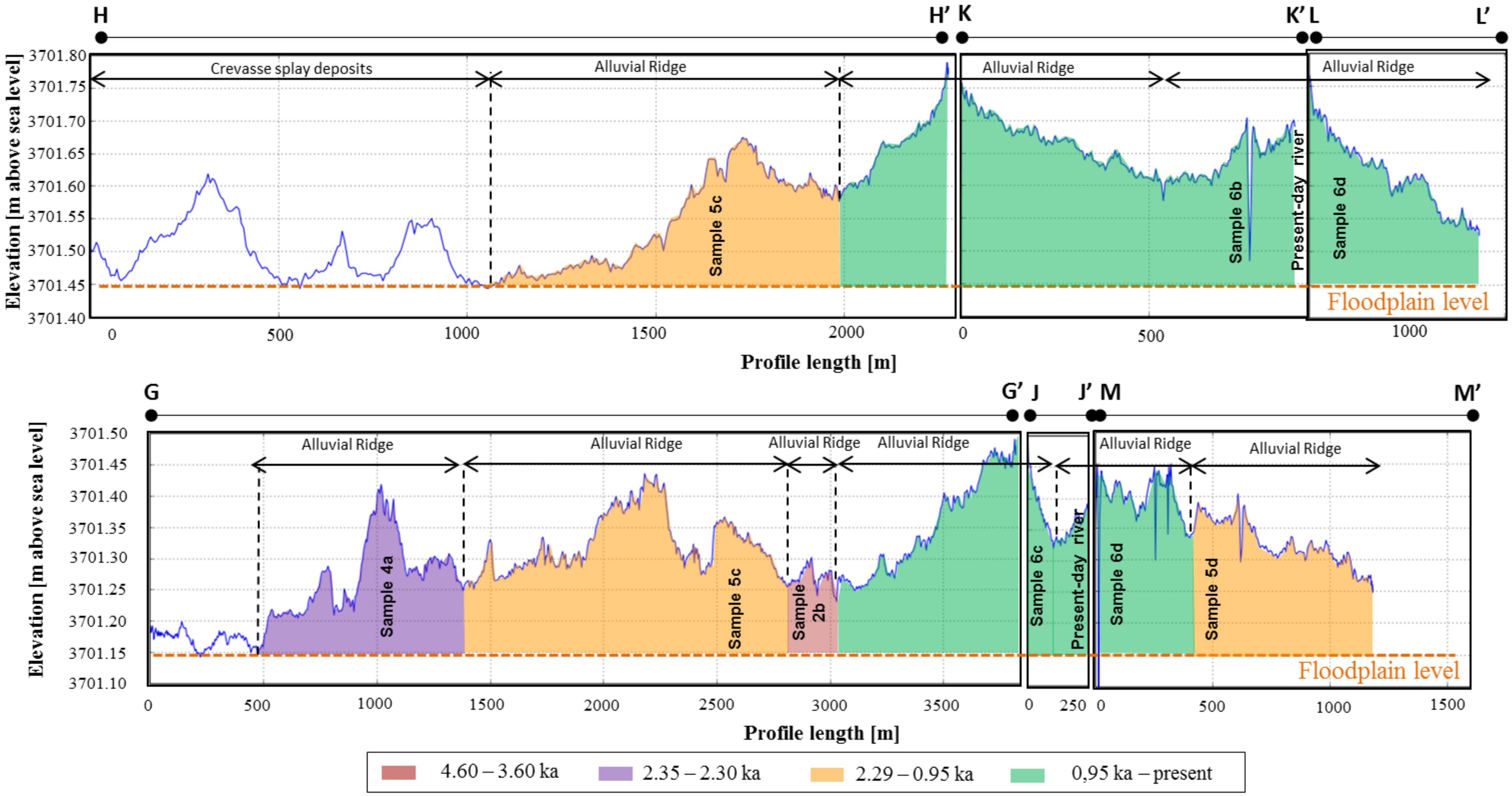

Figure 15. Merged profiles from SE to NW (see Figure 8 as a reference for the location). The colours are representing avulsion rivers, based on OSL samples from (Donselaar, et al., 2017)

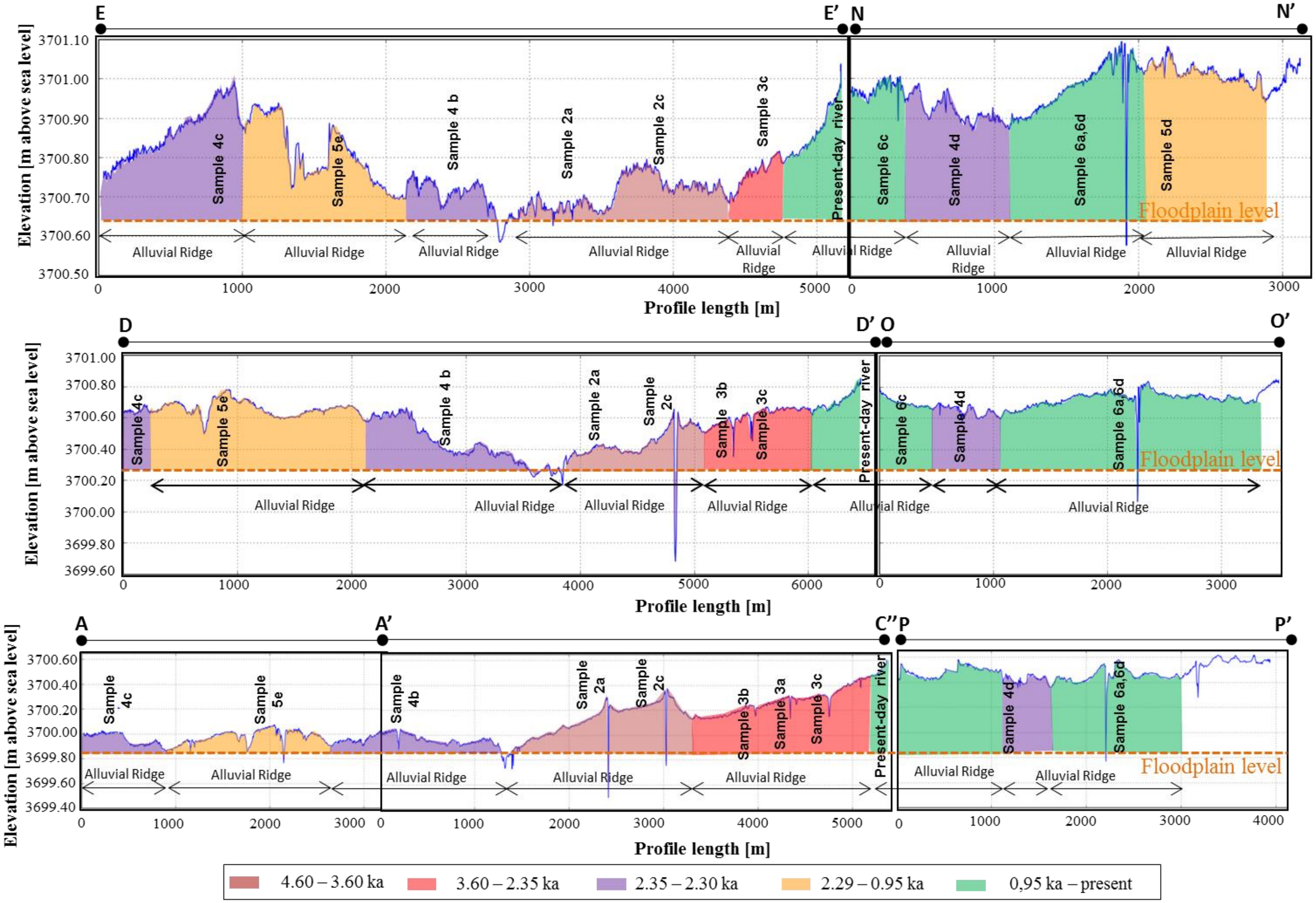

Figure 16. Continuation of the merged profiles from SE to NW (see Figure 8 as a reference for the location in the detailed area). The colours are representing avulsion rivers, based on OSL samples from (Donselaar, et al., 2017)

4.3 Regional transects

Three regional transects (Figure 17) were measured in an area of approximately 400 km^2 (Figure 7B and Appendix C). It allowed to extend the shape of the fluvial fan system heading to the Salar de Uyuni and to identify the lacustrine deposits (red dashed line) underlying the sedimentary architecture of amalgamated alluvial ridges and aggradation of floodplains. The dashed-line reference layer can be equal or higher than the lacustrine deposits, and it is part of the discussion in the next chapter of this report.

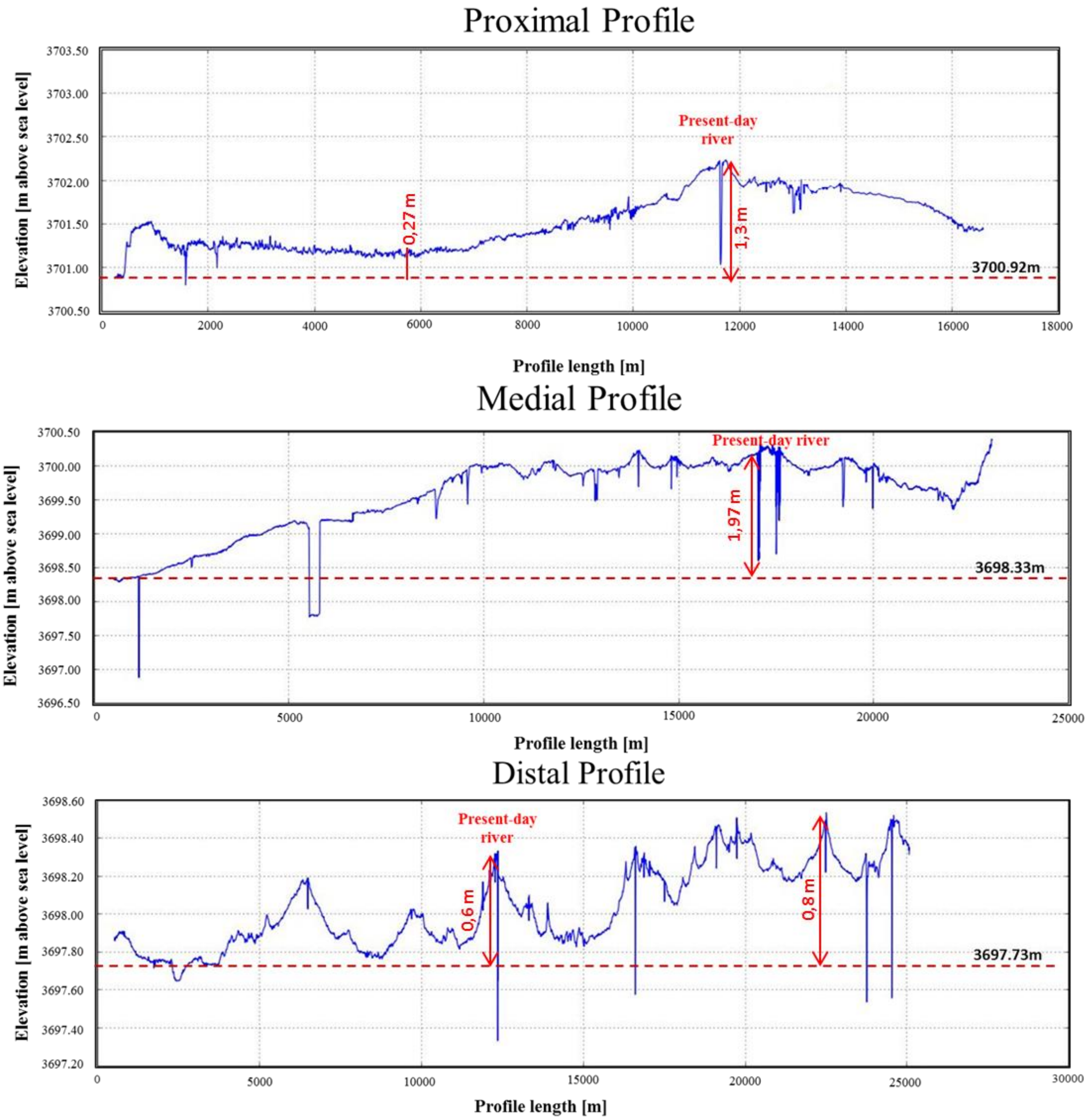

Figure 17. Regional transects from proximal to the distal section. The dotted lines represent the bottom layer below the fluvial sediments, used to build the static model.

The reference level to be considered as the bottom layer of the model was defined observing the lowest height in the dGPS measurements (not necessarily the fluvial-lacustrine contact). The thickness between the top of the fluvial deposits and the bottom layer differs from proximal to the distal section, finding the thickest succession of the present-day river fluvial deposits in the medial profile (almost 2 meters). As observed in section 4.1 of this chapter, the present-day river in the apex of the proximal transect is thinner respect to the medial section but thicker compared to the distal profile. Note that the present-day river is the highest channel along the proximal and medial transects, differing from the distal transect, where the active river has switched its path to the southwest, avoiding the elevated topography at the northeast (Figure 17)

It is important to notice that the reference level extracted from the regional profiles did not match with the contact found in the sedimentary log 2011-S10 (Appendix D), 2.80 m below the fluvial sediments. That difference will be explained later on in the discussion.

4.4 Lithology logs

Four lithological logs were taken in the present-day river and abandoned channels during the acquisition campaign, attached in Appendix D. Only one log is describing the complete section of the fluvial sediments and the contact with the lacustrine deposits (2011-S10). Starting from the bottom, a lacustrine clay is interbedded with fine-grained sand, with diatoms with 0.3 mm of diameter. Overlying this deposits, a fining-upward sequence from fine to very-fine fluvial sands were described (20161102-LC1 and 20161104-LAS2 logs). Ripple-laminated, simple cross-bedded and parallel-bedded sedimentary structures were observed (Figure 18). Gypsum crystals and salt cement cover the top of the sequence. However, a heterolithic section of sandstones, siltstones and claystones was described from the middle to the top of the in 2011-S10 log. Although the grain size of the section is fine-very fine to silt, the net to gross was defined as 0.9 in the model; and only the salt cement at the top was discarded.

Figure 18. Parallel-bedded sedimentary structures observed in the fluvial deposits.

4.5 Reservoir Geology

4.5.1 Static modelling

4.5.1.1 Regional top and bottom layers

The dGPS data recorded in the field were the basis to construct the top and bottom of the fluvial fan system. Figure 19 describes the regional layers for the fluvial and lacustrine deposits, covering an area of around 400 km^2. The squared shape in the figure highlights the detailed area and the focus of the static and dynamic modelling

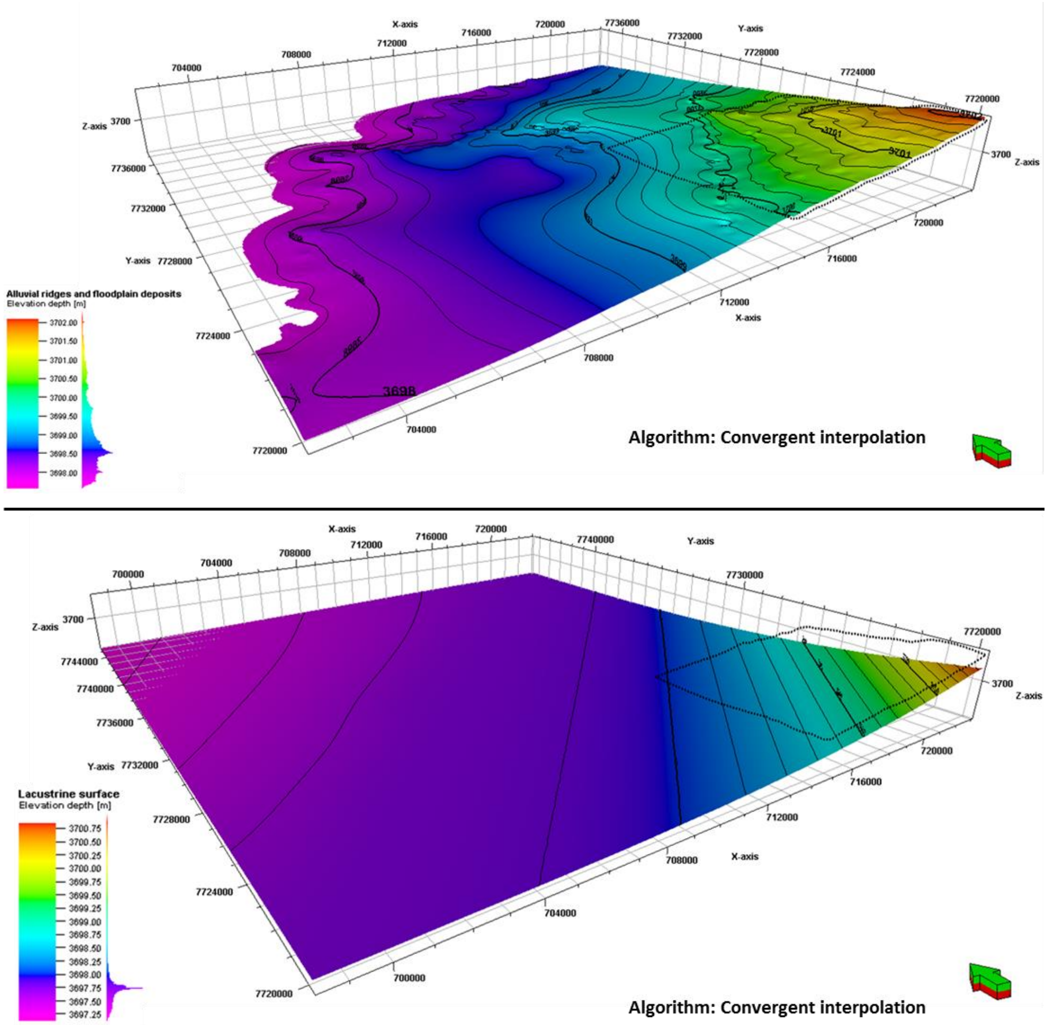

Figure 19. Regional top and bottom layers, describing the shape of the fluvial fan system and the lacustrine deposits respectively.

4.5.1.2 Detailed region

Figure 20 illustrates the topographic map of the fluvial deposits recorded with the dGPS, showing the fan-shape with the apex of the fluvial system (red colour) and how was possible to distinguish the paths created by each river, even with the centre polygon of the channel belts.

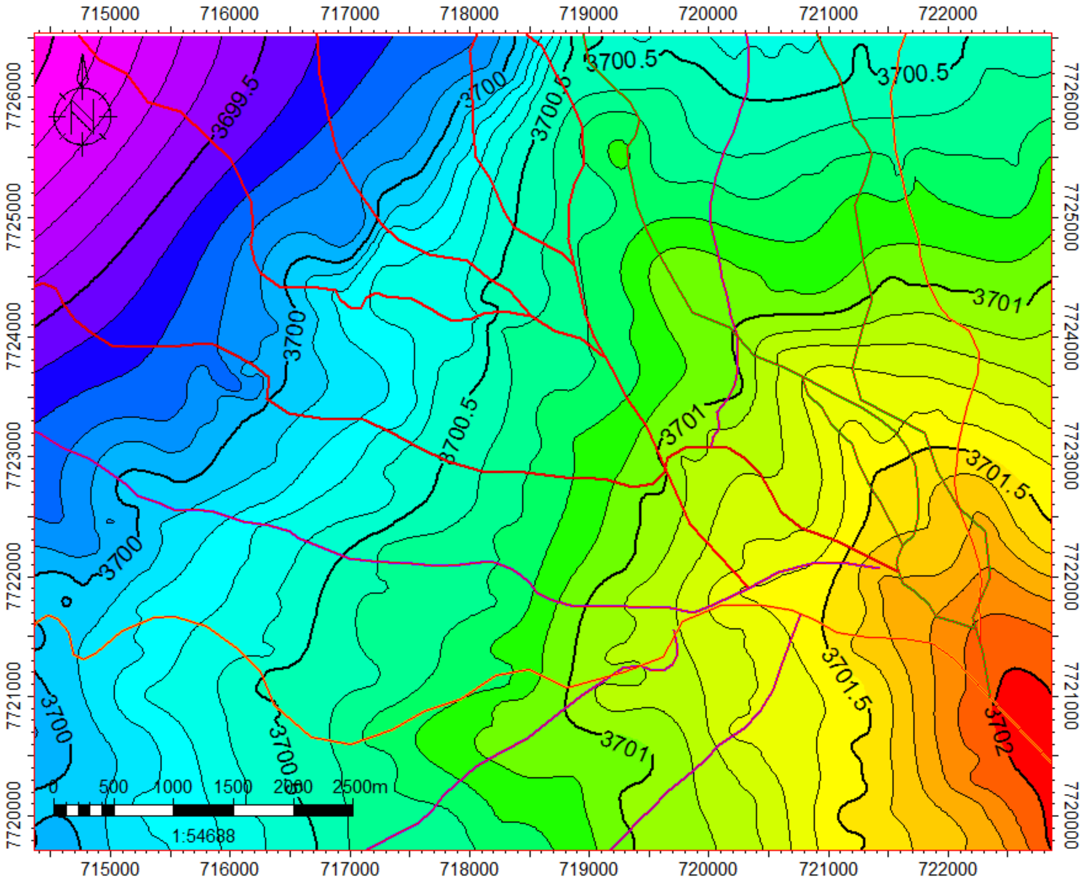

Figure 20. Topographic map of the fluvial deposits recorded by the dGPS data and the polygons representing the centre of the channel belts.

4.5.1.3 Property modelling

Two correlations were obtained from the core data analysis. First, a correlation between porosity and distance is illustrated in Figure 21, resulting in the following exponential function:

$$y = 0.1756e^{-0.002x}$$

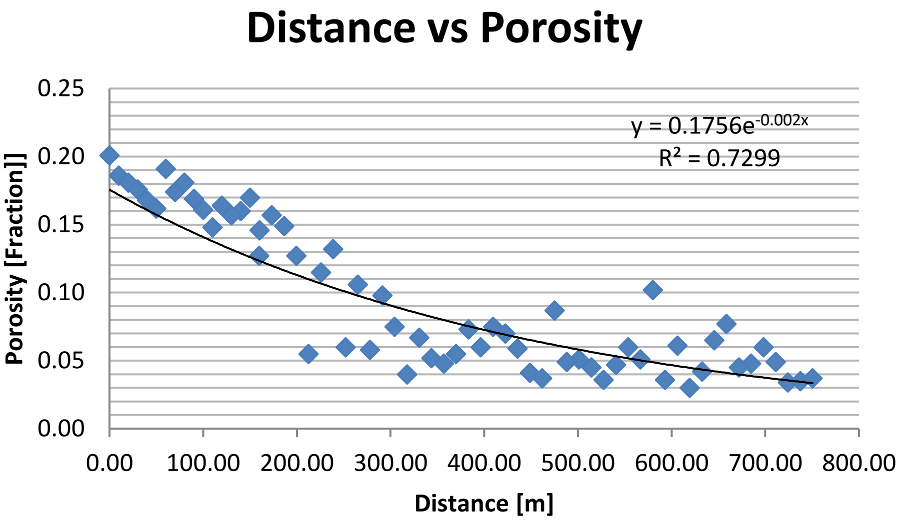

Figure 21. Correlation between distance and porosity with an exponential function.

The result porosity map with polygon trends of channel belts is illustrated in Figure 22

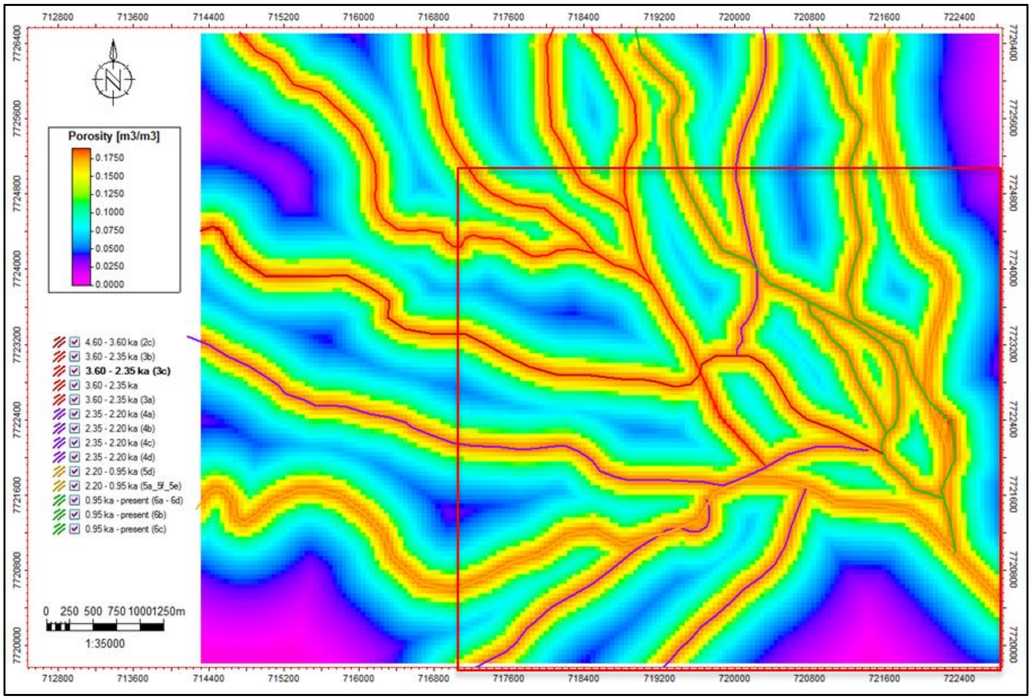

Figure 22. Porosity map with polygon trends for each of the channel belts. The red rectangle is the limit of the area used by (Donselaar, et al., 2017) to analyse the channels and the OSL samples

Once the distance vs porosity function was obtained, an exponential function $k = 0.0052e^{55.84\,\phi}$ is calculated based on the porosity vs permeability correlation in Figure 23. This function was used to populate the permeability values in the model Figure 24

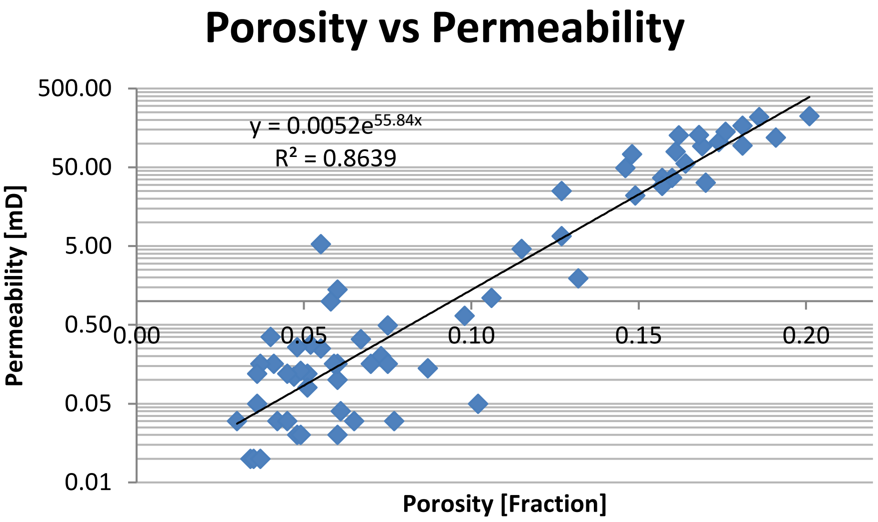

Figure 23. Exponential function of porosity and permeability correlation from core plug samples

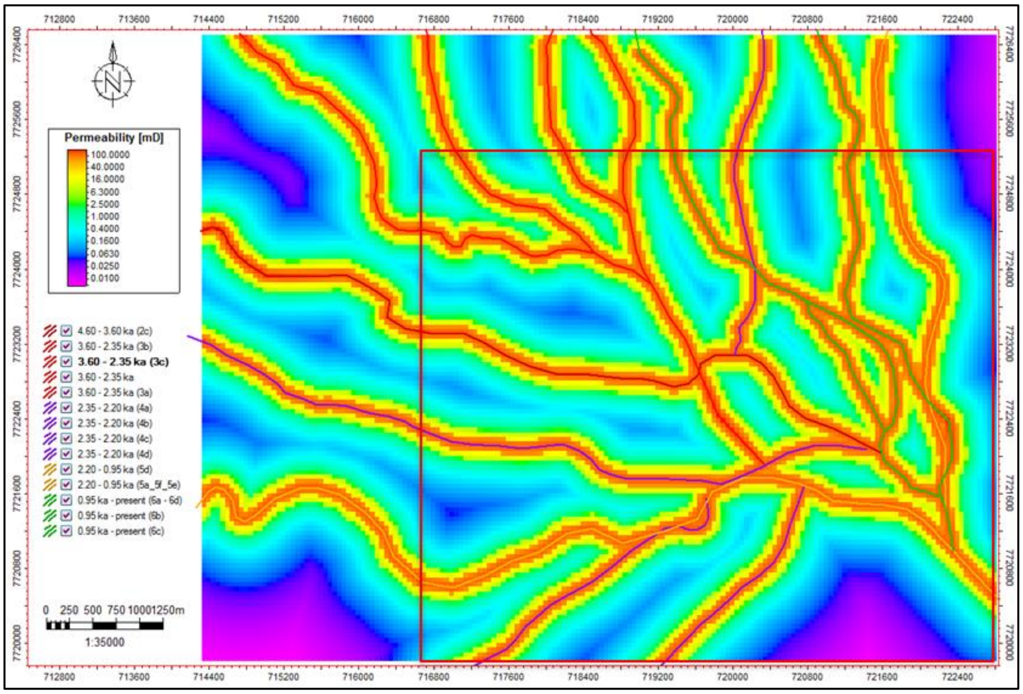

Figure 24. Permeability map with polygon trends for each of the channel belts. The red rectangle is the limit of the area used by (Donselaar, et al., 2017) to analyse the channels and the OSL samples

4.5.1.4 Gas Initially In Place (GIIP)

The volume calculation was performed in Petrel, using the *reservoir engineering tab*. The gas and water saturation were defined as 0.7 and 0.3 respectively; based on the relative permeability curves provided by the shaly-sand presets in Petrel. For a hydrocarbon-filled reservoir, the ultimate free gas saturation has an average $S_g = 30\%$ (Lyons & Gary, 2005) The Gas Expansion Factor (Eg) was calculated assuming a reservoir depth of 11052 feet (to fulfil the preset requirements for dry gas) divided by 36.9 for normal hydrostatic pressure reservoirs (Torres Carranza, 2013). The gas Formation Volume Factor (Bg) is the inverse of the Eg; therefore,

$$B_g = \frac{1}{11052/36.9} = 0.0033$$

The rest of the parameters used for the volume calculation are described in Table 3.

Table 3. Parameters for the Volume calculation P10, P50 and P90

Parameter	P10	P50	P90	Unit
Gas Saturation	0.7	0.7	0.7	[-]
Water Saturation	0.3	0.3	0.3	[-]
Porosity	From model	From model	From model	[Fraction]
NTG	1	0.9	0.5	[-]
Expansion Factor	257.8	299.523	368.2	[Std m3/res m3]
Gas Formation Volume factor (Bg)	0.0027	0.0033	0.0038	[sm3/sm3]

The Gas Initially In Place (GIIP), defined as the volume of gas in a reservoir before production, was calculated with the following formula:

$$GIIP = BRV * NTG * \varphi * S_g * B_g$$

Considering the Bulk Rock Volume (BRV) as the product of the area and the gross thickness of the reservoir, and the Net to Gross (NTG) as the way to indicate the economic value of a reservoir respect to the total gross thickness. The results of the GIIP calculated for P10, P50 and P90 are expressed in Table 4.

Table 4. GIIP calculated for P10, P50 and P90 in Petrel

Parameter	P10	P50	P90	Unit
Bulk Volume	98	98	98	[*10^6 m3]
Net Volume	49	88	98	[*10^6 m3]
Pore Volume	5	10	11	[*10^6 rm3]
HCPV	4	7	8	[*10^6 rm3]
GIIP	**969**	**2052**	**3009**	[*10^6 sm3]

P10 and P90 were also calculated, to have the complete range of uncertainty. The worst case scenario is considering a reservoir pressure of 300 bar and a reservoir temperature of 60 Celsius. The best scenario involves a reservoir pressure of 480 bar and 100 Celsius.

4.5.2 Dynamic modelling

The static geological model of the fluvial fan represents the reservoir before starting its production. In this section, the model was tested to have an idea of how the fluid flow properties would behave in the subsurface. Also, to decide the strategy to be implemented to produce these types of reservoirs regarding fluid rates, reservoir pressure, number of producer wells and the lifetime of the field.

4.5.2.1 Fluid model

A gas-water contact has been defined by the structural lowest depth found at the bottom layer of the model (3697.95 m). Boerboom, 2016, defined a gas water contact for his model based on a gradient test found in a pressure survey report of BTL-01 well. This well is part of the West Netherlands Basin, the same subsurface analogue used in this study. Therefore, it was assumed that the fluvial fan reservoir contains a gas-water contact.

The preset conditions for a dry gas defined in Petrel were used to construct the fluid model of a gas phase, assuming the reservoir conditions described in Table 5. The temperature of 76.85 °C is very similar to the reservoir temperature of 77.5 °C calculated for the reservoirs in the Netherlands, based on the average thermal gradient of 31.3 °C/km (Bonté, et al., 2012).

Table 5. Preset reservoir conditions in the fluid model for a Dry gas

Reservoir conditions		
Parameter	**Value**	**Unit**
Minimum Pressure	80	[bar]
Maximum pressure	350	[bar]
Temperature	76.85	[degC]
Reference pressure	215	[bar]

4.5.2.2 Rock Physics functions

Based on previous studies from the same analogue formations, the irreducible water saturation has been set as $S_{wirr} = 0.3$ (Boerboom, 2016). The saturation model was built considering the preset values for a shaly-sand in Petrel, for both gas and water phases. The presets for consolidated sandstone were used in the compaction model.

4.5.2.3 Well design and placement

Each well was manually designed, including three main basic components: a casing (0.17 m), tubing (0.127 m) and perforation (covering the entire thickness of the reservoir). In total, 24 vertical wells were placed from the middle to the highest part of the fluvial fan (Figure 25). The lowest area was not used for the location of the wells to avoid an early water breakthrough. The wells were named Uyuni's, and they were occupying the centre of the channel belts, crevasse channels and splay deposits and the edges of the fan with floodplain sediments (purple areas in Figure 25).

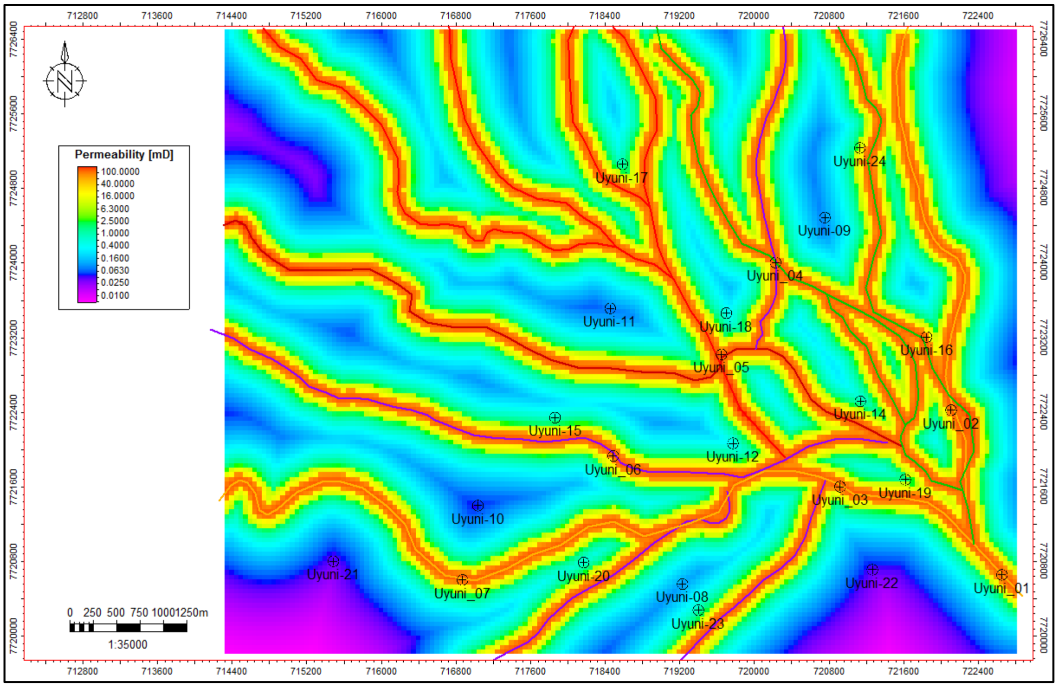

Figure 25. Permeability map and the location of the 24 wells around the study area.

The number of simulations was reduced to some wells, representing each of the facies: Uyuni-03 and Uyuni-05 for channel belts, Uyuni-15 and Uyuni-24 for crevasse splays and Uyuni-11 and Uyuni-22 for floodplain deposits.

4.5.2.4 Development strategy

The production life of the field was limited to 6 years, starting on June 15th of 2017 and ending on June 15th of 2023. This period was set because these type of reservoirs are considered as secondary targets and not as the main target (where the period is longer to pay back the initial investment). Each of the selected wells was evaluated under different production rates, trying to find the optimal flow rate that could maximise the recovery factor.

For the production control, the rule *well rate production control* was chosen, and the tubing head pressure was defined based on the recommendation written by (Bisdom, 2016), describing this method as the most realistic way of controlling the wells, compared to the bottom-hole pressure.

Several gas production rates considered in each well are included in Appendix G, starting with 700,000 sm3/day and reduced up to 10 sm3/day when the permeability was insufficient to allow the gas to flow. Based on that, different simulation cases we obtained for each facies.

4.5.2.5 Simulation Cases

In Petrel, the *simulation* tab allows to define cases, considering the parameters in the fluid model, the relative permeability drainage curves preset for the shaly-sand model and the development strategies designed for each gas production rate. Once each of the cases was defined, the results were exported into *Eclipse.*

The complete results of the gas production rates and outflow through wells are attached in Appendix G. However; Table 6 covers the most efficient production rates for the wells representing each facies. Based on that, parameters like water saturation (S_w) and pressure depletion changing through time were obtained, supplying enough information to understand the production behaviour and the radius drainage area, depending on the location of the well in the fluvial system (analysed in the next chapter) and its related permeability.

Table 6. Most efficient gas production rates based on the highest recovery factor obtained from Eclipse.

Well	Prod. Rate [sm3/day]	Outflow through well [sm3]	Recovery Factor
Uyuni-05	300,000	249,480,641	0.20
Uyuni-03	500,000	175,357,048	0.14
Uyuni-24	35,000	81,807,923	0.07
Uyuni-15	6,500	8,281,415	0.01
Uyuni-11	185	432,105	0.0003
Uyuni-22	10	12,897	0.0000

Uyuni-05 well

The location of the well in the centre of the fluvial fan permits to have a preferable drainage from the channels oriented from northwest to southeast (Figure 26), with higher S_w changes in a radius of approximately 1.5 km, where the higher permeability from the main channels is the main contributor to the gas production. Moreover, it is also possible to observe the expanding production radius at the distal part of the system at the end of the production from channels that were not contributing since the beginning. However, observing the streamlines map of the production in Uyuni-05 (Figure 27), it is noticed that the fluid contribution is not only coming from the main channels, but also from the alluvial ridges bordering them. However, the flow is weak and it does not represent a major influence in the cumulative production of the well.

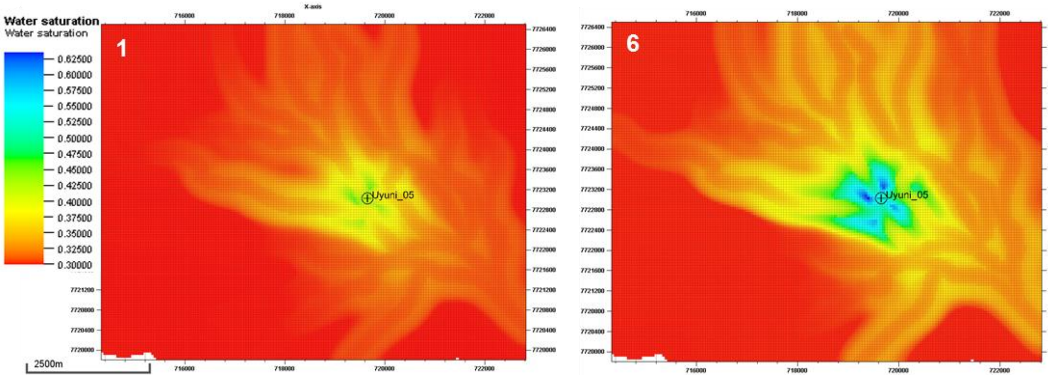

Figure 26. Water saturation maps comparing the first (left) and last year (right) of production in Uyuni-05

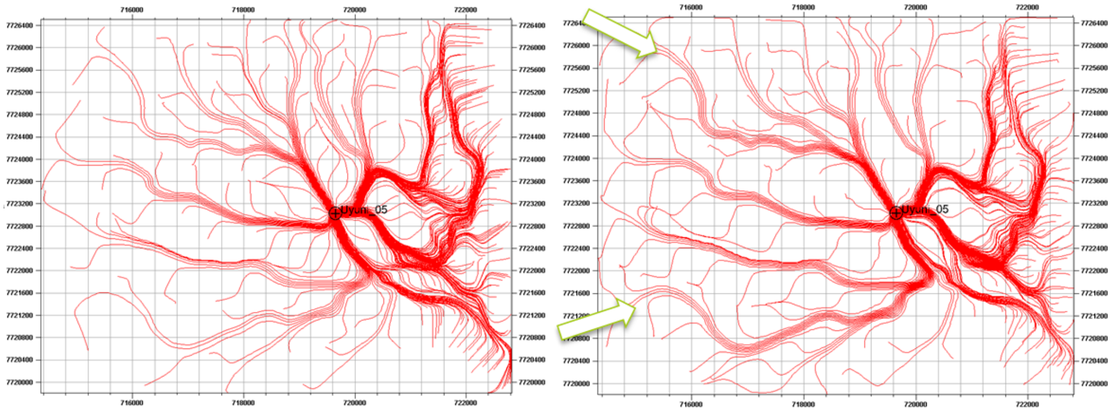

Figure 27. Streamlines map of the production of Uyuni-05. The fluid flow pattern is illustrated from the first sixth months (left) until the sixth year (right) of production. The arrows indicate channels that are supplying more fluid at the end than at the beginning of the production life.

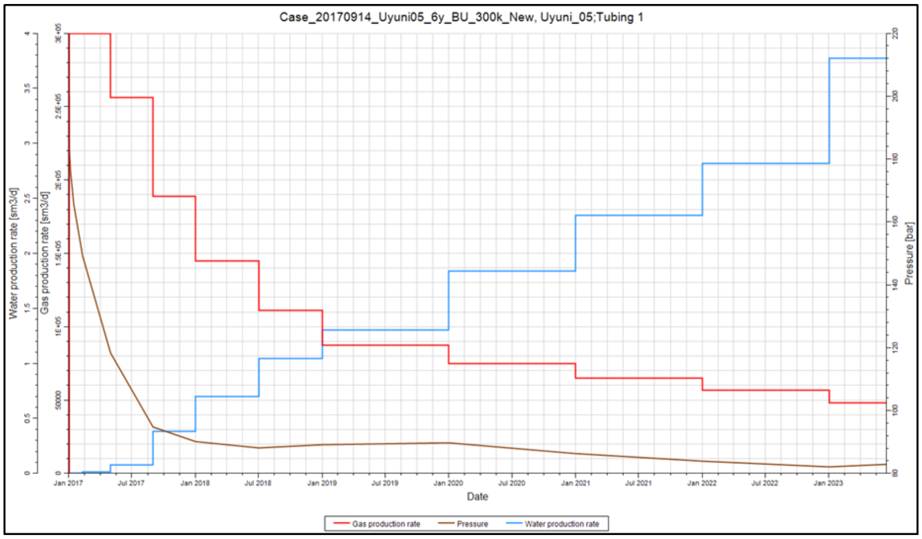

Figure 28. Uyuni-05 well production chart for 300,000 sm3/d

The production chart in Uyuni-05 (Figure 28) expressed a gas and pressure depletion at the early stages of the production, starting with 300,000 sm3/day and finishing with approximately 50,000 sm3/day, obtaining a recovery factor of 0.20. Lower rates were evaluated to avoid the drastic depletion, but the recovery factors obtained were significantly lower (Appendix G). Also, based on the graphic, a water breakthrough seems to occur at the beginning of the year 2019. However, the scale is very small, and the water production is negligible.

Uyuni-03 well

This well, located at the apex of the fluvial fan system (highest structural part), receives less pressure support from the aquifer (Figure 29). Some of the proximal channels at the south of the well, identified with OSL samples 4a and 4c (Figure 12), are the bodies with faster water saturation and pressure depletion, and new streamlines appeared at the west-northwest due to the bottom water drive (Figure 30). The drainage radius of 2 km is higher than Uyuni-05, but the fluid flow is channelised mainly by these two channels mentioned before. The rest of the system did not change in pressure and saturation.

The streamlines of the well production allowed observing some changes in the fluid pattern. For instance, the fluid flow in the southern channel (red square in Figure 30) is higher at the beginning of the production, but at the end, it losses the pressure support and therefore, the streamlines are weaker. On the other hand, new streamlines appear at the northwest due to the increment of pressure from the aquifer.

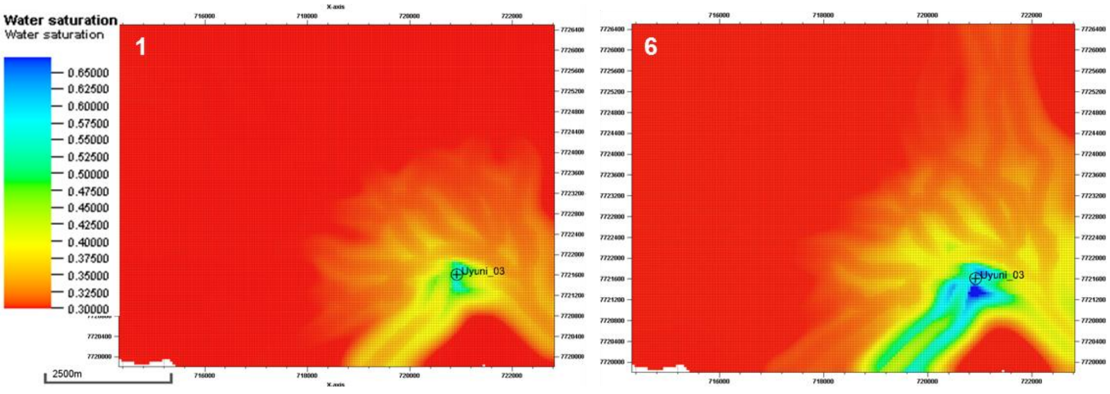

Figure 29. Water saturation maps comparing the first (left) and last year (right) of production in Uyuni-03

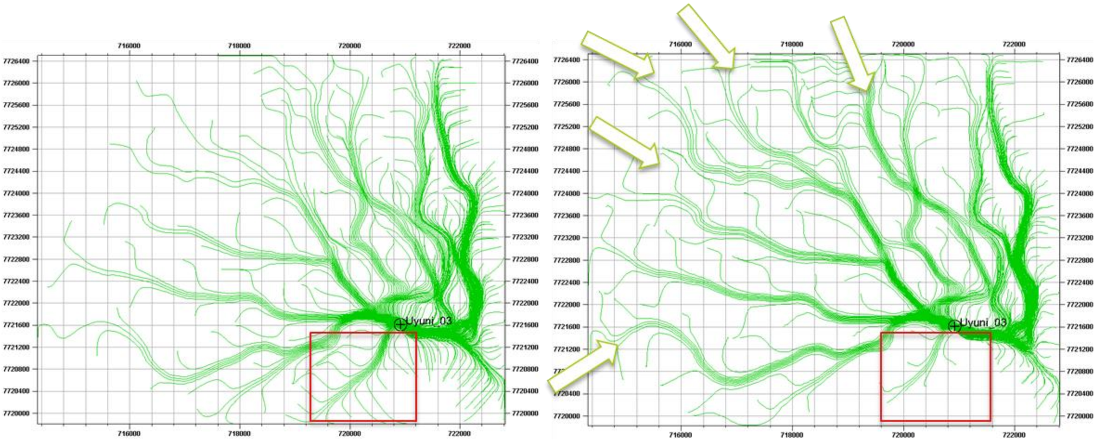

Figure 30. Streamlines map of the production of Uyuni-03. The fluid flow pattern is illustrated from the first sixth months (left) until the sixth year (right) of production.

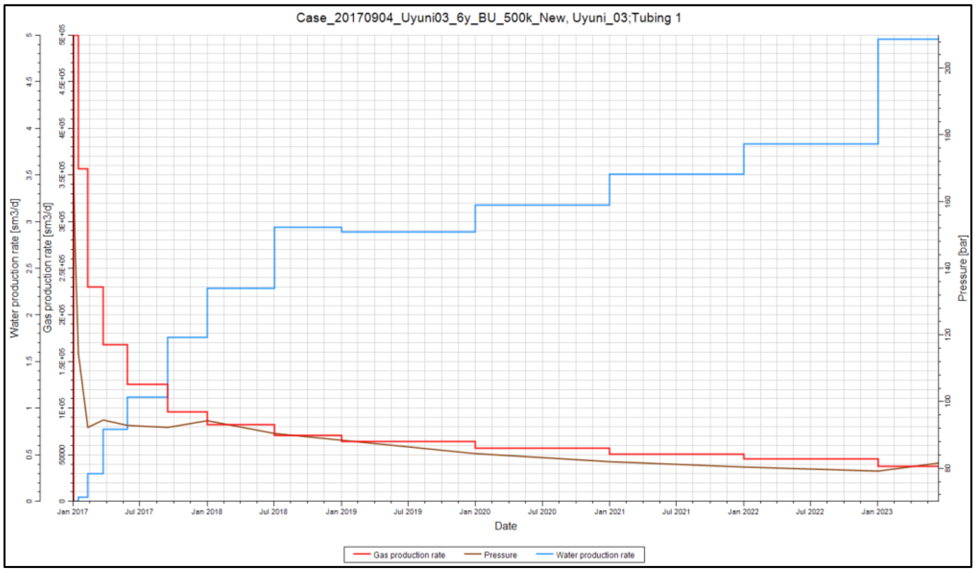

Figure 31. Uyuni-03 well production chart for 500,000 sm3/d

The production behaviour (Figure 31) is similar to Uyuni-05, starting with 500,000 sm3/day and finishing with approximately 50,000 sm3/day, reaching a steady-state condition. However, unlike the Uyuni-05, Uyuni-03 does not reach the same amount of gas outflow. Its maximum recovery factor was 0.14, attributed to the long distance that exists between the well location and the bottom water drive and the cornered position at the southeast of the system, isolating the well to the rest of the channel belts in the region. The water production is negligible, as explained in Uyuni-05, with very low water production rates.

Uyuni-24 well

The gas production rates managed for Uyuni-24 well had to be lower than the implemented in previous wells. Appendix G shows the comparison between a production rate of 100,000 sm3/d and 35,000 sm3/d, obtaining higher gas outflow through well with the lower rate. The permeability of the surrounding grid cell for this well is 14 mD, almost ten times lower than Uyuni-03 and Uyuni-05, which is limiting the well to produce at higher flow rates.

Figure 32 shows a drainage radius of approximately 1.5 km, with a restricted flow pattern from north to south. The location of Uyuni-24 in the left wing of the alluvial ridge of the channel with OSL sample 6a (Figure 12) predetermined higher water saturation and pressure depletion at the northeast of the reservoir, including the adjacent channel belt with OSL sample 5d (Figure 12). The streamlines in Figure 33 shows fluid communication between both channel belts, due to the proximity of both fluvial bodies in the area.

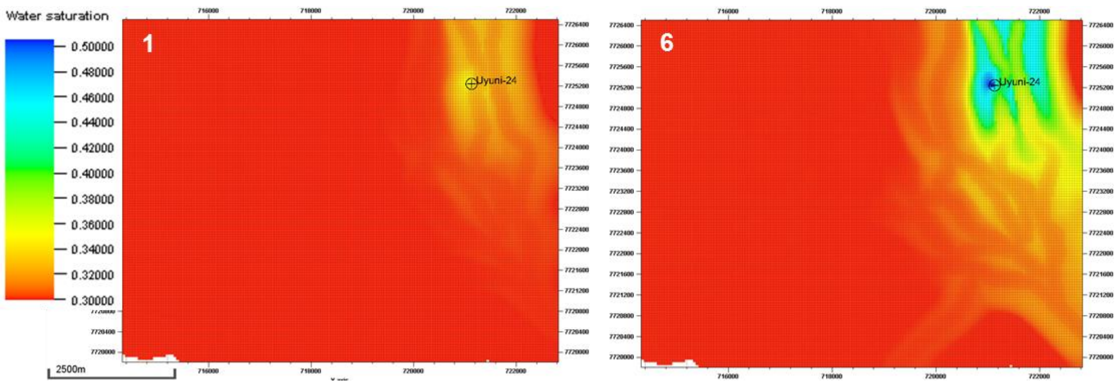

Figure 32 Water saturation maps comparing the first (left) and last year (right) of production in Uyuni-24

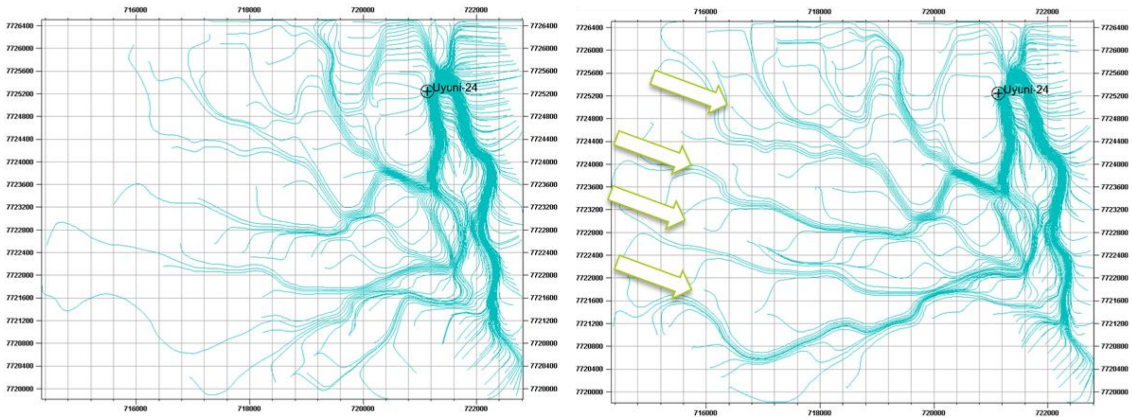

Figure 33. Streamlines map of the production of Uyuni-24. The fluid flow pattern is illustrated from the first sixth months (left) until the sixth year (right) of production.

The production chart of Uyuni-24 (Figure 34) is describing a constant gas production rate, with a gentle pressure depletion that allowed having a cumulative production of approximately $81\ x\ 10^{6} sm^{3}/d$ay (Appendix G) and a recovery factor of 6%. It is significantly less than the previous two wells; but, considering the lower permeability of the surrounding grid cell, it is a good location for a well to be placed in. Again the water production is insignificant and then, neglected.

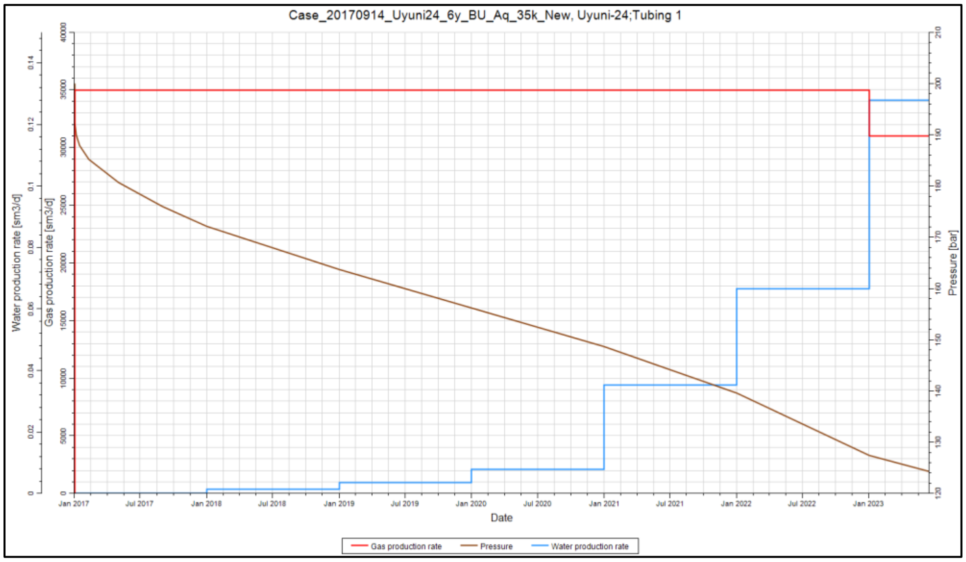

Figure 34. Uyuni-24 well production chart for 35,000 sm3/d

Uyuni-15 well

This well was located between the right wing of the alluvial ridge from the river with OSL samples 4b and at the left side of the river with OSL samples 2a, 2b and 2c. This grid cell has a permeability of 0.98 mD and most of the fluid flow is occurring between these two channels (Figure 35). As it was expected, the streamlines in Figure 36 shows that the flow in the alluvial ridges does not occur parallel to the channel belt, but through the nearest channel to the producer well. Other channels seemed to contribute to the fluid flow (greenish arrows - Figure 36); however, the intensity is very weak, and the contribution is not relevant for the drainage radius, estimated in 100 meters (Appendix I4. Uyuni-15 well).

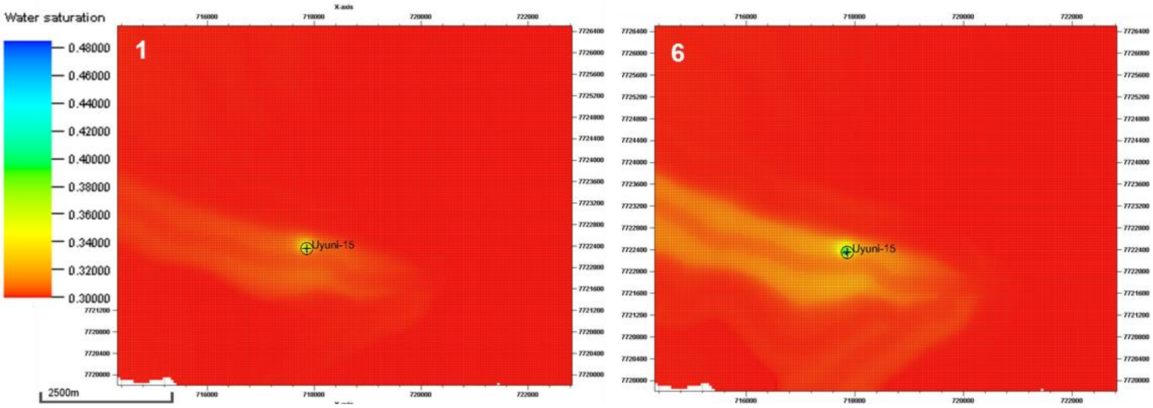

Figure 35. Water saturation maps comparing the first (left) and last year (right) of production in Uyuni-15

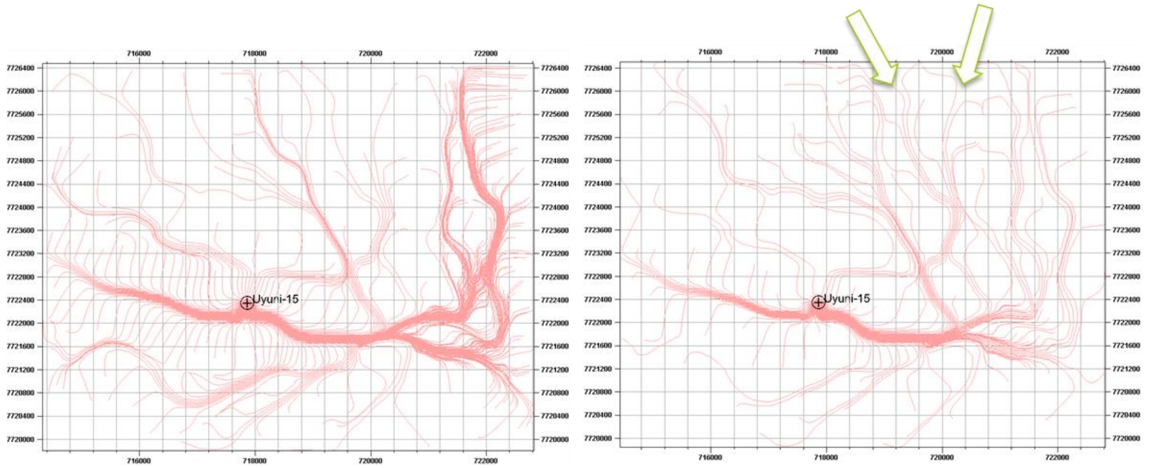

Figure 36. Streamlines map of the production of Uyuni-15. The fluid flow pattern is illustrated from the first sixth months (left) until the sixth year (right) of production

Figure 37 shows the production behaviour with 6500 sm3/d. During the first six months of production, fast pressure depletion occurs. However, due to the proximity to the aquifer at the west side of the fluvial fan (Figure 35), the pressure starts increasing again, reducing the fluid depletion and stabilising it in around 3000 sm3/d.

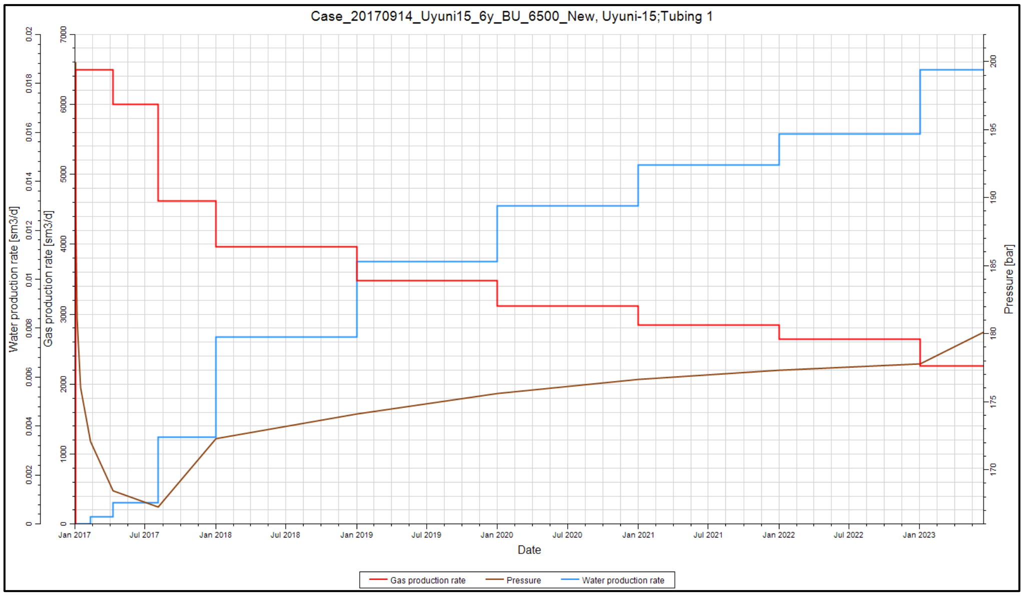

Figure 37. Uyuni-15 well production chart at 6,500 sm3/d

Uyuni-11 well

The location of this well was planned between the rivers with OSL samples 2a, 2b, 2c and 3a,3b,3c; representing floodplain sediments with a permeability of 0.08 mD. Unlike the previous wells (where the streamlines showed that the fluid flow was “looking for” higher permeability paths), the streamlines are showing a radial flow (Figure 39). Mostly, from the proximities of the well (alluvial ridges from the vicinities of the channels bordering the area), and some influx from the channels at the northeast of the fluvial fan. However, the water saturation (Figure 38) and pressure maps (Appendix I5. Uyuni-11 well) reflect the subtle changes in the reservoir; the flow rate is very low, and the outflow through well is insignificant, resulting in a drainage radius of approximately 70 m.

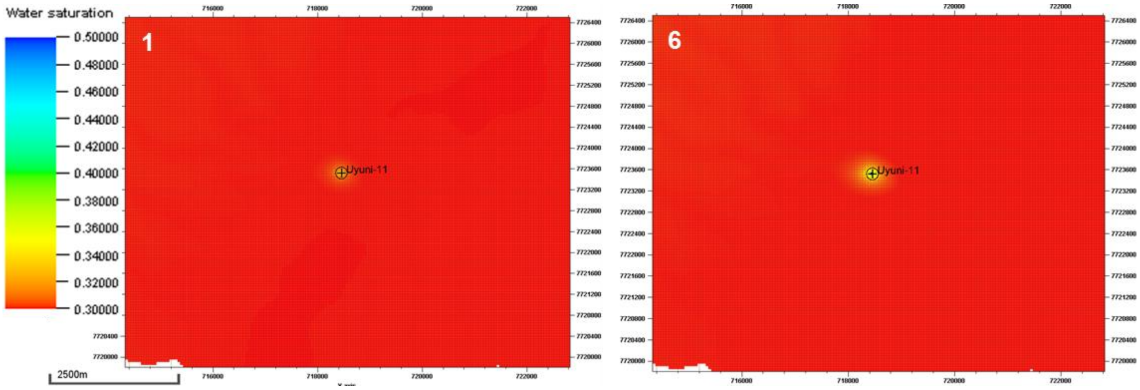

Figure 38. Water saturation maps comparing the first (left) and last year (right) of production in Uyuni-11

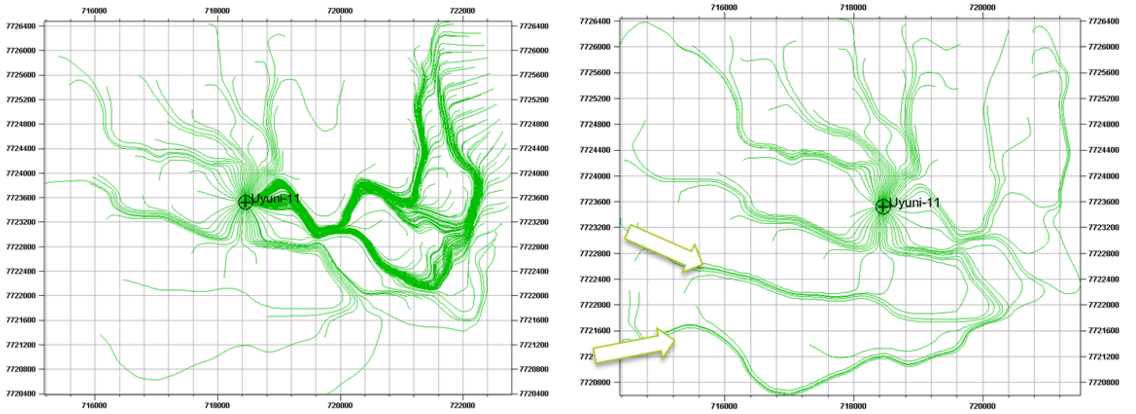

Figure 39. Streamlines map of the production of Uyuni-11. The fluid flow pattern is illustrated from the first sixth months (left) until the sixth year (right) of production

The low permeability and the low difference between the reservoir pressure and the tubing head pressure allow maintaining a low but constant flow rate. The production chart of the well (Figure 40) showed a smooth pressure decline, increasing at the beginning of the sixth year due to the influence of the bottom water drive.

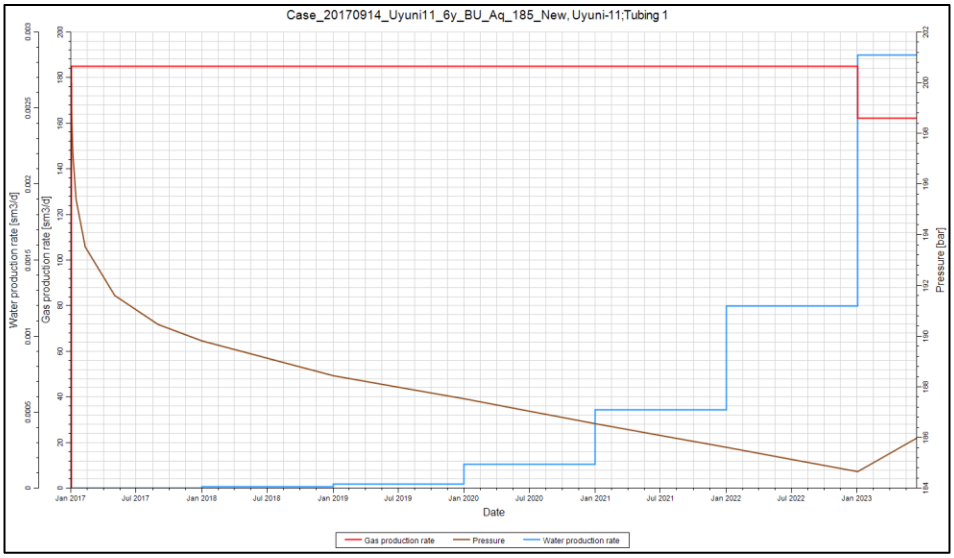

Figure 40. Uyuni-11 well production chart for 185 sm3/d

Uyuni-22 well

The last evaluation of the reservoir was considering a well located at the border of the fluvial fan, far from the bottom water drive and representing the floodplain sediments. With a permeability of 0.04 mD, the well is unable to produce more than 10 sm3/d (Figure 43) and it is barely affected by the bottom water drive at the end of the production life; reflected in weak streamlines (arrows in Figure 42) and with a drainage radius of 20 m (Figure 41).

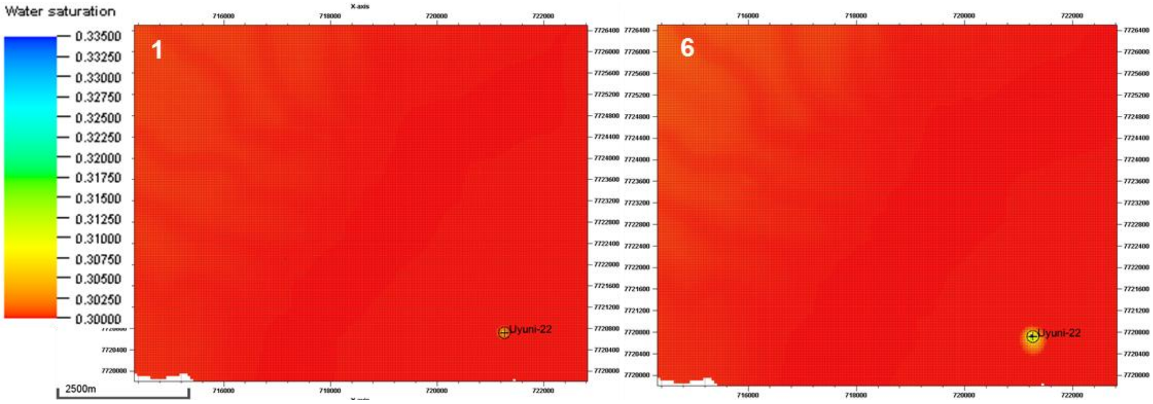

Figure 41. Water saturation maps comparing the first and last year of production in Uyuni-22

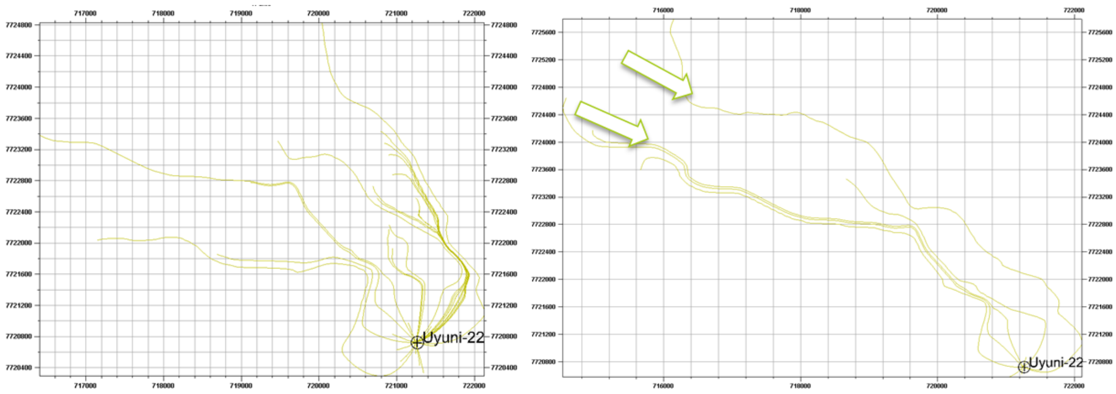

Figure 42. Streamlines map of the production of Uyuni-22. The fluid flow pattern is illustrated from the first sixth months (left) until the sixth year (right) of production

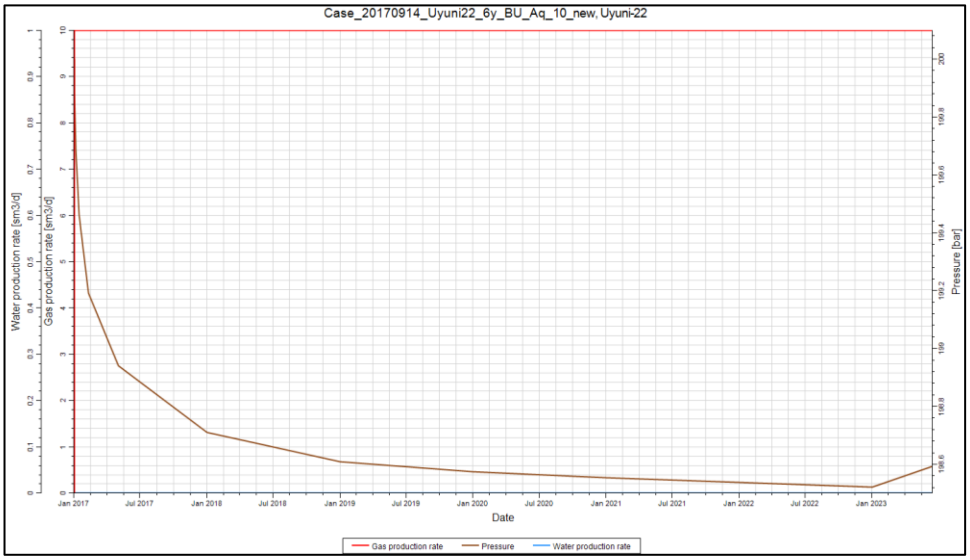

Figure 43. Uyuni-22 well production chart for 10 sm3/d

4.5.2.6 Cumulative area vs Efficiency in production rates

Once the static and dynamic model was constructed, it was important to calculate an anticipated value for the given production. In statistics, the expected production rate that could be found at any point of the fluvial fan system can be calculated by multiplying each of the most efficient production rate per facies by the possibility that each outcome will occur (in this study, the area percentage calculated per facies). Then, summing all of those values (Table 7).

$$E[x] = \sum_{i=1}^{n} A_i \times q_i$$

$$E[x] = (0.085 \times 10) + (0.348 \times 185) + (0.386 \times 35000) + (0.18 \times 300000)$$

$$E[x] = 67575\ sm^3/day$$

However, the variation among the measurements is high, with a standard deviation of

$$\sigma = \sqrt{\frac{\sum_i (E_{(x)i} - \bar{E}_{(x)})^2}{N-1}} = 25540$$

Table 7: Area percentage per facies and their permeability ranges, considered for the calculation of the Expected value of production rate.

Permeability Ranges [mD]	Area [%]	Area [Fraction]	Facies	Efficient Rate per Facie [sm3/day]	E(x)
0 - 0.019	8.5	0.085	Floodplain (Clay)	10	0.85
0.06 - 0.6	34.8	0.348	Floodplain (Fines)	185	64.38
0.6 - 35	38.6	0.386	Crevasse splay deposits	35000	13510
35 - 154	18	0.18	channel belt	300000	54000
		0.999		**Expected value:**	**67575**

The Expected Value was important to calculate because it allowed predicting the most likely production rate according to the property distribution; in this case, using permeability histogram from the model (Appendix K). Besides, the most effective production rates were plotted against the cumulative area (from all the facies in the fluvial system) to have the whole uncertainty of the model (Figure 44).

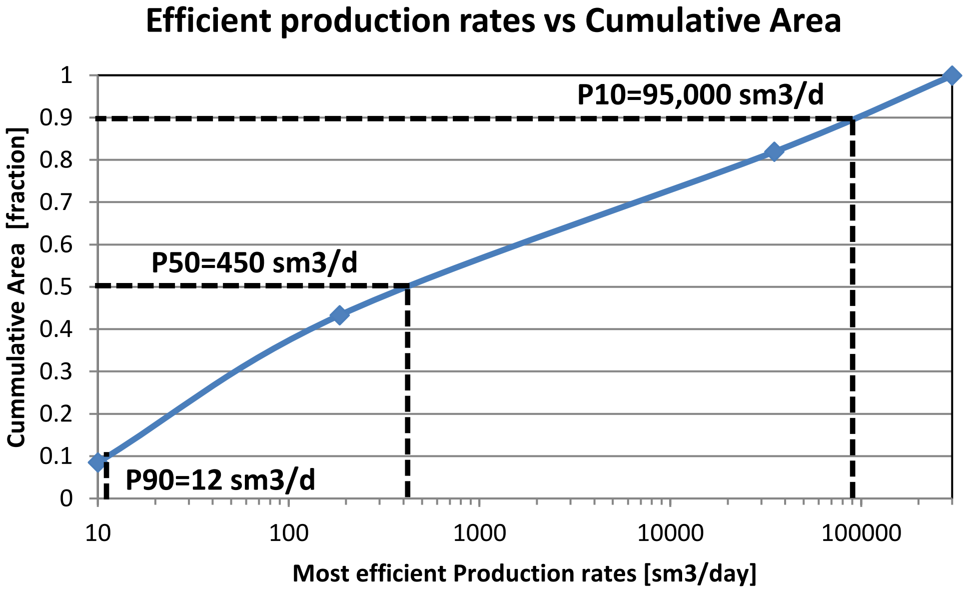

Figure 44. Cumulative distribution function with P10, P50, and P90

5. Discussion

5.1 Differential GPS data

5.1.1 Gradient profile

Observing the longitudinal cross-section in Figure 11B, the lacustrine deposits slope decreasing with an order of magnitude could explain the thicker succession of fluvial sediments in the middle regional transect compared to the proximal, caused by a further decrease in flow energy. However, from middle to the distal section, the thickness of fluvial sediments is thinner again. It could be explained by the fact that the width of the fan is larger at the distal lobe of the system and the confinement pattern - observed in the middle and proximal section - is lower, spreading the sediments laterally, and thins out in areas where the progradation has not reached yet.

5.1.2 Detailed area

It was more difficult to recognise the avulsion of older channels at the apex of the fluvial fan system. It is explained by the fact that construction of alluvial ridges (by aggradation of levees, channel floor and crevasse splays) - followed by river avulsions shifting to a lower elevation – have overprinted the upstream sediments of the fluvial fan. It can be related to the study from (Rannie, 1990), who compared super-elevation versus local channel flow depth from the Assiniboine River, Manitoba, Canada. Around 65% of the bankfull channel is elevated over the adjacent floodplain, demonstrating that most of the channels had changed their position before the base of the confined channel became equal in height to the floodplain. Other authors have proposed depositional mechanisms to describe the expression of the stacking pattern of the fluvial low-gradient dryland river systems, suggesting that the process of channel-belt-super-elevation is reproduced until an upstream avulsion take place again (Van Toorenenburg, et al., 2016).

The aggradation of floodplain and the stacking pattern due to the successive river avulsion through the last 4000 years is not homogeneous throughout the entire area. The development of the fluvial sediments has changed from southwest to northeast, having an asymmetrical shape of the channel in a cross-section, with thicker successions from the central part of the fan to the north-northeast. During the first stages of the river (4.60 – 3.60 ka), the active channel was preserved in the central part of the fluvial fan. Then, the subsequent channel paths developed a compensational stacking pattern, building-up a positive topography. This processes created a barrier for the location of the next river avulsions, avoiding the central area. It is observed in Figure 16 that the next avulsion of the river with samples 3 (3.60 – 2.35 ka) occurred on the northeast side of the oldest river (4.60 – 3.60 ka), having the younger river a positive relief of 4 cm higher respect to the previous one (E-E'). If we compare the highest topography level of the oldest river and the present-day river, the difference goes up to 52 cm.

The asymmetrical development of the fluvial fan – prone to a higher amalgamation of successive avulsed channel belts to the central and northeast part of the system – permit the development of complete alluvial ridges in certain parts of the river path. The A-P' profile in Figure 16 and the distal profile in Figure 17 illustrate outstanding channel wings, developed for each of the river groups.

The characterisation and subdivision of alluvial ridges were possible by the combination of dGPS data, OSL absolute dating samples, and Google Earth Imagery techniques. The schematic representation of the floodplain stacking pattern in Figure 13 showed the recorded dGPS data on the surface (yellow line) and what kind of information can be missed. For instance, the extension of the complete alluvial ridge and where to define the edges of each “wing” when two or more ridges are in contact. Also, the southern section of profile D-D’ serves as an example of how important is to combine these technologies. The southwest wing of the alluvial ridge in the river with sample 5e (profile D-D’) seemed to continue to the left of the section. However, zooming in the area where the aggradation of river 5e occurred on top of river 4c (Figure 45), it is clear that the first 200 meters of the profile D-D’ from south to north (left to right in the profile) is part of the river with sample 4c.

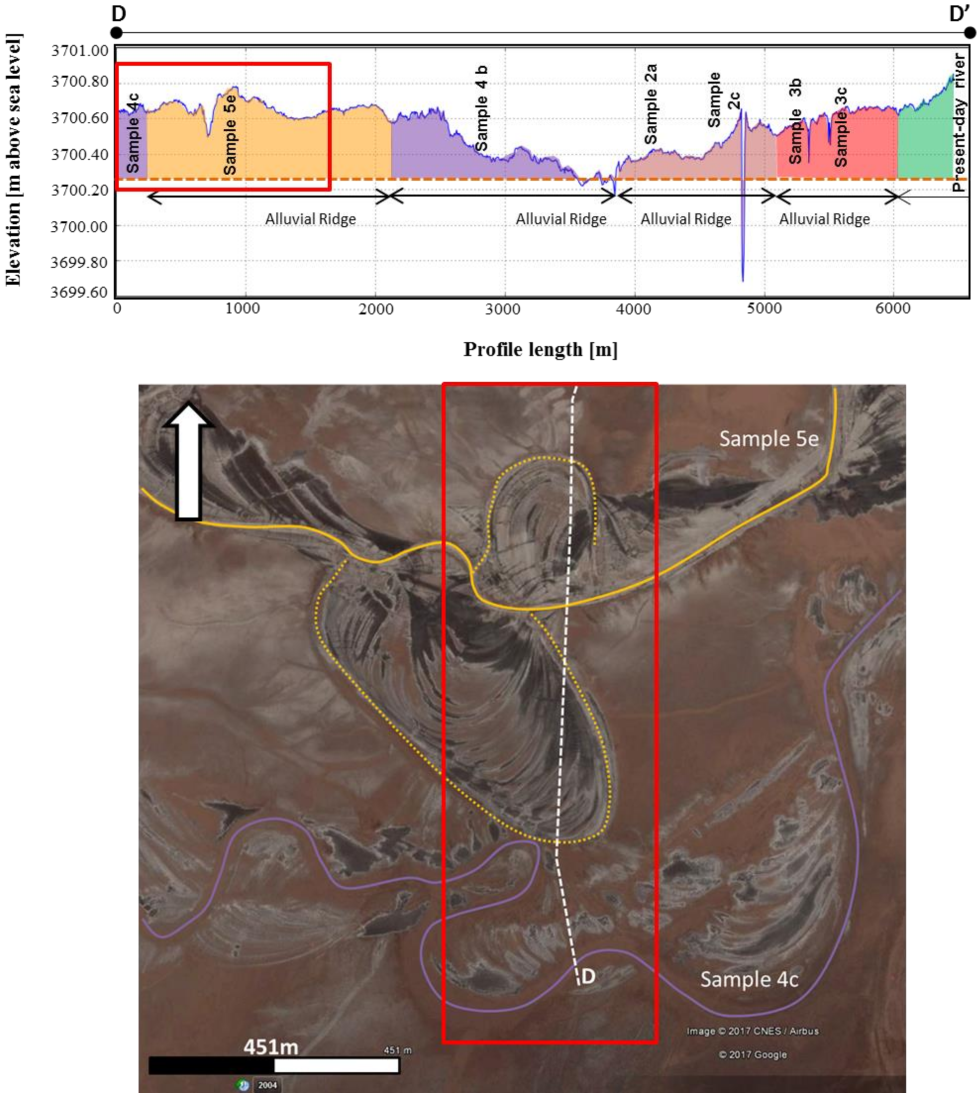

Figure 45. Detailed section of the first 1.2 km of D-D’ transect.

5.1.3 Regional area

The dGPS data obtained in the regional sections and the Google Earth Imagery Pro elevation profile were used to measure the lowest height in the transects and to determine the lacustrine deposits to be defined as the bottom layer in the geological model (Figure 17). However, based on the sedimentary logs obtained in the field, the thickness of the fluvial deposits can be higher - reaching up to 2.80 m before finding the contact between the fluvial and the lacustrine sediments - as described in the lithology log 2011-S10 (Appendix D). These thicker sections can be developed when incisional rivers eroded the basal layer. Nevertheless, this gross section was the only complete measurement in the area, due to the difficulty of removing the fluvial sediments to reach the contact between the fluvial and lacustrine deposits in several locations in the field.

Another uncertainty would be how constant is the 2.80 m of depth found in the sedimentary log 2011-S10 (Appendix D) along the entire area (magenta line in Figure 46). It was not possible to obtain the geometry of the contact between the fluvial and the lacustrine deposits like the imaginary line sketched in Figure 46 (brown dotted line). Because of that, the demarked depths in Figure 17 and Figure 46 (red dashed lines) found in the dGPS data have been defined as the lacustrine deposits.

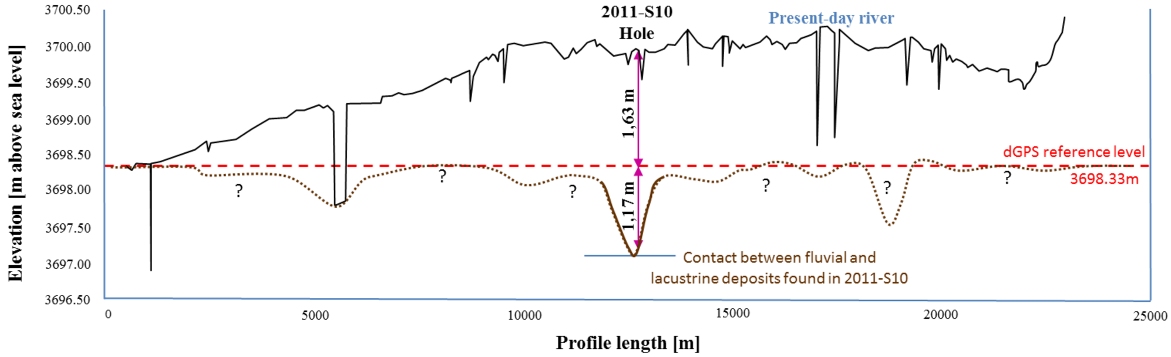

Figure 46. Sketch of the medial profile, comparing the reference level measured with dGPS and the contact between fluvial and lacustrine deposits found in 2011-S10 hole. The brown line is showing the uncertainty in the surface geometry of the lacustrine deposits.

The thinnest sections of the fluvial fan system are found in the distal area, where the sediments are less confined, spreading widely until reaching the salt lake at the northwest of the system. This can be justified by the absence of sediment supply. The lacks of sufficient and continuous fluvial streams to reach the farthest areas have thinned out these sediments. This is an important observation for the random location of the wells as secondary targets, which will avoid the thinnest areas for the gas production.

5.2 Reservoir Geology

5.2.1 Regional top and bottom layers

From proximal to medial transects, the dGPS data density was enough to characterise the channels and differentiate each of the alluvial ridges. On the other hand, the topography information in the area between medial to distal transects is biased to the northern part, (considering the dGPS data recorded in 2014) raising the topography in just a small area (Figure 47– red ellipse). However, this elevation is not symmetric along the whole fan-shape, and it is unrealistic. It is suggesting progradation and aggradation of the river only in the central region, without any development activity at the edges of the system, something that it is not true. However, the shape of the topography map is not affecting the volumetric calculation of the gas initially in place, because the dynamic model was concentrated in the southeast of the system.

The bottom layer of the model was built considering the lowest heights in the regional transects, assuming this levels as the lacustrine deposits underlying the oldest floodplain sediments of the fluvial system. However, the depth where the contact between the fluvial and the lacustrine layer was found with percussion drilling was up to 2.80 m, much thicker than the maximum thickness of 2 m found in the model. In reality, the lacustrine layer must be an irregular surface, perhaps containing incisions from the development of the first fluvial activity (Figure 46). Nevertheless, with the available information, it is only possible to assume a continuous flat floor. Therefore, the current gas volume calculated in the static model was interpreted as the most conservative amount of hydrocarbons in the system.

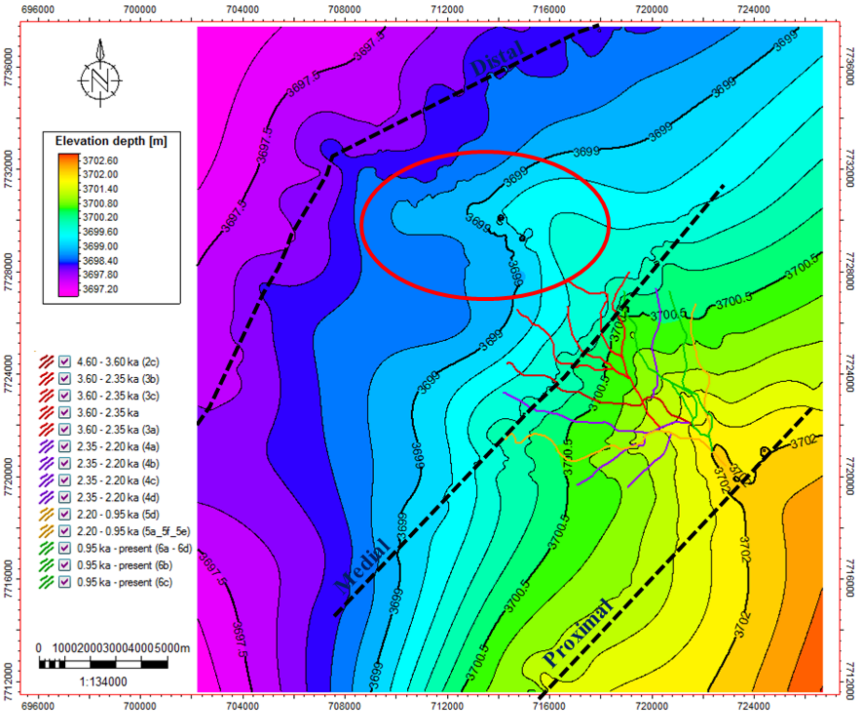

Figure 47. The top layer of the model with the high density of dGPS data in the proximal transect of the fluvial fan and the restricted data in the distal section (red ellipse).

5.2.2 Detailed region

The contours of the topographic map in Figure 20 are describing the depressions of the channel in the surface. However, the centre of the channel belts was considered as the representation of the rivers in the model and not the sinuous-meandering shapes in the real analogue, to avoid unrealistic distribution of the petrophysical parameters in the alluvial ridges; one of the problems found during the process of populating properties.

5.2.3 Petrophysical properties

The narrowest channel belt with 320 m of width (sketched in Figure 9B) , was used to generalise the rest of the channel belts in the Río Colorado system. This assumption was made to observe disconnected channels in zones far from the apex of the divergent flow pattern. Otherwise, the fluvial system would have shown higher connectivity with the width average of the channel belts (561 m). Ideally, the model should have been run taking the width of each channel belt. However, the distribution of the properties was not possible to run consecutively with the current method of *property modelling – distance to object*. Having said that, each channel was appended to the next one. In the end, all combined were run to populate the property as a unique object.

5.2.4. Fluid model

Most of the values run in the fluid model have been taken from the preset values from Petrel. These values inside the software are just a reference and represent a common average of reservoir conditions (in this study: *dry gas).* One of the recommendations provided by the Schlumberger Customer Care Centre was that if the fluid model is simulated for a particular reservoir, it is important to make sure that the minimum and maximum pressure (in the *make fluid process tab*) cover all operating ranges of pressures during the lifetime of the reservoir. In this study, that rule was achieved because the lower reservoir pressure for every single simulation never went below the minimum pressure of 80 bar.

5.2.5 Simulation cases

The gas production rate was the main criteria to select the optimal simulation case scenario for each well in this study. Each of the flow rates defined in Table 6 was the base to describe the changes in water saturation, pressure depletion, and streamlines. However, this study does not include an economic evaluation that could involve other vital factors; for instance, the cost of kW per m^3produced. In that case, the priority for the selection of the best gas rate could be different. Taking the Uyuni-05 well as an example, the gas production rate of 50,000 sm3/d would have been a better option, considering that is six times lower than the suggested rate in the current study and it could produce almost half of the hydrocarbon that the rate of 300,000 sm3/d has produced (Appendix G).

Observing the production chart of Uyuni-05 well (Figure 28), the high flow rate provides a lot of gas production, specifically during the first 1.5 years of production. Then, the outflow reached a stable flow rate for the next 4.5 years, ending in approximately 50,000 sm3/d. The water production does not seem to be a problem in this simulation, but other obstacles can complicate the life of a well with such a high initial production rates; for example, sand production or wellbore storage. The scope of this study did not reach the analysis of these possible problems, but in real life, these factors must be measured and considered.

The analysis of the production behaviour in the wells has allowed identifying which components have a higher impact in the well management. For example, high permeability does not always guarantee higher production rates. Uyuni-03 is located in a place with 116 mD, compared with Uyuni-05 that has 101 mD, and its outflow through well is significantly lower (30% lower - Appendix G). The distance between each well is 1.9 km, with Uyuni-05 closer to the bottom water drive and surrounded by more channel belts. Also, Uyuni-03 is closer to the model edge; that means, the pressure is not received uniformly.

Based on the water saturation maps, it seemed that the drastic changes in the fluid saturation are concentrated at the early stages of the production, decreasing the effects of the depletion in areas far off the well location. However, observing pressure maps from the same wells in, the pressure depletion is still occurring. Therefore, it is important to consider these pressure changes when the reservoir is produced with more than one well, quantifying the interference and minimising the gas losses.

5.2.6 Fluid flow paths

The result of the simulation cases regarding water saturation, pressure and streamline maps, allowed to discuss and understand the communication between channel belts and alluvial ridges and how that connectivity is reflected in the resultant flow rates and recovery factors. The production behaviour is very different from well to well, but some characteristics are shared in all of them. For example, the simulations for Uyuni-05, Uyuni-11 and Uyuni-15 generated similar fluid flow input from the channel belts with OSL samples 5d and 6a (Appendix J). One possible explanation is that these channels are located next to the area where the amalgamation of several avulsed channel belts occurred (at the apex of the fluvial fan system by compensational stacking).

5.2.7 Cumulative distribution

The distribution of the permeability around the area and how much belongs to each of the facies were taking into account to calculate the uncertainty in the ranges of production rates that can be managed in the system. The range is high (from 12 to approximately 95,000 sm3/d) because the permeability is populated with an exponential function. Because of that, the expected value was calculated, giving a value of approximately 68,000 sm3/day with a standard deviation of 25500.

This expected value was calculated considering the most efficient production rates for the wells included within the simulation (Uyuni-05, Uyuni-03, Uyuni-24, Uyuni-15, Uyuni-11, and Uyuni-22). Each of these wells are located in different facies for the gas production. The northwest of the fluvial fan was not involved to avoid an early water breakthrough. However, the northwest part of the fluvial fan contains most of the floodplain sheets in the model, where the channel is less confined and can shift easier. Based on that, the expected value would have been very different if the area not covered in the analysis were also included.

6. Conclusions

The integration of dGPS data and Google Earth Pro Imagery with river avulsion analysis in previous studies ((Donselaar, et al., 2013) and (Donselaar, et al., 2017)) have improved the understanding of the river avulsion and sand-sheet extension of the semi-arid river system of the Río Colorado in Bolivia. The repeated river avulsions during the last 4000 years have created a connected network of amalgamated channel belts and alluvial ridges, mainly concentrated at the apex of the fluvial fan system and decreasing in thickness and connectivity towards the Salar de Uyuni.

Floodplain deposits and alluvial ridges are more evident to be recognised at the distal transect of the fluvial fan system, at the largest transect in the detailed section of the model (from A-A’ to P-P’) and at the edges of the fan, proximal to the avulsion point (H-H’). For the rest of the local transects, the alluvial ridges are laterally amalgamated and overlying older sediments, impeding the recognition of initial floodplain deposits.

The geomorphological and sedimentological characteristics of the fluvial river system, combined with the subsurface rock properties measured with borehole logs and plug samples from the PRW-01; allowed the construction of a three-dimensional model. The distribution of reservoir properties as function of alluvial ridge width permitted to analyse the production behaviour of six well depending on its location within the several facies interpreted in the model. Based on that, it was possible to predict the recovery factor and most likely production rate for each well included in the simulations.

The proximity of the rivers with OSL samples 5d and 6a to the apex of the fluvial fan system, where the amalgamated stacking pattern is higher, seems to serve as a fluid flow path for the contribution of the production area. Most of the streamlines created during the production of the wells described high fluid flow input from these channels, a factor to be considered if it is intended to produce that zone from a well located in that area.

The streamlines allowed observing the fluid flow pattern, representing the pressure throughout the entire reservoir and how it changes over time. However, it is difficult to quantify the contribution of each facies and assign a recovery factor for each one. Instead, it was better to relate the amount of gas production that each facies can handle with the probability to “hit” or to find the facies in the reservoir (based on the histogram of the permeability).

The estimates for connectivity of the channel belts and alluvial ridges in the dynamic model are very conservative because the average value for the width of the channel belts was considered taking into account the narrowest channel of the fluvial system (to have a higher contrast between alluvial ridges). Controlling the width of each channel at a time may increase the volume calculation of GIIP, and improving the expected production rates per facies.

The bottom water drive has an important role on the pressure and fluid distribution of the phases in the fluvial fan system. The pressure support coming from the lowest part of the reservoir helped to maintain a constant pressure at the latest stage of the production and, as observed in some of the production charts, the pressure even increased (not relevant contribution). The impact of the pressure effect will depend on the location of the well (how far is from the aquifer entrance) and the orientation of the channel.

Despite the lower petrophysical properties of the alluvial ridges and floodplain sediments compared to conventional coarse-grained fluvial reservoirs, their lateral amalgamated stacking pattern increases the connectivity and improves the hydrocarbon potential of these types of thin-bedded sand layers. Because of this, the production stages of mature oil fields can be extended, guaranteeing the role of gas as a driver of energy supply and its role in the energy transition.

7. Recommendations

To continue with the development of the static and dynamic model in the entire fluvial system (400 km^2), it would be important to collect more dGPS data at the west side of the region, to extrapolate the existent information recorded in 2014. These hypothetic new points will have to be correlated with a detailed interpretation of the satellite image to follow the fluvial paths for each of the channel belts from medial to distal transects. The present study considered less than half of the regional area, focused mainly in the region of higher frequency avulsions. Then, if new data is incorporated to the model by applying this approach, the top layer of the model will be higher. Consequently, the bulk rock volume of the model will be higher, improving the GIIP volume calculation and allowing to produce the reservoir with higher production rates.

The width of the channel belts was generalized in the model taking into account the narrowest channel present on the semi-arid river system, underestimating the volume calculation, represented in lower reserves and impacting the economic evaluation of the project (not developed in this study). Therefore, it is essential to model one channel at a time, allowing to control the width of each. Perhaps, detailed facies recognition can be done using ERDAS satellite image analysis, helping to represent the exact dimension of each facies and improving the characterisation of the reservoir.

The dynamic model can be more accurate regarding subsurface reservoir conditions. The fluid model, rock physics functions, and type water drive were built based on the preset values that Petrel software has to offer and only represent a reference for the common average of the reservoir conditions. However, the results have shown the reservoir potential of the thin-sand sheet deposits, providing an excellent analogue for the reservoirs in the Netherlands. Therefore, the project can be continued focus in the latest stage of this study.

Bibliography

Aitken, M., 1998. *An Introduction to Optical Dating. The Dating of Quaternary Sediments by the Used of Photon-Stimulated Luminescence.* Oxford, New York, Tokyo: Oxford Science Publications. Clarendon Press.

Argollo, J. & Mourguiart, P., 2000. Late Quaternary climate history of the Bolivian Altiplano. *Quaternary International,* Volume 72, pp. 37-51.

Baker, P. A. et al., 2001. Tropical climate changes at millennial and orbital timescales on the Bolivian Altiplano. *Nature,* Volume 409, pp. 1-4.

Bills, B. G., de Silva, S. L., Currey, D. R. & Emenger, R. S., 1994. Hydro-isostatic deflection and tectonic tilting in the central Andes: Initial results of a GPS survey of Lake Minchin shorelines. *Geophysical Research Letters,* 21(4), pp. 293-296.

Bisdom, K., 2016. *Petrel 2014 guide. For courses AES1510 (Geological Interpretation of Seismic data) and AES2009 (Field Development Project),* Delft: TU Delft.

Boerboom, H., 2016. *Detectability and modeling of low net-to-gross fluvial stratigraphy,* Delft: TU Delft.

Bonté, D., van Wees, J. & Verweij, J., 2012. Subsurface temperature of the onshore Netherlands: new temperature dataset and modelling. *Netherlands Journal of Geosciences - Geologie en Mijnbouw,* 91(4), pp. 491-515.

Bouman, L., 2014. *Spatial distribution and connectivity of thin-bedded crevasse splay sandstones; outcrop analogue studies for tough gas reservoir potential,* Delft: TU Delft.

DeCelles, P. & Horton, B., 2003. Early to middle Tertiary foreland basin development and the history of Andean crustal shortening in Bolivia. *Geological Society of American Bulletin,* Volume 115, pp. 58-77.

Donselaar, M., Cuevas Gozalo, M. & Moyano, S., 2013. Avulsion processes at the terminus of low-gradient semi-arid fluvial systems: Lessons from the Río Colorado, Altiplano endorheic basin, Bolivia. *Sedimentary Geology,* Volume 283, pp. 1-14.

Donselaar, M., Cuevas Gozalo, M. & Wallinga, J., 2017. *Avulsion history of a Holocene semi-arid river system - outcrop analogue for thin-bedded fluvial reservoirs in the Rotliegend feather edge.* Paris, France, Proceedings 79th EAGE Conference & Exhibition. Paper Th C105, 5 pp. DOI: 10.3997/2214-4609.201700610.

Geluk, M. v. D. T., 1996. Development of the Permo-Triassic succession in the basin fringe area, southern Netherlands. In: B. D. N. W. Rondeel H.E., ed. *Geology of Gas and Oil under the Netherlands.* Dordrecht: Springer, pp. 57-78.

Hammerschmidt, K., Dobel, R. & Friedrichsen, H., 1992. Implication of 40Ar/39Ar dating of early Tertiary volcanic rocks from the north-Chilean Precordillera. *Tectonophysics, v.202,* pp. 55-81.

Hampton, B. & Horton, B., 2007. Sheetflow fluvial processes in a rapidly subsiding basin, Altiplano plateau, Bolivia. *International Association of Sedimentologists, Sedimentology, 54,* pp. 1121-1147.

Horton, B. K., Hampton, B. A. & Waanders, G., 2001. Paleogene synorogenic sedimentation in the Altiplano plateau and implications for initial mountain building in the central Andes. *Geological Society of American Bulletin,* 113(11), pp. 1387-1400.

Isacks, B. L., 1988. Uplift of the Central Andean Plateau and Bending of the Bolivian Orocline. *Journal of Geophysical Research, Vol. 93,* pp. 3211-3231.

Lavenu, A., 1991. *Lago Titicaca, Síntesis del conocimiento limnológico actual.* ORSTOM, Institut Francais de Recherche Scientifique pour le Développement en Cooperation. ed. La Paz, Bolivia: Claude Dejoux y André Iltis.

Lenters, J. & Cook, K., 1997. On the origin of the Bolivian High and related circulation features of the South American climate. *Journal of Atmospheric Science,* Volume 54, pp. 656-677.

Mackey, S. & Bridge, J., 1995. Three-dimensional model of alluvial stratigraphy: Theory and application. *Journal of Sedimentary Research,* Volume 65, pp. 7-31.

Mohrig, D., Heller, P., Paola, C. & Lyons, W., 2000. Interpreting avulsion process from ancient alluvial sequences: Guadalope-Matarranya system (northern Spain) and Wasatch Formation (western Colorado). *Geological Society of American Bulletin,* 112(12), pp. 1787-1803.

Murray, B., Horton, B., Matos, R. & Heizler, M., 2010. Oligocene-Miocene basin evolution in the northern Altiplano, Bolivia: Implications for evolution of the central Andean backthrust belt and high plateau. *Geological Society of America Bulletin,* 122(9/10), pp. 1443-1462.

Nichols, G., 2009. *Sedimentology and Stratigraphy.* 2nd ed. Chichester: John Wiley & Sons Ltd.

Noordijk, N., 2014. *Geological characterisation of thin-bedded crevasse splay sandstones; outcrop-analogue studies for tough gas reservoir potential,* Delft: TU Delft.

Placzek, C. J., Quade, J. & Patchett, J. P., 2011. Isotopic tracers of paleohydrologic change in large lakes of the Bolivian Altiplano. *Quaternary Research,* Volume 75, pp. 231-244.

Placzek, C. & Patchett, P. J., 2006. Geochronology and stratigraphy of late Pleistocene lake cycles on the southern Bolivian Altiplano: Implications for causes of tropical climate change. *Geological Society of America Bulletin,* 118(5/6), pp. 515-532.

Placzek, C., Quade, J. & Patchett, P., 2013. A 130 ka reconstruction of rainfall on the Bolivian Altiplano. *Earth and Planetary Science Letters,* Volume 363, pp. 97-108.

Rannie, W., 1990. The Portage La Prairie Floodplain Fan. In: J. W. a. Sons, ed. *Alluvial Fans: a field approach.* s.l.:s.n., pp. 179-193.

Rhodes, E. J., 2011. Optically Stimulated Luminescence Dating of Sediments over the Past 200,000 Years. *Annual Review of Earth and Planetary Sciences,* 39(0084-6597/11/0530-0461), pp. 461-488.

Rigsby, C. A. et al., 2005. Late Quaternary palaeolakes, rivers, and wetlands on the Bolivian Altiplano and their palaeoclimatic implications. *Journal of Quaternary Science,* 20(7-8), pp. 671-691.

Rodríguez, A., 1985. *Las Cuencas Intramontanas Andinas.* Bogotá, Colombia, 11 Simposio Bolivariano. .

SCM, 2014. *Petrel TIPS&TRICKS from SCM.* [Online] Available at: www.scminc.com/resources/SCM_Algorithm_Comparison_Petrel_2013.pdf [Accessed 15 August 2017].

Slingerland, R. & Smith, N., 2004. River avulsions and their deposits. *Annual Review of Earth and Planetary Science,* Volume 32, pp. 257-285.

Torres Carranza, Y. A., 2013. *Statig Reservoir Model of Crevasse Splays in the Colorado River System, Salar de Uyuni, Bolivia,* Delft: AES/TG/13-16.

Van Toorenenburg, K., Donselaar, M., Noordijk, N. & Weltje, G., 2016. On the origin of crevasse-splay amalgamation in the Huesca fluvial fan (Ebron Basin, Spain): implications of connectivity in low net-to-gross fluvial deposits. *Sedimentary Geology,* Volume 343, pp. 156-164.

Van Toorenenburg, K., Donselaar, M. & Weltje, G., 2016b. *Stacked crevasse splays in the semi-arid Huesca fluvial fan (Ebron Basin, Spain): implications for connectivity.* Catania, Italy, Proceedings 5th EAGE Shale Workshop. Paper Mo SWS P01, 5 pp. DOI: 10.3997/2014-4609.201600399.

Vuille, M. & Keimig, F., 2004. Interannual Variability of Summertime Convective Cloudiness and Precipitation in the Central Andes Derived from ISCCP-B3 Data. *Journal of Climate,* Volume 17, pp. 3334-3348.

Appendices

Appendix A

A general stratigraphic column of the Triassic in the West Netherlands Basin. The red rectangle is highlighting the wireline log information from the Rot Fringe and Solling formations. Modified from (Boerboom, 2016).

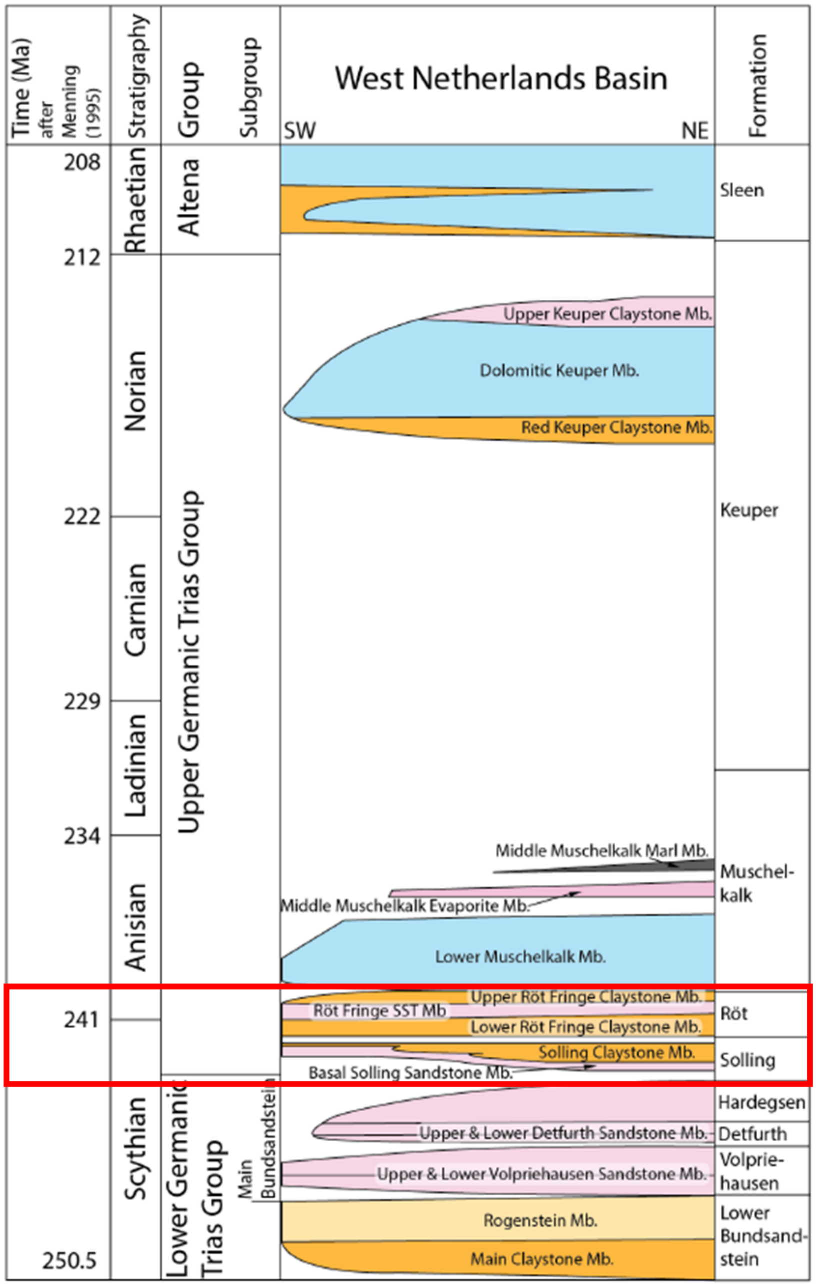

Appendix B

Excel spreadsheet is describing the schedule that was followed during the first stage of the fieldwork. It is shown the timing on/off of the base station and rover during the recording of GPS signals for the detailed transects (from A-A' to P-P') and the regional sections (proximal, medial and distal) of the fluvial fan system. Each of these transects is illustrated in Appendix C, including the direction in which the data was recorded.

NAME	DATE	SECTION	TIMING ON BASE STATION	TIMING ON ROVER	TIMING OFF ROVER	TIMING OFF BASE STATION
Detailed Transects	30-10-2016	A-A'	9:06:00	9:24:00	9:38:55	
		A'-C'		9:47:45	10:08:40	
		D'-D		10:25:45	10:46:40	
		E-E'		10:56:00	11:03:33	11:04:50
		E-E'	11:05:00	11:07:55	11:18:40	
		F'-F		11:22:50	11:38:10	
		G-G'		11:41:45	11:53:47	
		H'-H		11:58:30	12:05:30	
		I-I'		12:11:15	12:16:52	
		I-C		12:22:45	12:36:34	
		C-C'		12:38:28	12:48:40	
		B'-B		12:53:12	13:01:20	
		A-C		13:07:22	13:13:29	13:23:47
		P'-P	15:04:25	15:13:25	15:30:16	
		O-O'		15:38:48	15:50:27	
		N'-N		15:54:35	16:05:47	
		M-M'		16:25:10	16:29:26	
		L'-L		16:33:00	16:34:56	
		K'-K		16:47:48	16:51:19	
		J-J'		16:55:41	16:57:08	17:04:19
Middle Section	31-10-2016	Start - TurnWay1	10:36:30	10:57:53	11:24:10	11:32:50
		TurnWay1 - TurnWay2	11:49:15	11:56:55	12:11:55	12:20:15
		TurnWay2 - End	12:33:53	12:42:07	12:55:32	13:03:22
Distan Section	1-11-2016	Start - TurnWay1	9:32:15	10:00:54	10:14:36	10:22:05
		TurnWay1 - TurnWay2	10:35:22	10:42:28	10:59:00	11:07:16
		TurnWay2 - End	11:22:24	11:28:19	11:38:48	11:55:27
Proximal Section	1-11-2016	End - HalfWay	13:05:26	13:17:16	13:35:15	13:46:13
		HalfWay - Start	14:06:42	14:20:17	14:46:06	14:55:50
Repeated Middle Section	5-11-2016	-	10:29:30	10:45:31	11:06:51	11:08:14

Appendix C

The red square is enclosing the detailed transects traced from S-N, SW-NE, and W-E, covering an area limited by the national road (eastern dashed line) and the railway (western dashed line). It is the same image showed in Figure 7B.

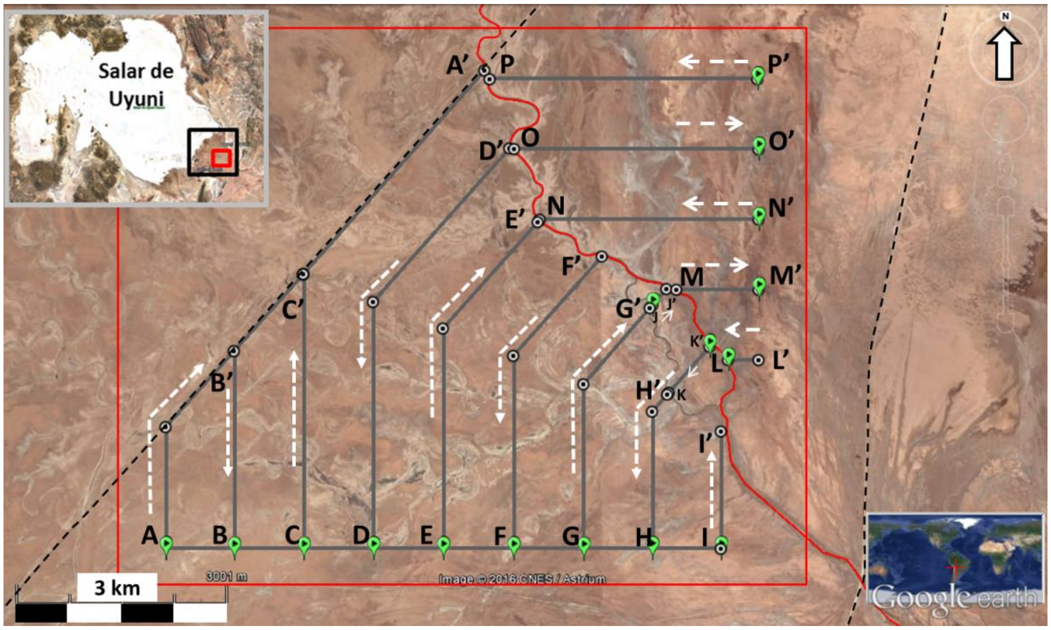

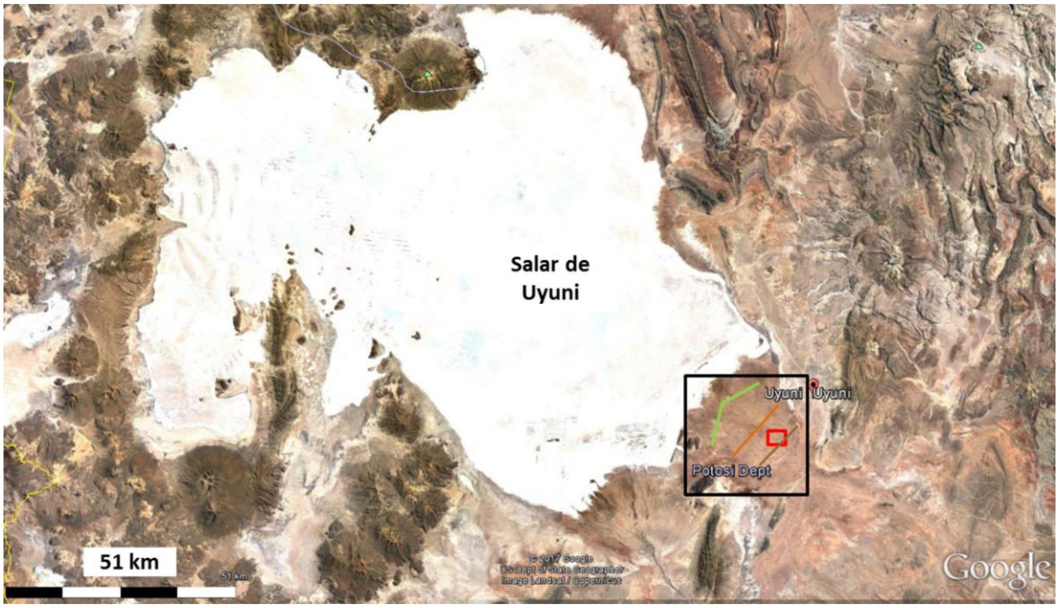

Appendix D

Lithology logs obtained in the field. Their location is specified in Figure 8

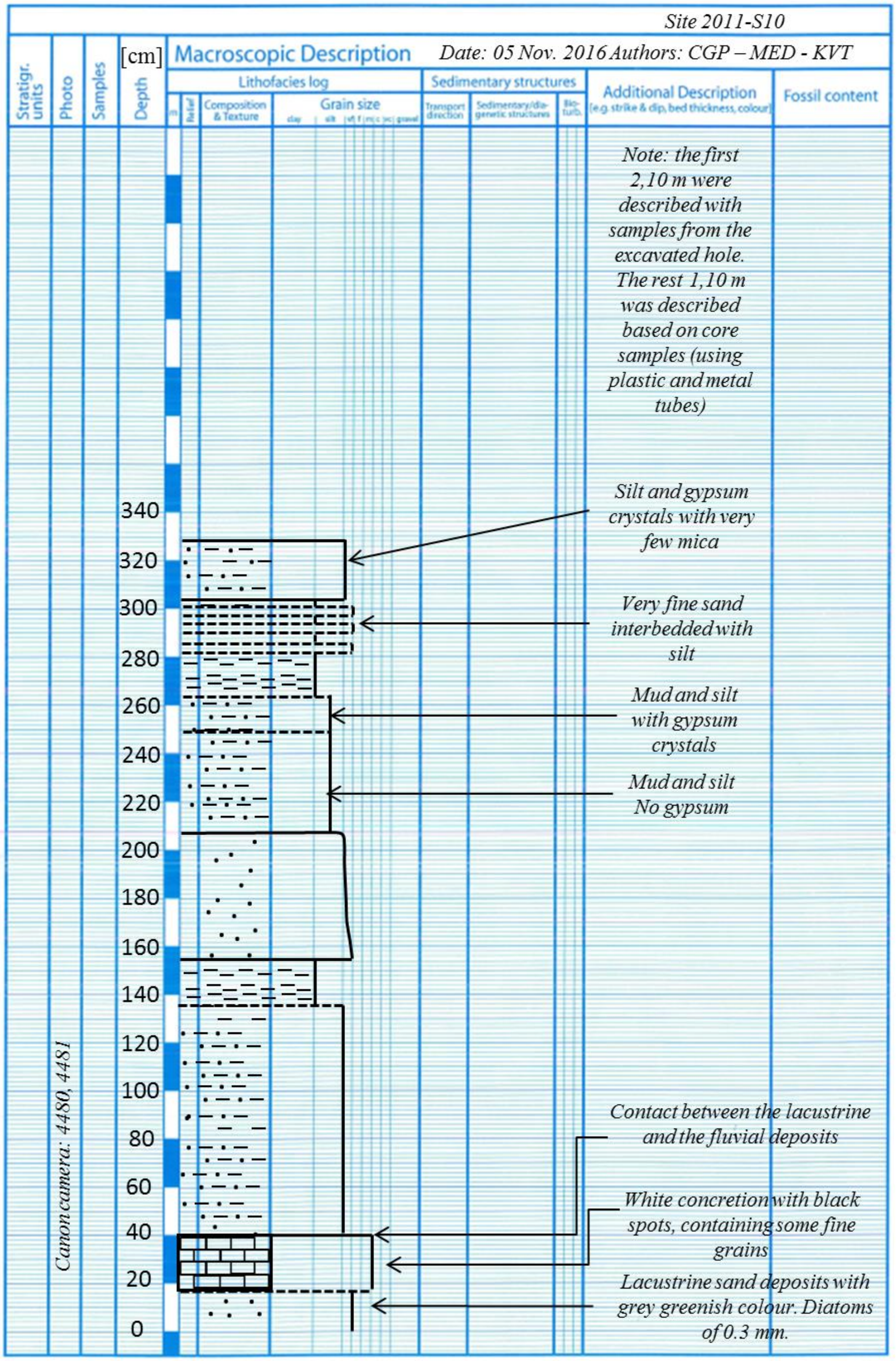

Site 2011-S10

Date: 05 Nov. 2016 Authors: CGP – MED - KVT

Note: the first 2,10 m were described with samples from the excavated hole. The rest 1,10 m was described based on core samples (using plastic and metal tubes)

Silt and gypsum crystals with very few mica

Very fine sand interbedded with silt

Mud and silt with gypsum crystals

Mud and silt No gypsum

Contact between the lacustrine and the fluvial deposits

White concretion with black spots, containing some fine grains

Lacustrine sand deposits with grey greenish colour. Diatoms of 0.3 mm.

Canon camera: 4480, 4481

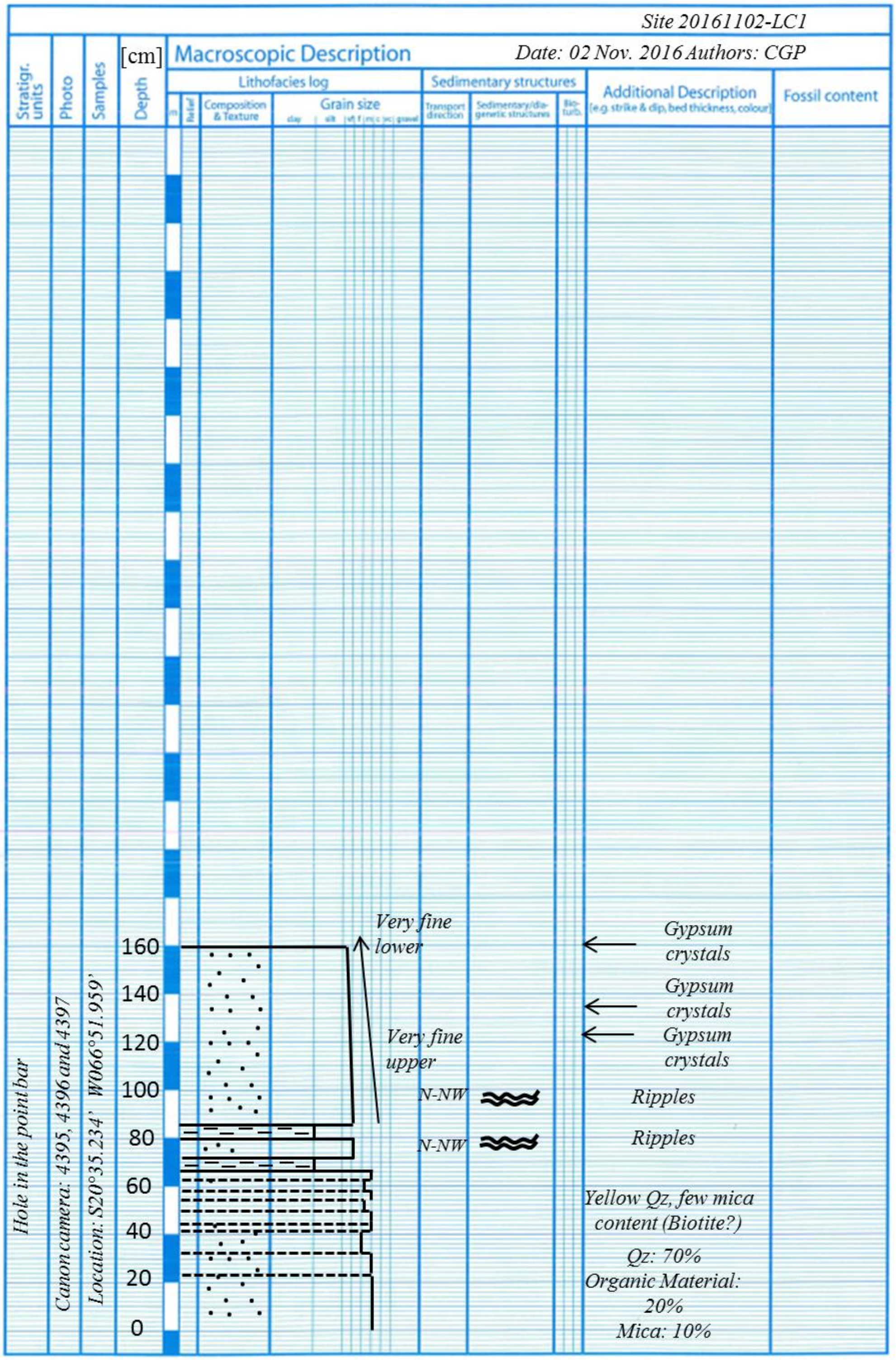
Site 20161102-LC1
Macroscopic Description
Date: 02 Nov. 2016 Authors: CGP
Stratigr. units
Photo
Samples
[cm]
Depth
Lithofacies log
Relief
Composition & Texture
Grain size
clay
silt
vf
f
m
c
vc
gravel
Sedimentary structures
Transport direction
Sedimentary/diagenetic structures
Bioturb.
Additional Description (e.g. strike & dip, bed thickness, colour)
Fossil content
Hole in the point bar
Canon camera: 4395, 4396 and 4397
Location: S20°35.234' W066°51.959'
160
140
120
100
80
60
40
20
0
Very fine lower
Very fine upper
N-NW
N-NW
Gypsum crystals
Gypsum crystals
Gypsum crystals
Ripples
Ripples
Yellow Qz, few mica content (Biotite?)
Qz: 70%
Organic Material: 20%
Mica: 10%

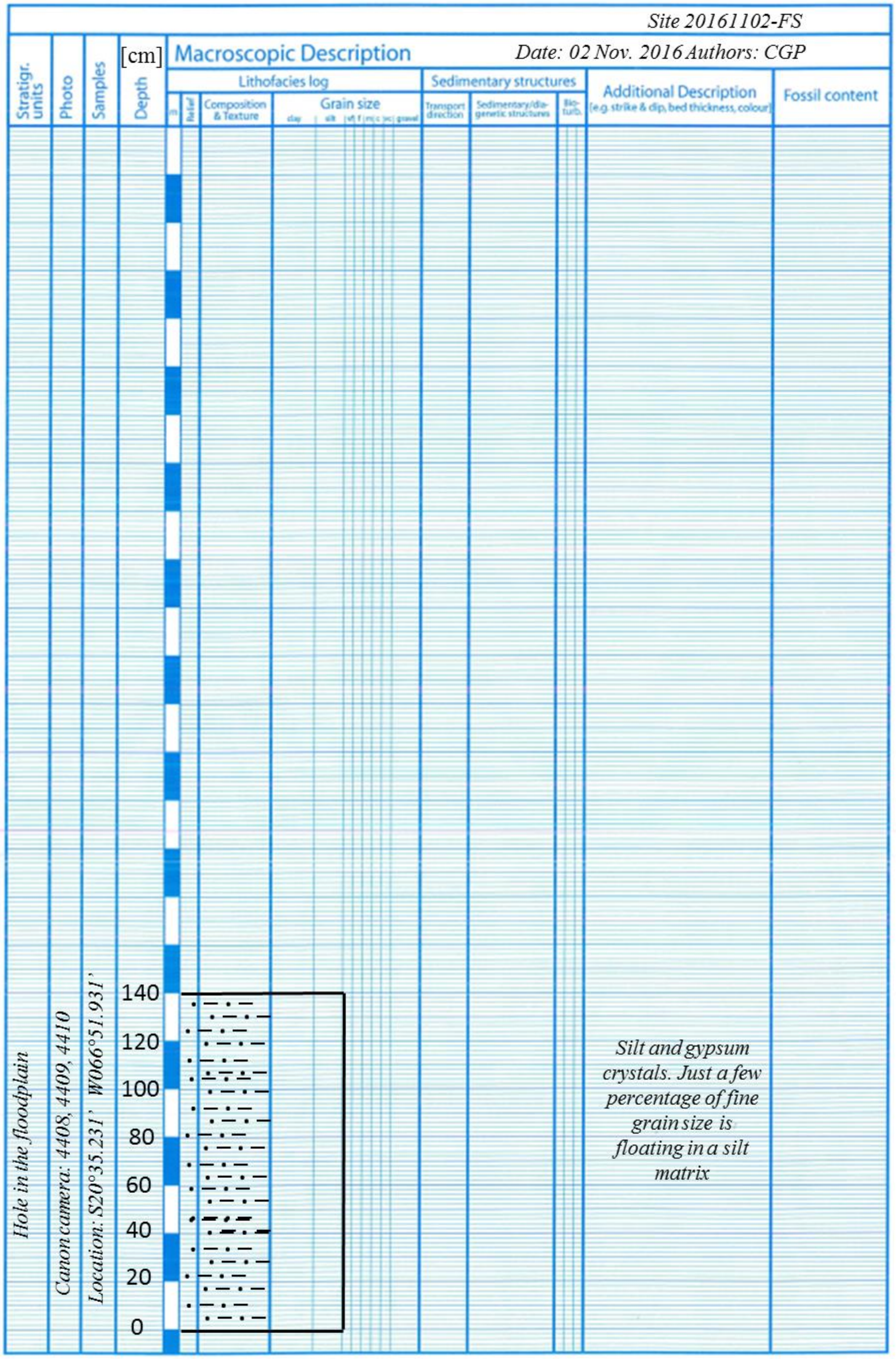

Site 20161102-FS

Date: 02 Nov. 2016 Authors: CGP

Hole in the floodplain

Canon camera: 4408, 4409, 4410

Location: S20°35.231' W066°51.931'

Silt and gypsum crystals. Just a few percentage of fine grain size is floating in a silt matrix

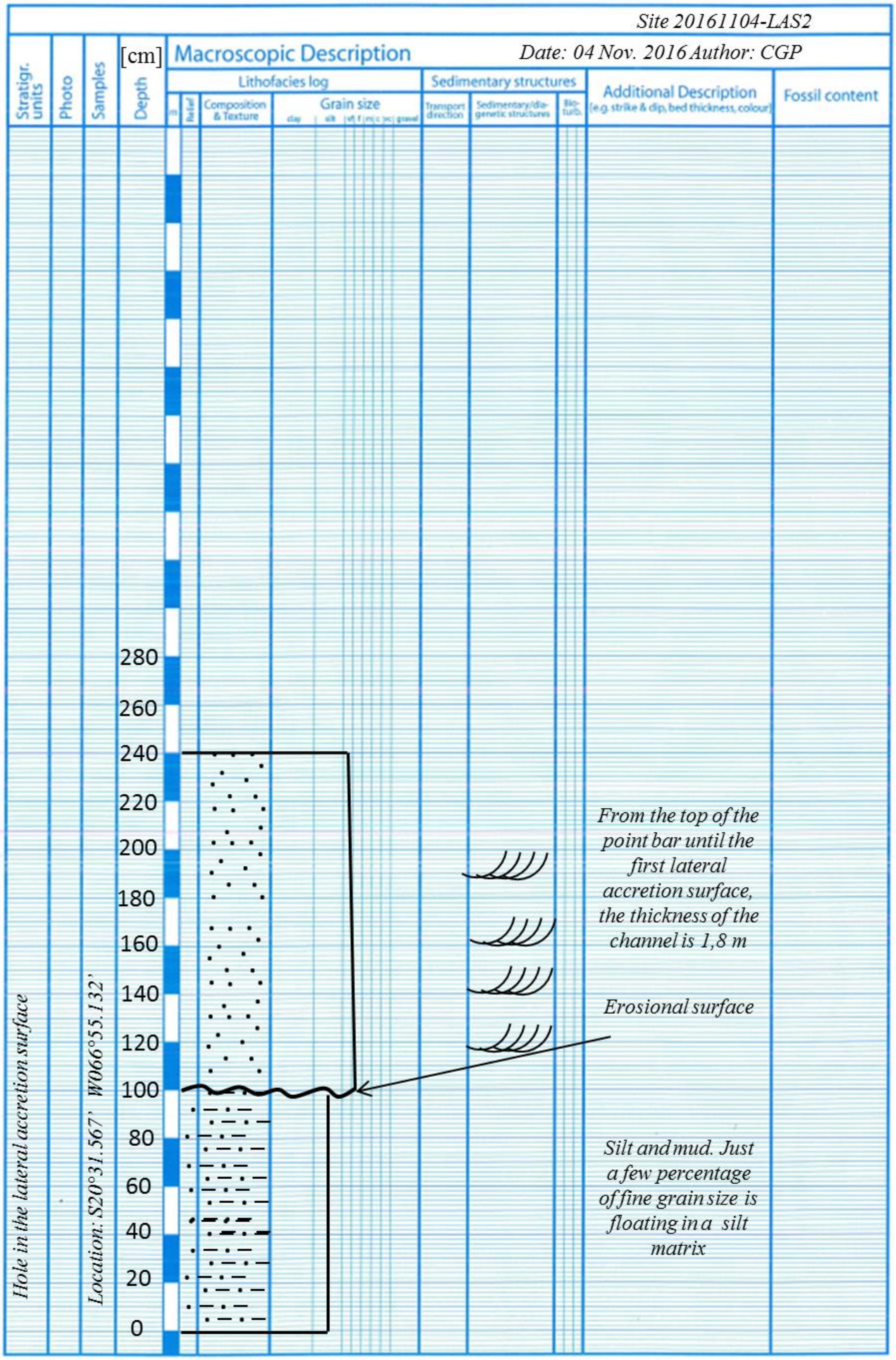

Site 20161104-LAS2

Date: 04 Nov. 2016 Author: CGP

Hole in the lateral accretion surface

Location: S20°31.567' W066°55.132'

From the top of the point bar until the first lateral accretion surface, the thickness of the channel is 1,8 m

Erosional surface

Silt and mud. Just a few percentage of fine grain size is floating in a silt matrix

Appendix E

Followed steps to construct the regional bottom layer representing the lacustrine deposits.

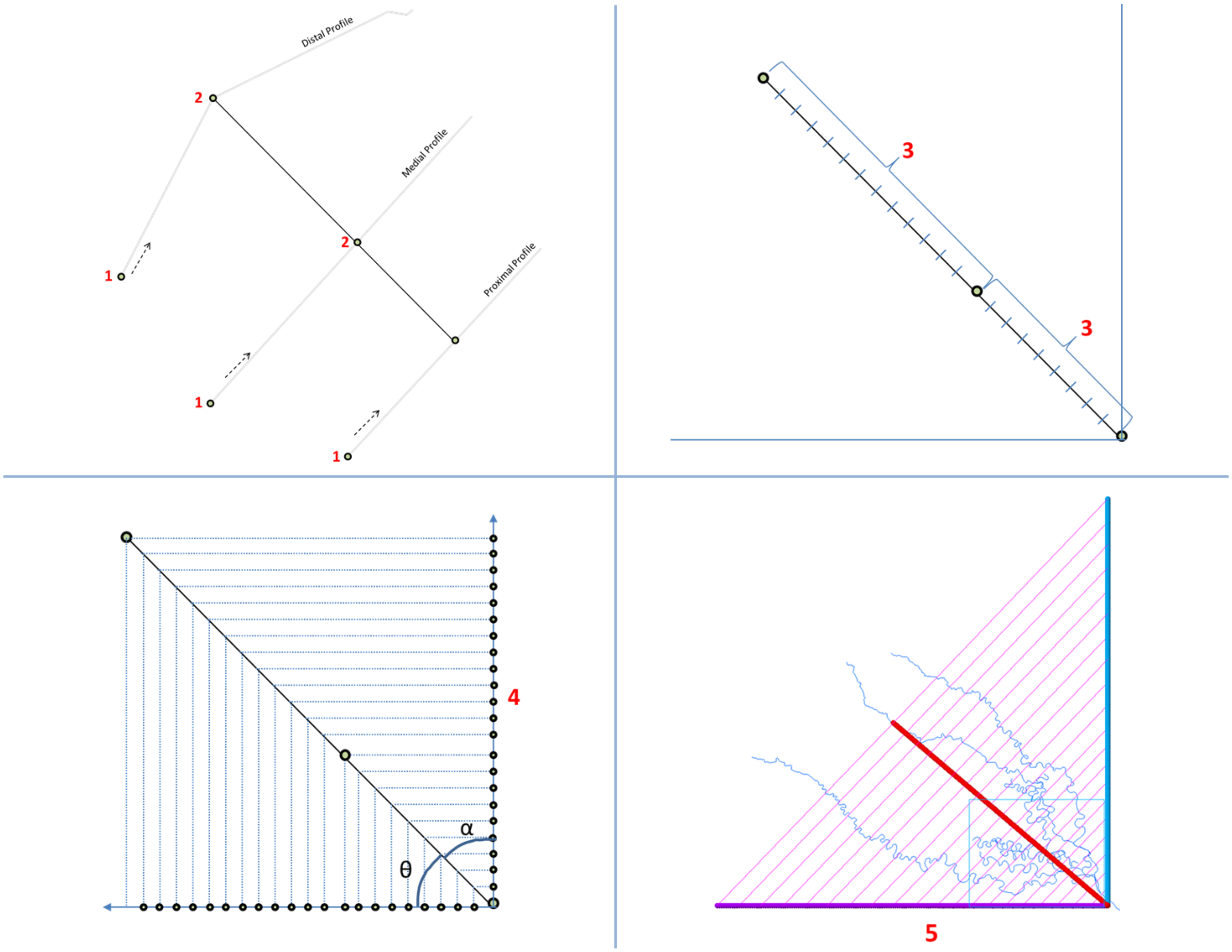

Appendix F

Core data from the Lower Rot Fringe Sandstone, Lower Rot Fringe Claystone and the Solling Claystone Members of the Pernis West – 01 from the West Netherlands Basin.

Formation	Depth [m]	Porosity [Fraction]	Horizontal Permeability [mD]	GR [API]	Distance [m]
Rot Fringe Sandstone Member	2977.09	0.19	119.00	119.20	60.00
	2977.26	0.16	56.00	117.44	120.00
	2977.57	0.18	94.00	101.65	80.00
	2978.28	0.16	36.70	108.16	140.00
	2978.61	0.19	216.00	106.55	10.00
	2978.88	0.15	73.00	104.97	110.00
	2979.13	0.13	25.00	102.03	160.00
	2979.18	0.17	93.00	101.67	90.00
	2979.42	0.17	129.00	100.33	40.00
	2979.46	0.16	79.00	98.29	100.00
	2979.63	0.16	127.00	96.11	50.00
	2980.10	0.17	105.00	95.92	70.00
	2980.40	0.17	32.00	99.99	150.00
	2982.18	0.16	36.80	85.37	130.00
	2982.48	0.18	168.00	87.71	20.00
	2983.95	0.20	224.00	108.17	0.00
	2984.85	0.18	141.00	124.93	30.00

Formation	Depth [m]	Porosity [Fraction]	Horizontal Permeability [mD)	GR [API]	Distance [m]
Lower Rot Fringe Claystone Member	2993.15	0.04	0.35	152.00	317.54
	2993.47	0.05	0.02	145.00	684.90
	2993.76	0.10	0.05	135.00	579.94
	2994.02	0.13	1.95	132.14	238.82
	2994.30	0.13	6.70	133.80	199.46
	2994.60	0.12	4.60	127.95	225.70
	2994.87	0.16	29.00	110.90	173.22
	2994.97	0.03	0.03	106.20	619.30
	2995.33	0.08	0.49	101.02	304.42
	2995.63	0.11	1.10	100.00	265.06
	2995.91	0.15	49.00	110.25	160.10
	2996.16	0.07	0.20	112.81	383.14
	2996.44	0.04	0.03	122.72	632.42
	2996.73	0.06	0.10	124.62	553.70
	2997.05	0.07	0.03	126.25	645.54
	2997.28	0.09	0.14	127.30	474.98
	2997.52	0.10	0.65	121.25	291.30
	2997.89	0.15	22.00	114.34	186.34
	2998.07	0.03	0.01	109.80	724.26
	2998.37	0.07	0.33	119.09	330.66
	2998.62	0.06	0.25	139.30	370.02
	2998.88	0.04	0.01	148.99	737.38

Formation	**Depth [m]**	**Porosity [Fraction]**	**Horizontal Permeability [mD)**	**GR [API]**	**Distance [m]**
Solling Claystone Member	2999.16	0.06	0.16	151.82	396.26
	2999.45	0.08	0.03	158.26	658.66
	2999.71	0.04	0.01	152.67	750.50
	2999.99	0.08	0.16	140.05	409.38
	3000.30	0.07	0.16	156.47	422.50
	3000.58	0.05	0.12	166.74	501.22
	3000.88	0.05	0.11	152.68	540.58
	3001.23	0.06	0.02	138.08	698.02
	3001.48	0.06	0.16	130.35	435.62
	3001.78	0.05	0.08	138.32	566.82
	3002.08	0.06	0.99	138.87	278.18
	3002.38	0.05	0.28	144.82	343.78
	3002.69	0.06	0.04	143.91	606.18
	3002.98	0.05	0.02	139.30	711.14
	3003.25	0.04	0.16	143.95	448.74
	3003.56	0.04	0.16	145.07	461.86
	3003.86	0.05	0.13	144.67	488.10
	3004.19	0.05	0.03	144.74	671.78
	3004.46	0.06	5.30	137.60	212.58
	3005.08	0.04	0.05	148.74	593.06
	3005.38	0.05	0.26	155.23	356.90
	3005.95	0.05	0.12	160.95	514.34
	3006.61	0.04	0.12	154.01	527.46
	3006.88	0.06	1.40	126.89	251.94

Appendix G

Selected wells for each facies and the different gas production rates per day, highlighting the most efficient flow rate for each case.

Well	Prod. Rate [sm3/day]	Outflow through well [sm3]	Recovery Factor
Uyuni-05	700,000	208,782,190	0.16
	500,000	225,747,882	0.18
	300,000	249,480,641	0.20
	100,000	166,758,953	0.13
	50,000	113,371,173	0.09
Uyuni-03	700,000	161,407,937	0.13
	500,000	175,357,048	0.14
	300,000	130,145,485	0.10
	100,000	127,211,860	0.10
	50,000	110,705,082	0.09
Uyuni-15	700,000	11,301,400	0.01
	500,000	11,301,400	0.01
	100,000	11,301,400	0.01
	30,000	11,301,462	0.01
	10,000	13,844,947	0.01
	6,500	8,281,415	0.01
	6,000	13,779,291	0.01
Uyuni-12	700,000	3,167,742	0.003
	10,000	3,172,047	0.003
	2,000	4,283,490	0.003
Uyuni-23	10,000	5,542,928	0.004
	4,000	4,391,565	0.004
Uyuni-24	100,000	58,010,753	0.046
	35,000	81,807,923	0.065
	28,000	48,021,719	0.038
	25,000	51,122,010	0.040
Uyuni-11	700,000	365,762	0.0003
	185	432,105	0.0003
Uyuni-22	2,000	12,472	0.0000
	10	12,897	0.0000

Appendix H

Appendix H1. Uyuni-05 water saturation evolution

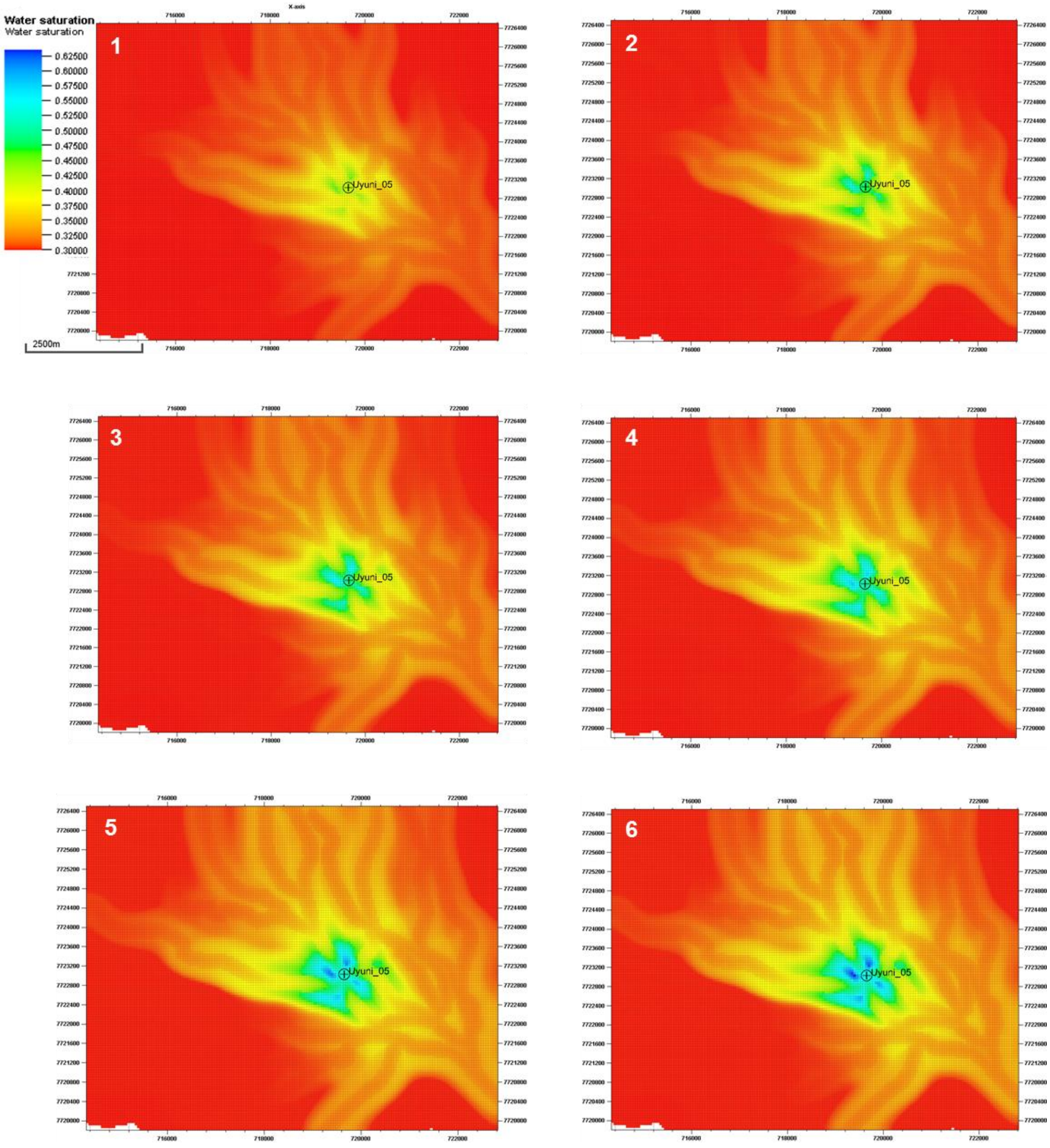

Appendix H2. Uyuni-03 water saturation evolution

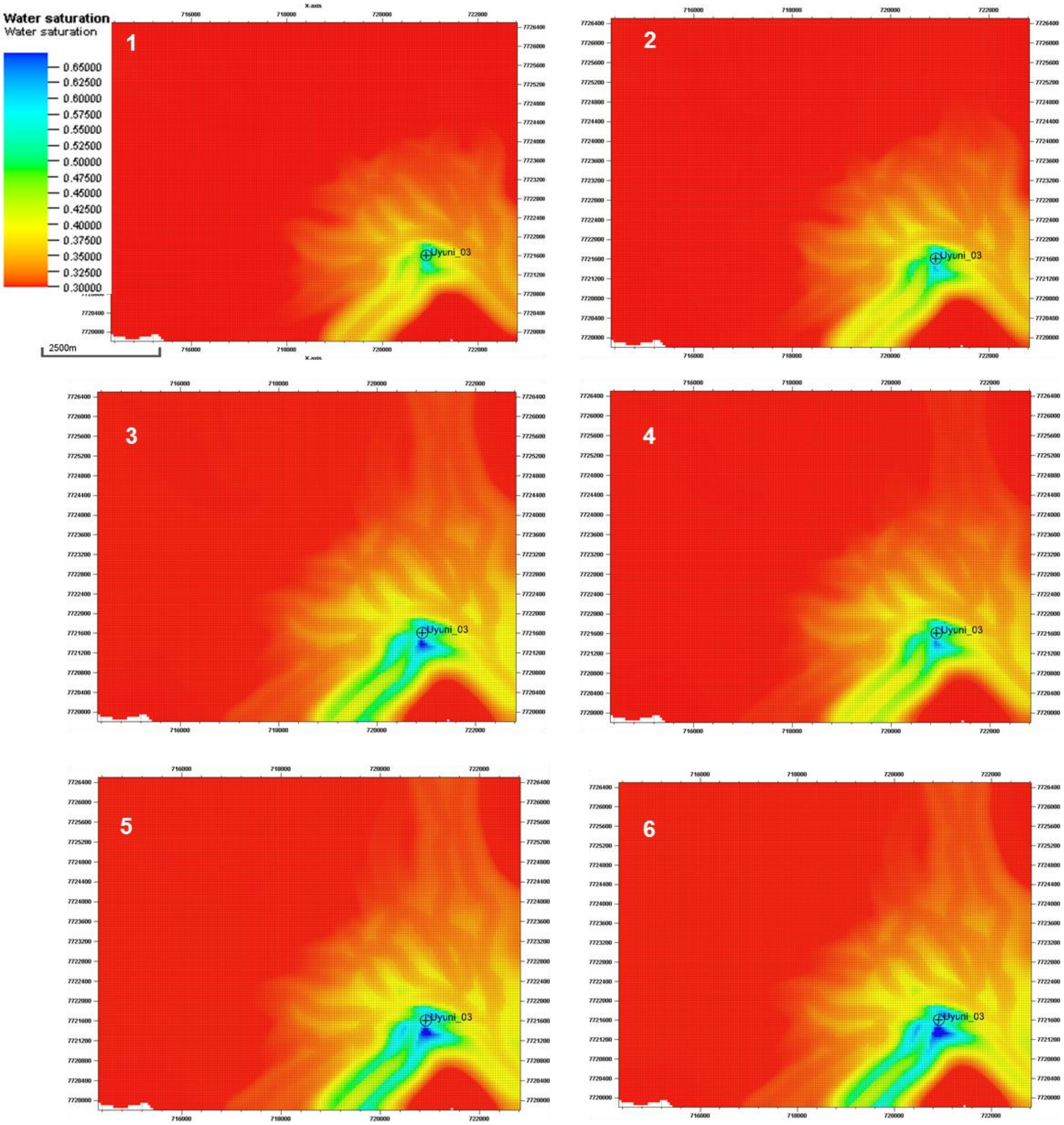

Appendix H3. Uyuni-24 water saturation evolution

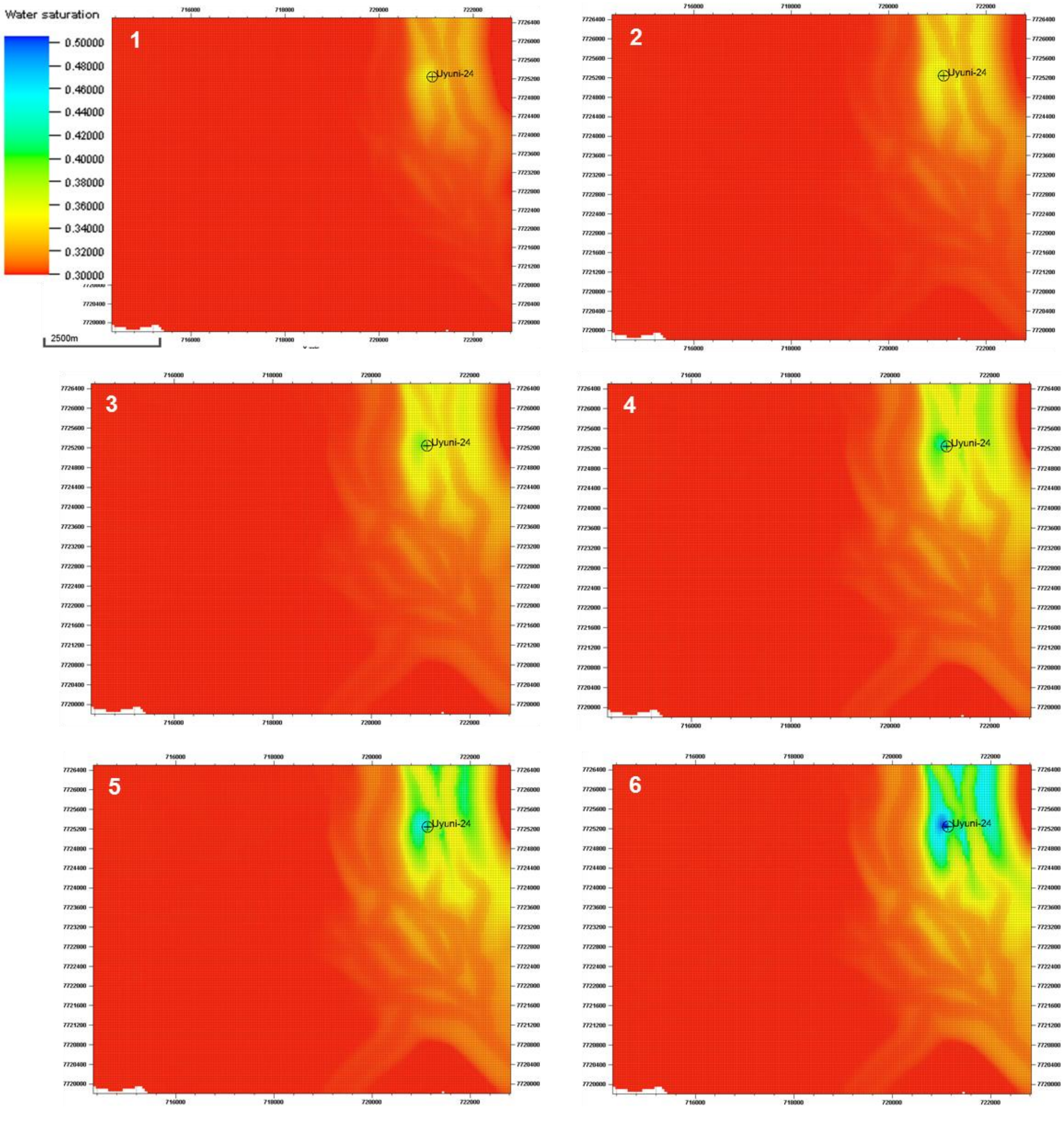

Appendix H4. Uyuni-15 water saturation evolution

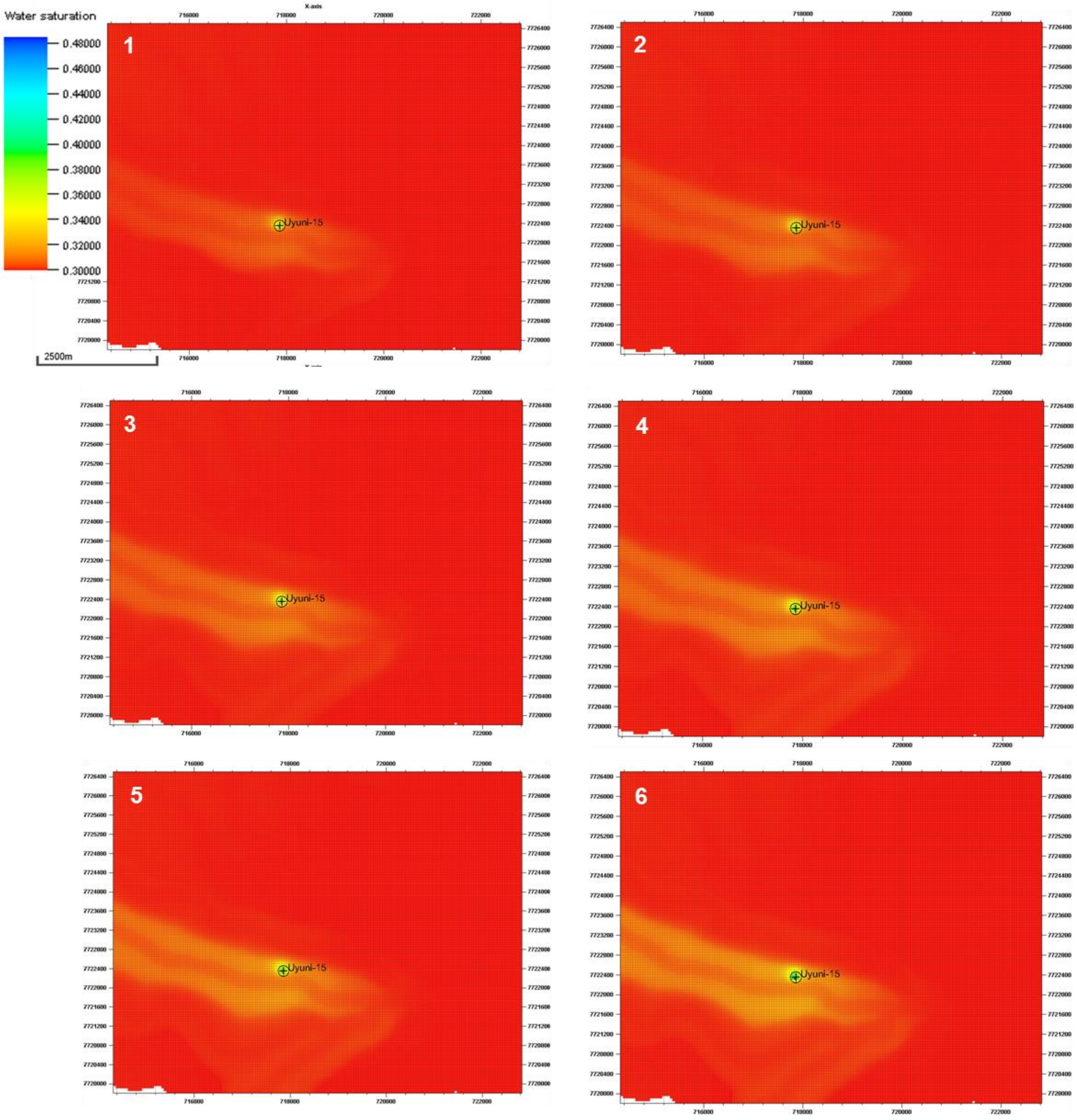

Appendix H5. Uyuni-11 water saturation evolution

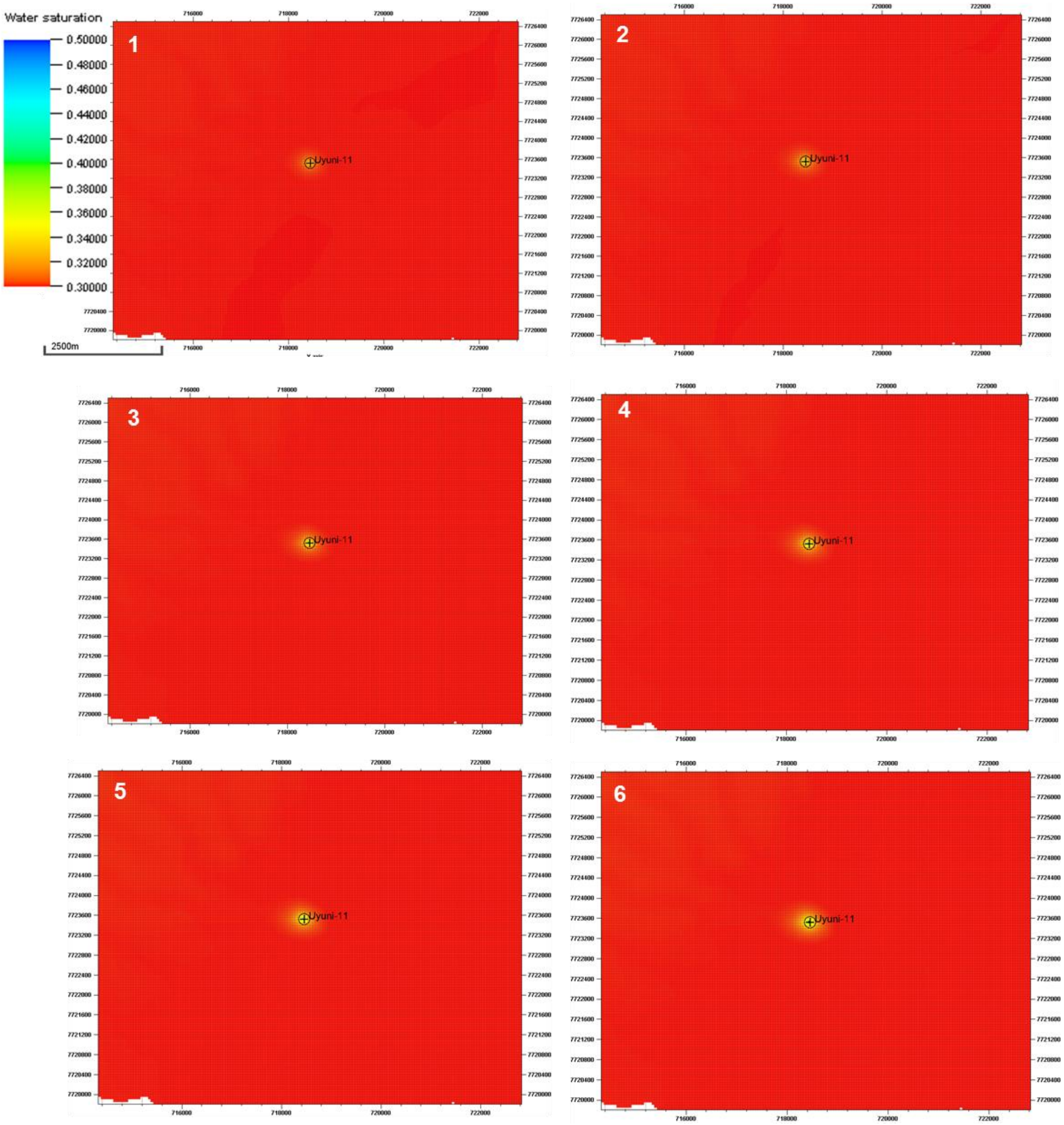

Appendix H6. Uyuni-22 water saturation evolution

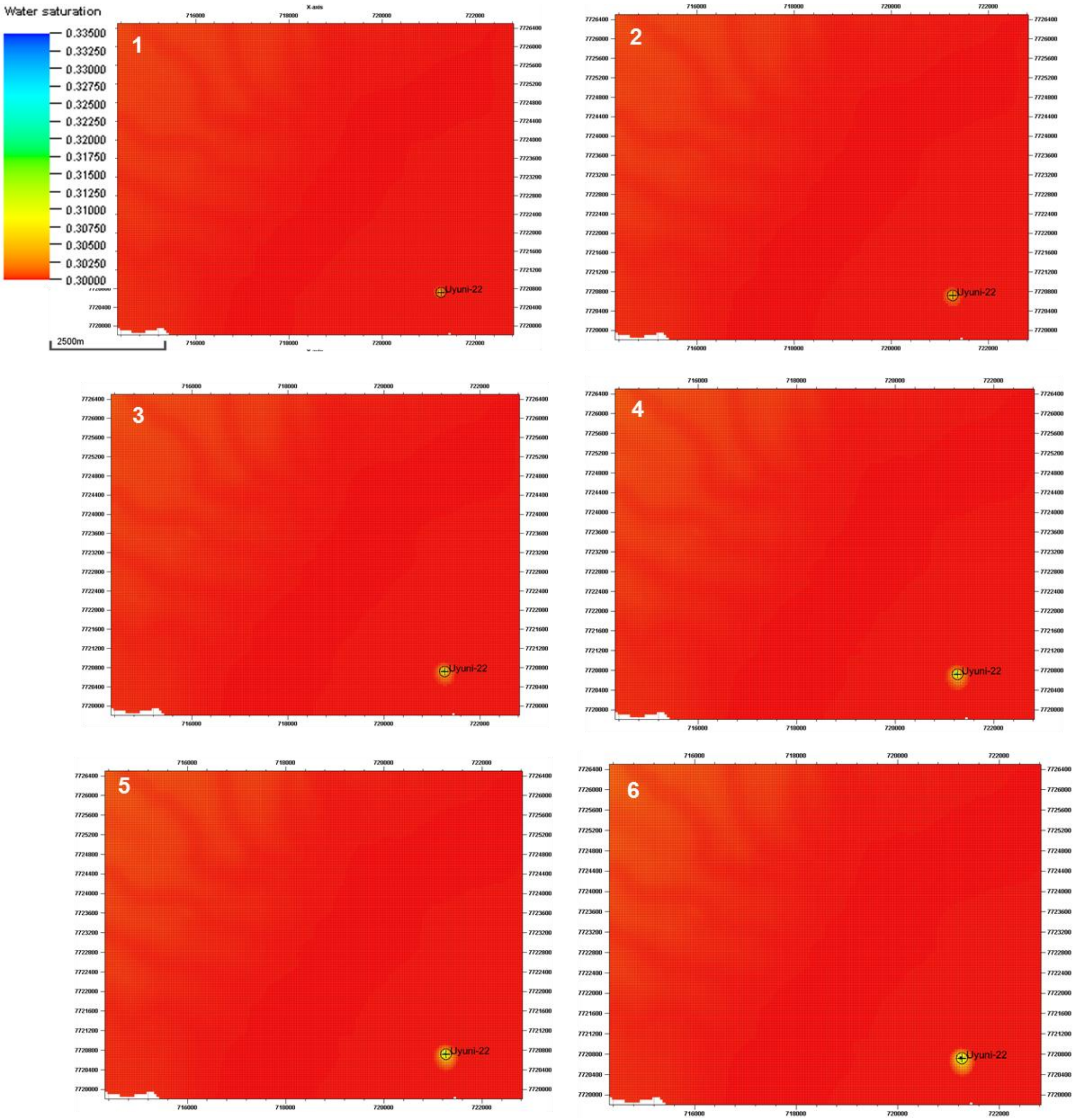

Appendix I

Evolution of the pressure depletion for different wells, starting with the first 6 months and ending up in the sixth year of production.

Appendix I1. Uyuni-05 well pressure maps

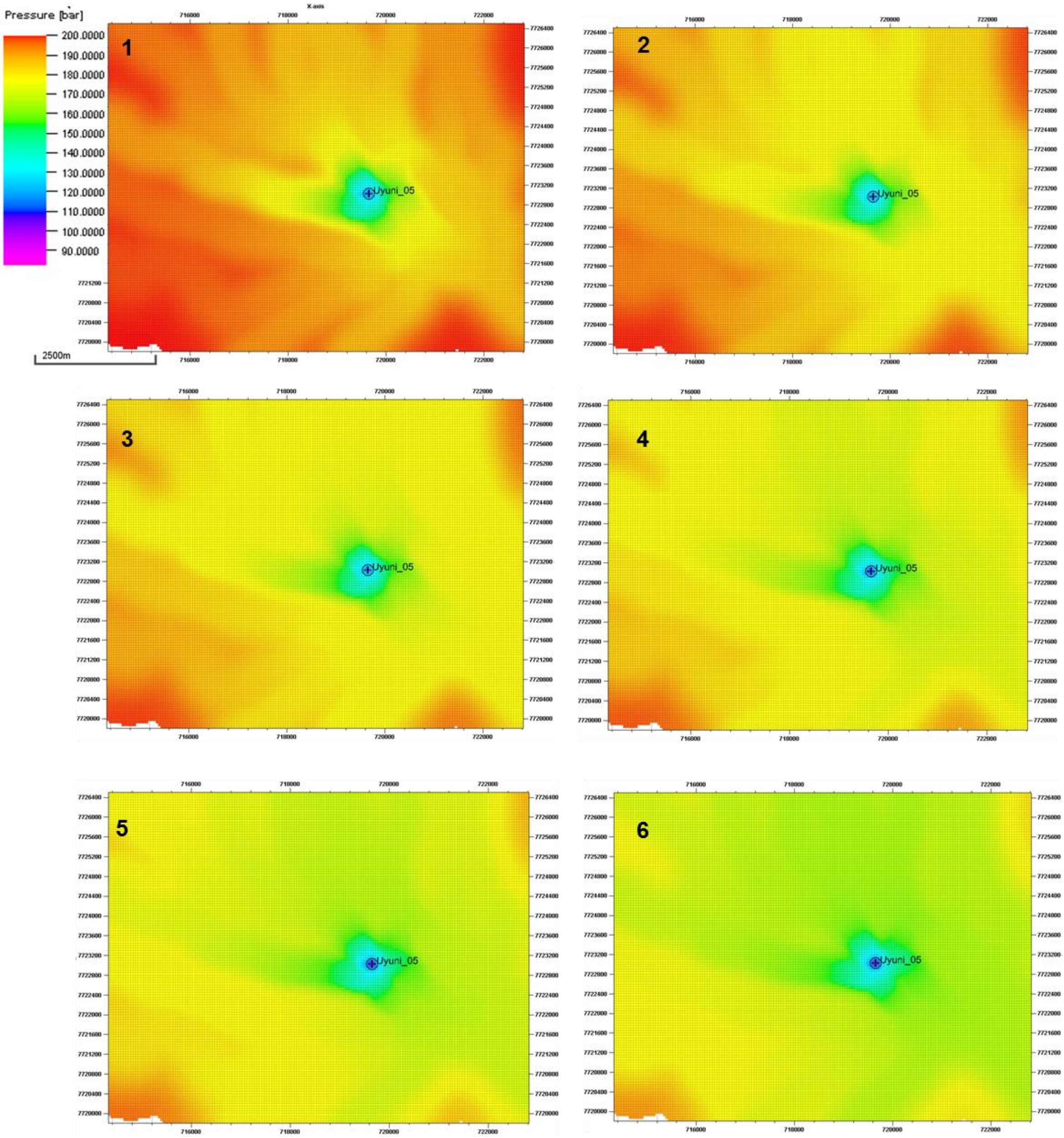

Appendix I2. Uyuni 03 well pressure maps

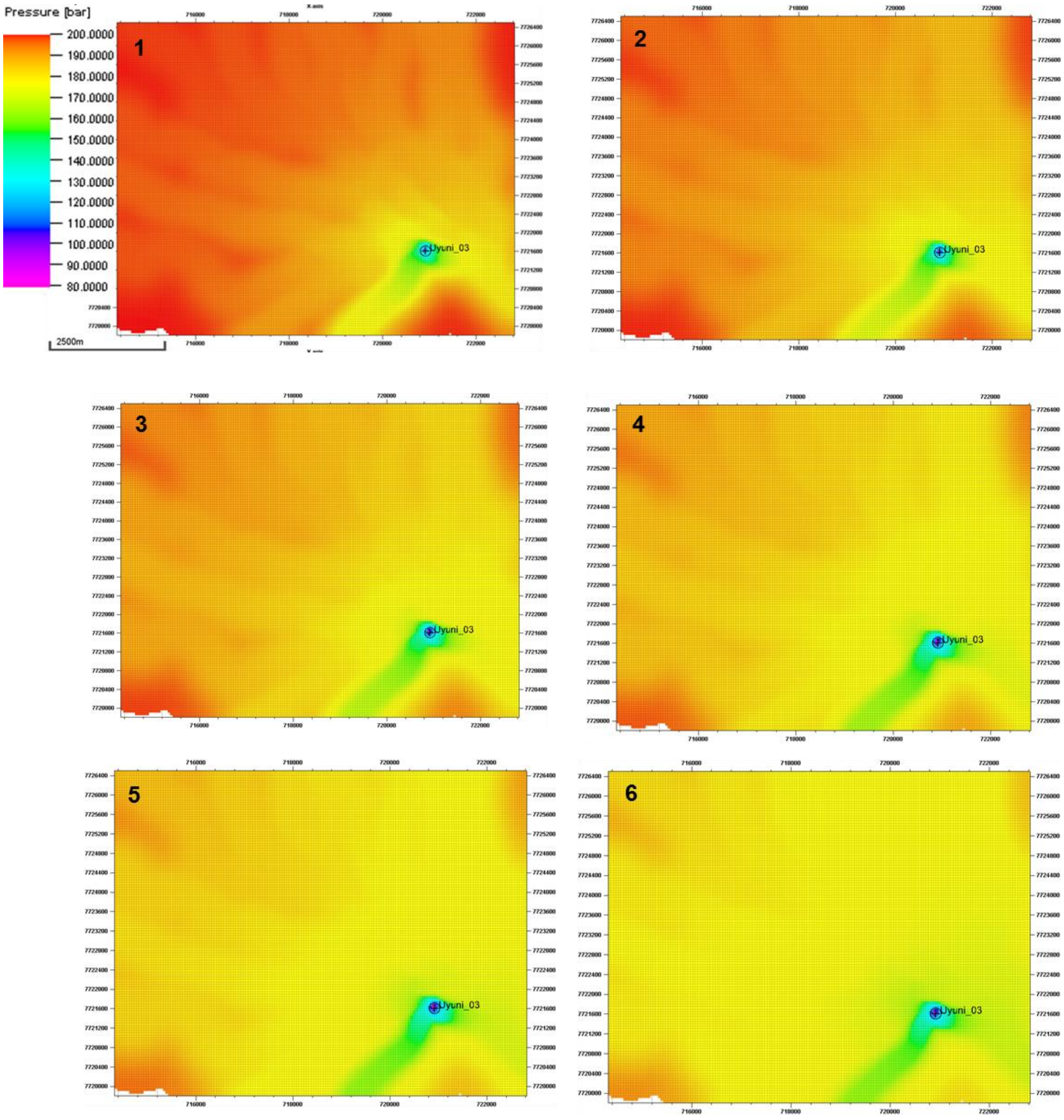

Appendix I3. Uyuni-24 well pressure maps

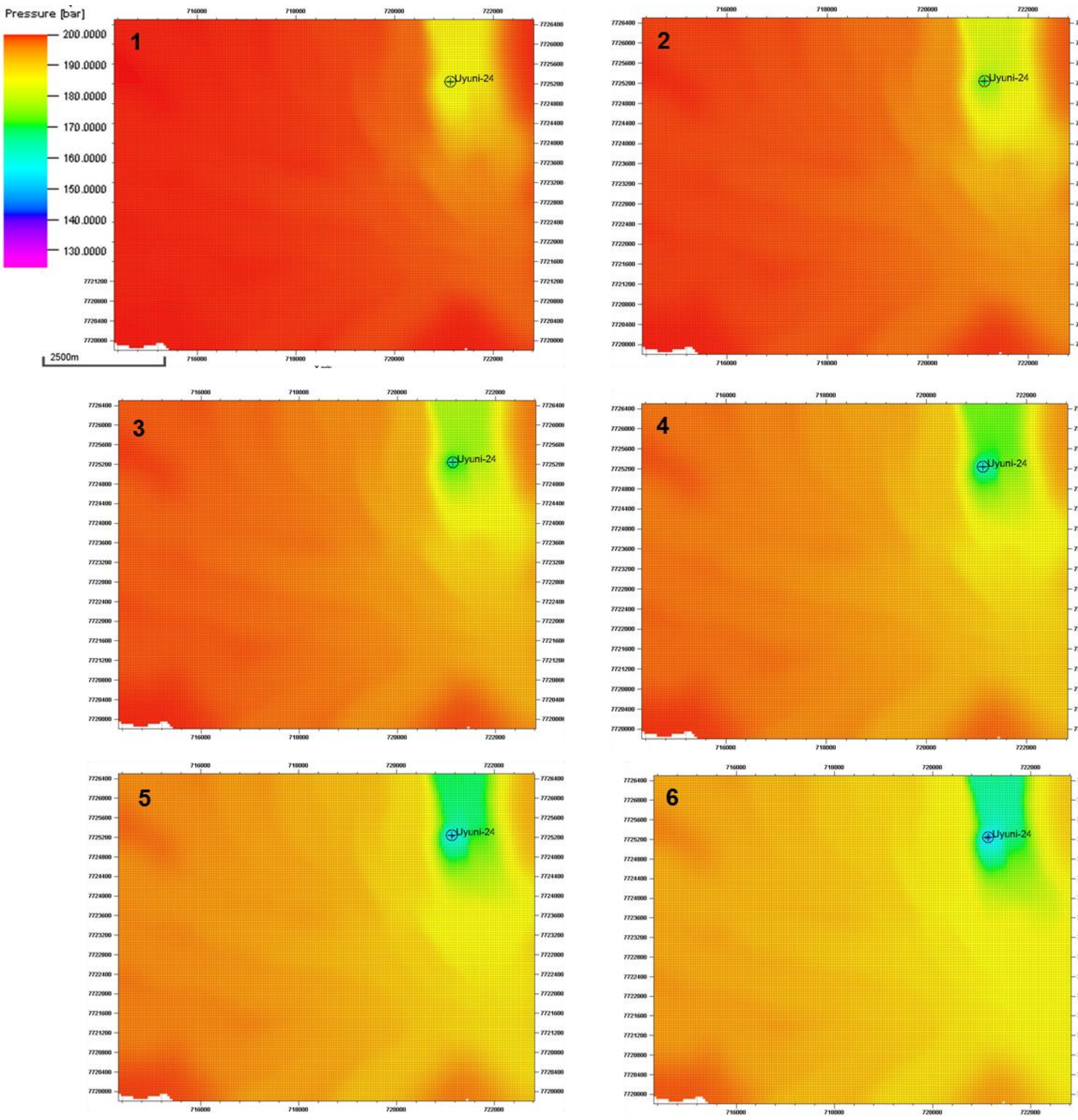

Appendix I4. Uyuni-15 well pressure maps

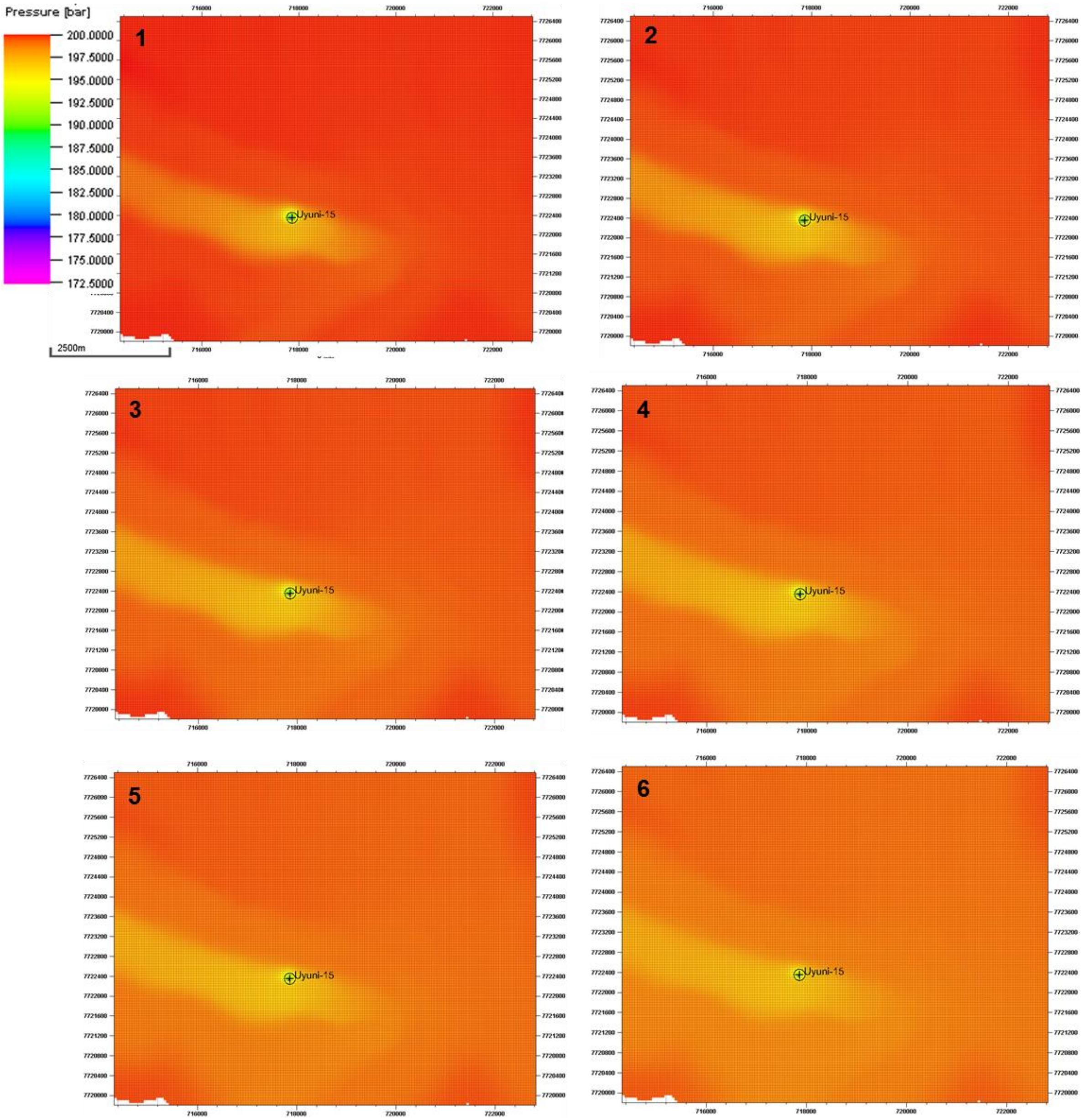

Appendix I5. Uyuni-11 well pressure maps

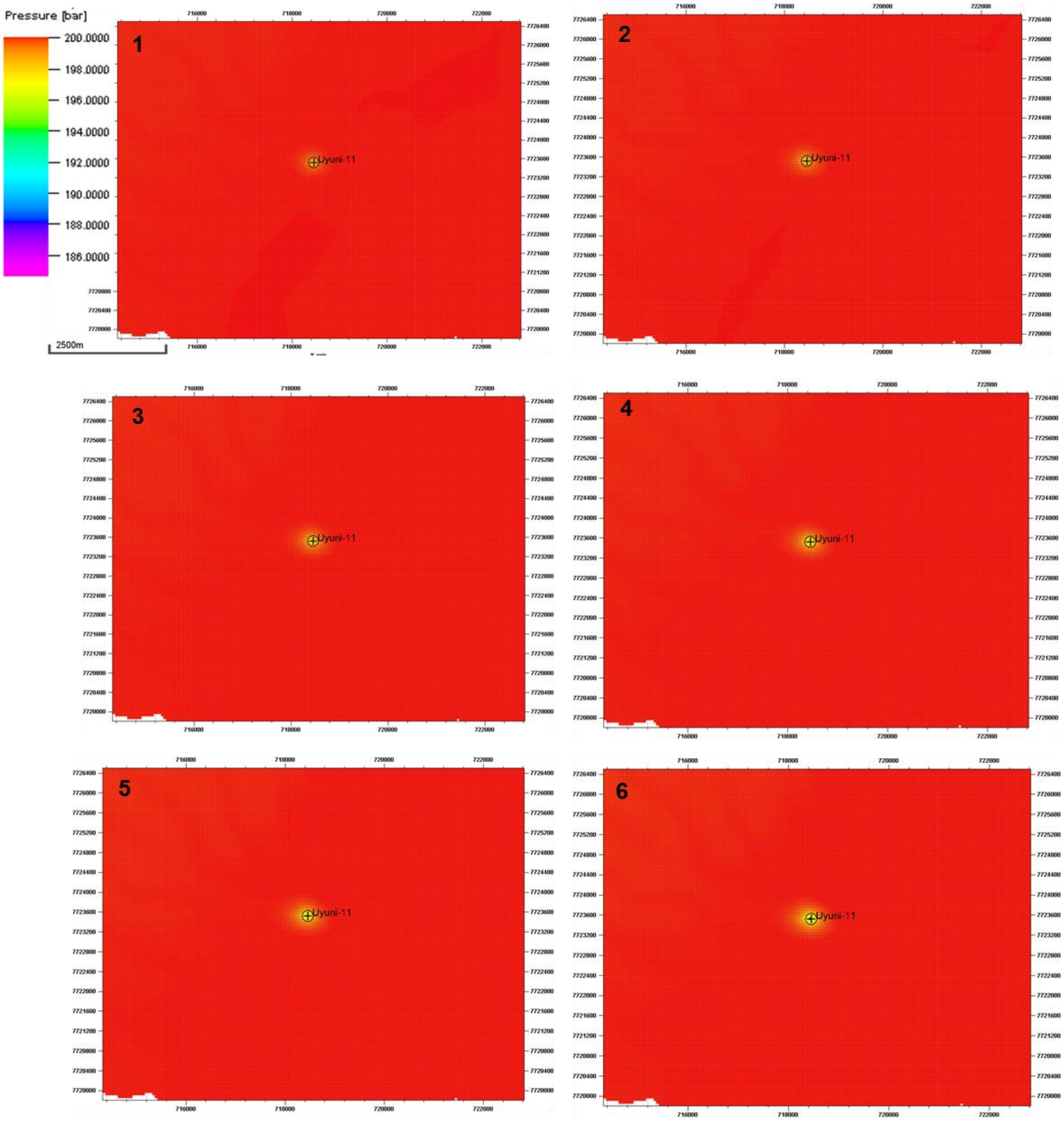

Appendix I6. Uyuni-22 pressure maps

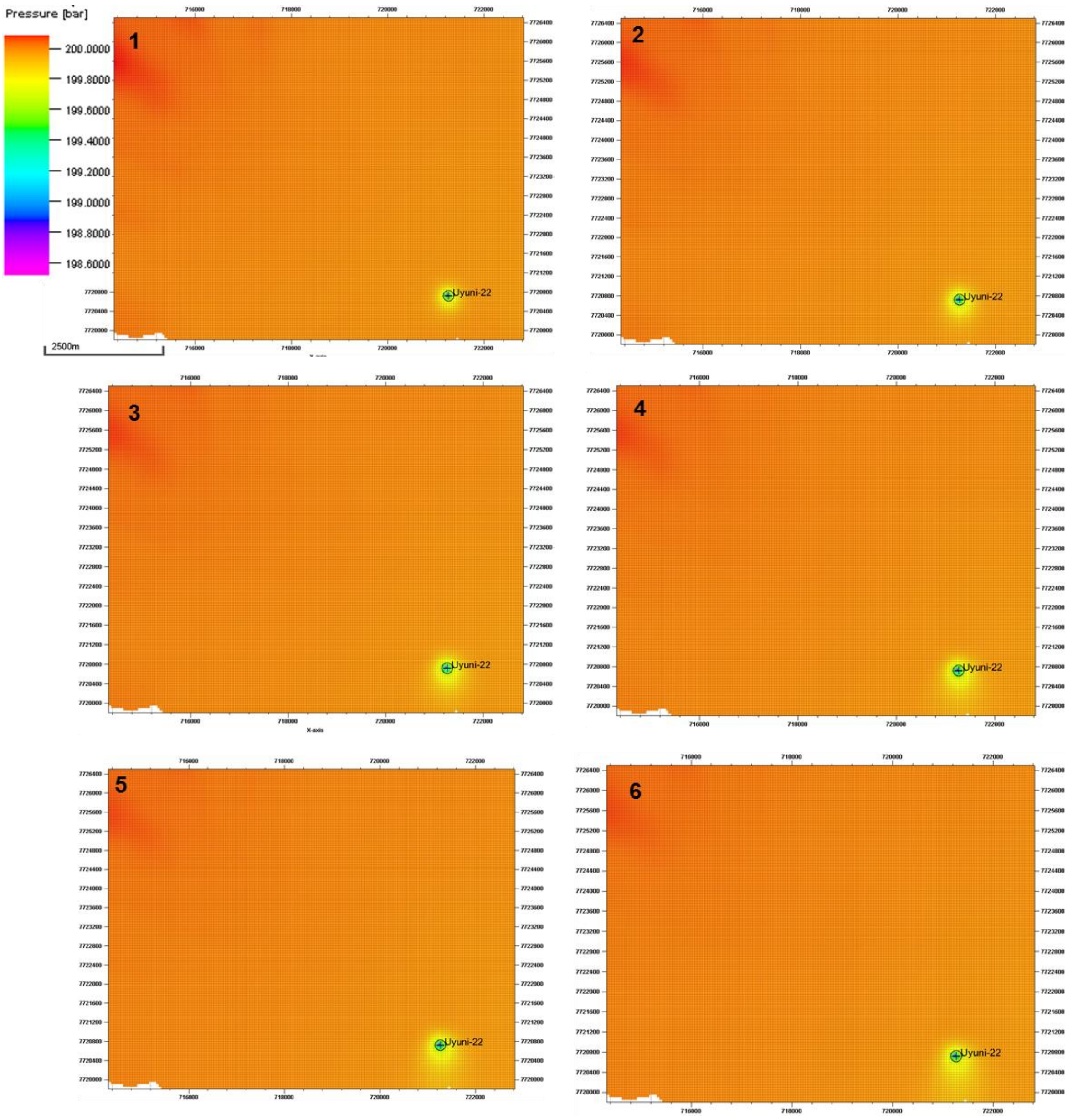

Appendix J

Sketch of one of the reasons of higher fluid contribution from channels with OSL samples 5d and 6a

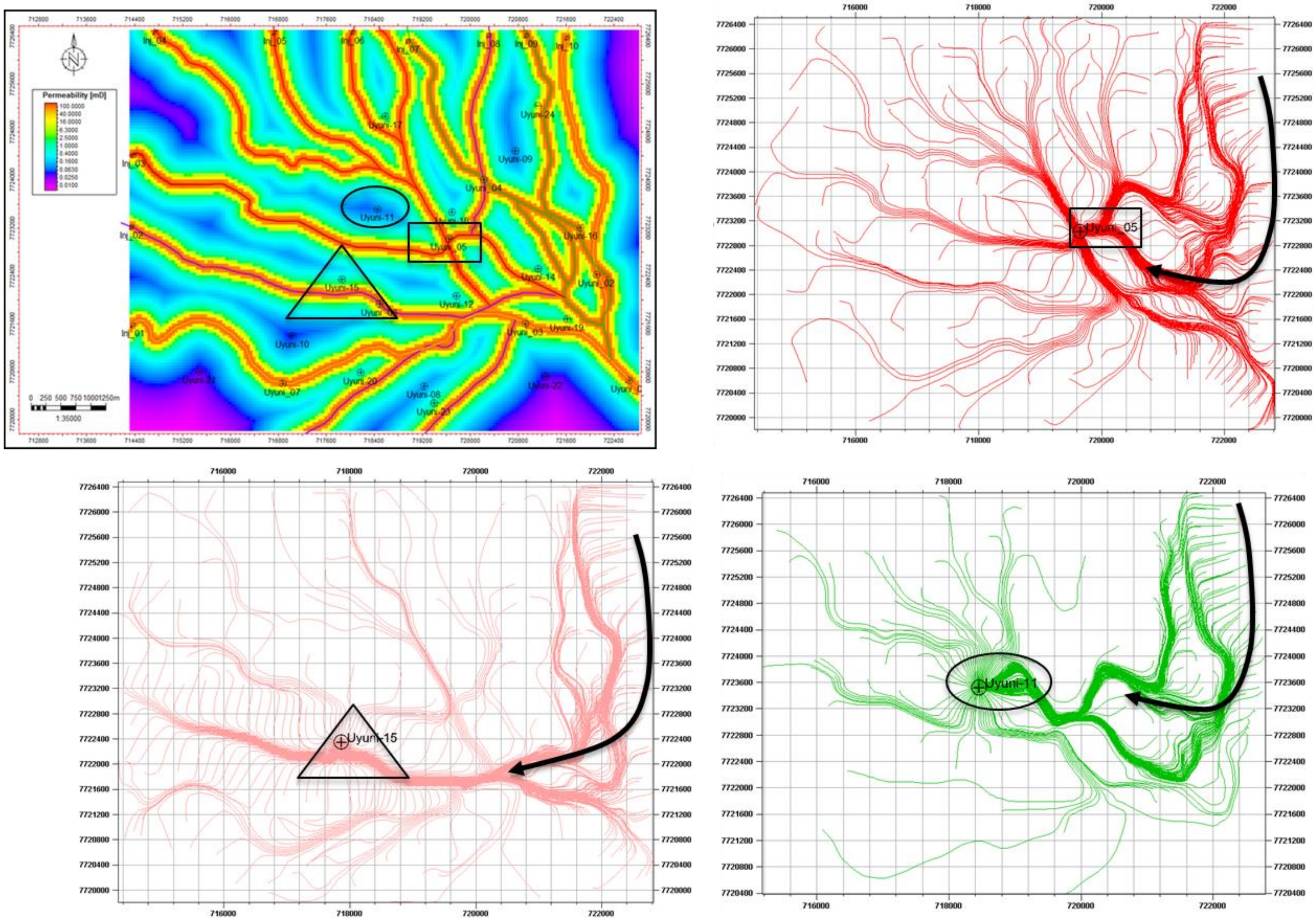

Appendix K

Histogram of the permeability generated during the property distribution in the model